The Dissertation Committee for Sangyup Lee
certifies that this is the approved version of the following dissertation:

Nonholonomic Hamiltonian Method for Multiscale Simulation of Reacting Shock Physics

Committee:

Eric P. Fahrenthold, Supervisor

Michael D. Bryant

John T. Foster

Raul G. Longoria

Eric M. Taleff

Nonholonomic Hamiltonian Method for Multiscale Simulation of Reacting Shock Physics

by

Sangyup Lee

DISSERTATION

Presented to the Faculty of the Graduate School of

The University of Texas at Austin

in Partial Fulfillment

of the Requirements

for the Degree of

DOCTOR OF PHILOSOPHY

THE UNIVERSITY OF TEXAS AT AUSTIN

August 2017

To my parents and my wife.

Acknowledgments

I wish to first thank my supervisor, Dr. Eric P. Fahrenthold for his great advice and patient answers to my innumerable questions. I learned much from him, including life lessons. I would also like to thank my committee members, Dr. Michael D. Bryant, Dr. John T. Foster, Dr. Raul G. Longoria, and Dr. Eric M. Taleff.

This research was supported by the Defense Threat Reduction Agency (Grant number HDTRA1-13-1-0023). The support and assistance of the program managers, Su Peiris and Allen Dalton, has been much appreciated.

Nonholonomic Hamiltonian Method for Multiscale Simulation of Reacting Shock Physics

Publication No. _____

Sangyup Lee, Ph.D.
The University of Texas at Austin, 2017

Supervisor: Eric P. Fahrenthold

Multiscale methods which are systematic, computationally efficient, and applicable to a wide range of materials are needed to augment experimental research in the development of improved explosives and propellants. A variety of modeling methods have been applied to detonation simulation, but different model formulation techniques are normally used at each scale. This research has developed the first unified discrete Hamiltonian approach to multiscale simulation of reacting shock physics, using a nonholonomic methodology. The method incorporates general material and geometric nonlinearities, which are of central interest in reacting shock modeling applications.

A new synchronous multiscale model has been formulated, which incorporates a macroscale Lagrangian particle-element model, a mesoscale Lagrangian finite element model, and a Lagrangian reacting molecular dynamics model. A new asynchronous multiscale model has been formulated, which incorporates a macroscale Eulerian finite element model, a mesoscale Lagrangian

particle-element model, and a Lagrangian reacting molecular dynamics model. The asynchronous model includes new strategies to accommodate the large time and space disparities between scales, and has been validated in simulations which model shock to detonation in two widely used explosives.

Table of Contents

List of Tables

List of Figures

Chapter 1

Introduction

1.1 Motivation

Computational research on reacting shock physics simulation has employed a wide range of numerical methods, including macroscale continuum hydrocodes [49], mesoscale discrete or finite element formulations [2], and molecular dynamics models [86]. Each modeling approach has been applied effectively, but quite different model formulation techniques are normally employed at each scale. For example, weighted residual solution methods for partial differential equations are often favored at the continuum scale, while discrete Hamiltonian methods are typical of molecular scale modeling. A systematic approach to the merger of dissimilar modeling methods is needed to better address the multiscale multiphysics simulation problem. Although some multiscale Hamiltonian methods have been developed [41], their utility has been greatly limited by two factors: (1) an inability to model general thermomechanical coupling at all scales, and (2) an exclusive focus on holonomic formulations.

Parallel computing, and the associated development of improved numerical methods, have allowed computational physics to make significant con-

tributions to the solution of a variety of science and engineering problems. The problems of interest include energetic materials design, terminal effects simulations, and a wide range of applications in between. Although further advances are needed in the development of models at each level, the most challenging needs in current computational research are those associated with the systematic integration of distinct numerical methods developed for application at various scales.

Numerical methods which attempt to simulate macroscale shock-to-detonation problems must incorporate process models of: (1) chemical physics which occurs at the molecular scale, and (2) ignition and growth physics which occurs at the explosive grain scale. Integrated multiscale models must span a very wide range of spacial and temporal scales, as indicated in Table 1.1. Current computational methods normally address this issue by resorting to empirical descriptions of the chemical, ignition, and growth processes of interest. This work introduces a modeling approach which reduces the need for the complex experiments used to develop fully empirical formulations. In particular, the present work avoids any reliance on empirical ignition and growth models developed using explosive experiments. The focus here is on combining fundamental balance laws (for mass, energy, and momentum) with molecular scale chemistry in order to develop the multiphysics model.

This research has developed the first unified approach to multiscale reacting shock physics simulation, extending previous research [18, 29, 31]. Unlike all previous research, this work applies a uniform (nonholonomic discrete

Hamiltonian) modeling approach at all scales. The research also introduces novel multiscale integration strategies. Unlike all previous research, the great temporal and spacial disparities between scales are addressed (in part) by coupling the meso and macro scale thermomechanical models to distinct chemistry models, each of which incorporates time constants which match those of the corresponding thermomechanical subsystems.

1.2 Previous Work

Demands for the development of multiscale simulations have increased over past decade, in a wide variety of research areas, including nano structure [34], earth science [87], propulsion [56], and munitions [71] research. Strong interest in the mesomechanical aspects of material behavior has motivated interest in mesoscale simulations, while the efforts to develop first principals predictions of material bahavior have motivated interest in molecular dynamics (MD) simulations.

As noted in the last section, a wide variety of simulation approaches focus on only a single scale. Macroscale simulations generally model shock to detonation in order to reduce reliance on experiments, for weapons design or other applications [56]. Mesoscale (grain-scale or micro-scale) simulations have primarily focused on hotspot generation, the most widely accepted ignition mechanism [22]. Various studies have attempted to develop hotspot ignition models caused by pore collapse or plastic deformation, including: voids with or without gases [40, 53, 72, 73], stochastic approaches [3], and continuum P-

α models [50, 70]. Molecular dynamics research has produced a number of successful approaches to process modeling, including: ab-initio methods [25], ReaxFF [86, 88], DFTB [46], reacting MD [62], and has made limited use of nonholonomic methods [37].

Successful implementations of single scale approaches has naturally led to interest in interscale links. Such coupling research has employed various multiscale integration strategies, including material point methods [34], multiscale shock techniques (MSST) [60], quantum based upscale MD [71], coarse-grained molecular dynamics (CGMD) [63], multiscale coarse-graining (MS-CG) [33]), interscale homogenizations [57, 59, 61], interscale transient methods [8, 42]), and uniform formulation methods [26, 41]. Most multiscale models, however, apply quite different formulation methods at different scales. Although some 'single formulation' methods have been developed, they have either not included comprehensive thermodynamic coupling [41, 42] or have not considered interscale differences disparate enough to be applied in energetic materials applications [8, 51]. Similarly, MD based multiscale strategies are severely challenged to accommodate the disparity between scales associated with practical application of reacting shock modeling [71].

With regards to multiscale integration of chemical kinetics models, a variety of approaches have been developed, including empirical kinetics models [2], ignition and growth models [38], simplified reaction models [30, 48, 58], and assimilation of chemical kinetics models which originate from MD results [44, 52]. All these models are either limited to simulations of parts of the

detonation processes or focus solely on empirical kinetics for specific materials; they do not fundamentally resolve the issue of the great spatial and temporal gaps between scales.

The aimed objectives of the new multiscale formulation presented here include the development of a unified model formulation approach (based on a nonholonomic thermomechanical Hamiltonian method) and the development of new integrating strategies which provide a sound and flexible foundation for explosive detonation simulation.

1.3 Objective

This research is developing, implementing, and validating a new multiscale formulation of reacting shock physics, using a new nonholonomic Hamiltonian modeling methodology. The formulation is discrete nonholonomic Hamiltonian, at all scales. Although Hamiltonian methods are typically associated with Lagrangian frames and the molecular scale, this research incorporates both Eulerian and Lagrangian frames, and a combination of finite element, particle, and hybrid particle-element kinematics. The approach is enabled by: (1) introducing thermal and chemical states as generalized Hamiltonian coordinates, and (2) separating the discretization process (e.g. finite element interpolation) from the solution method (e.g. weighted residual methods for partial differential equations (PDE)). Note that discretization precedes application of the Hamiltonian solution method. General geometric and material nonlinearities are included. The general theoretical approach may be extended

to address a wide range of computational materials design problems.

A synchronous multiscale approach is theoretically formulated using a seamless description of constitutive relations at the macro, meso, and molecular levels. An asynchronous multiscale approach is both theoretically formulated and validated with practical examples of reacting shock physics simulation. Simulations are included which validate the models developed at each scale, as well as the integrated models, against the published shock to detonation experiments on condensed phase explosives. These simulations include: (1) mesoscale hotspot generation models with explicit and implicit voids, (2) a macroscale shock to detonation description, (3) integration of mesoscale thermomechanical models with a short time (detonation) chemistry models, and (4) integration of macroscale thermomechanical models with long time (recombination) chemistry models.

The methods which are employed at each scale build on previous research. The multiscale approach presented here extends previously developed hybrid particle element (HPE) methods [31], finite element methods (FEM) [18, 29] and the concurrently developed reacting molecular dynamics (RMD) methods [4]. For convenience, Table 1.2 relates the aforementioned methods to the multiscale modeling work undertaken in this research.

1.4 Organization

The dissertation includes two multiscale modeling approaches and numerical validation of the second approach. In Chapter 2, a synchronous multi-

scale approach is developed, in a theoretical context. The formulation includes macroscale, mesoscale, and molecular scale models. All three scales are coupled by nonholonomic constraints, demonstrating seamless integration and a unified formulation approach. Chapters 3-7 develop a new asynchronous multiscale modeling approach. In Chapter 3, the multiscale approach is outlined, including meso-macro scale formulations and example applications. Chapter 4 describes key components of the asynchronous approach, including linking of the thermomechanical and chemical kinetics models and the development of equation of state formulations. In Chapter 5, the hybrid particle-element and Eulerian finite element formulations to be used at the meso and macro scales are validated against published experimental data, at individual scales. The simulations presented in Chapter 5 include hotspot generation at the grain scale and a shock to detonation modeling at the macroscale, the latter for TNT and Composition-B. Chapter 6 integrates the individual scale models, and validates the method using detonation simulations for HMX. Chapter 6 includes detailed development of the state equations for the multiphysics system. All the simulations focus on validating against published experimental data. Chapter 7 validates the method for a second explosive (RDX). Finally Chapter 8 summarizes the significant contributions of this research.

Table 1.1: Comparison of the three scales.

Scale	Spatial unit	Temporal unit	Application
Macro	mm	μs	shock to detonation
Meso	μm	ns	hotspot generation (granular scale)
Molecular	nm	ps	chemical reaction (atomic scale)

Table 1.2: Overview of the specific models.

Scale	Method	Synchronous	Asynchronous
Macro	Frame Discretization Formulation	Lagrangian Hybrid Particle Element Hamiltonian Method	Eulerian Finite Element Hamiltonian Method
Meso	Frame Discretization Formulation	Lagrangian Finite Element Hamiltonian Method	Lagrangian Hybrid Particle Element Hamiltonian Method
Molecular	Frame Discretization Formulation	Lagrangian Particle Hamiltonian Method	Lagrangian Particle Hamiltonian Method
Multi	Integration	Nonholonomic Constraints	Interscale coupling with Ignition process & Chemistry models

Chapter 2

Synchronous Multiscale Approach

2.1 Introduction

This chapter[1] presents a unified approach to the synchronous multiscale reacting shock physics modeling problem, in which the governing equations for all scales are advanced at the same time step. Although synchronous multiscale modeling limits the time scale addressable in any practical simulation, such formulations are nonetheless of significant theoretical interest. In succeeding chapters synchronous multiscale nonholonomic Hamiltonian formulations of reacting shock physics will be developed and applied in the simulation of the general multiscale reacting shock physics problems.

2.2 Kinematics and Structure of the Multiscale Model

The numerical formulation presented in this section is Lagrangian, at all scales. The assumed kinematics vary with the scale: particles are used at the

[1]This chapter is based on the previous publication: Fahrenthold, E.P., Lee, S., and Bass, J.L., "Multiscale simulation of reacting shock physics," presented at AIAA SciTech, San Diego, California, 4-8 January, *AIAA 2016-1508*, 2016. The co-authors Fahrenthold and Bass are experts in applied mechanics and reacting molecular dynamics respectively, the dissertation author's expertise is in the integration of applied mechanics and reacting molecular dynamics methods to form multiscale models.

molecular scale, finite elements are used at the mesoscale, and hybrid particle-element kinematics are used at the macroscale. Discrete thermomechanical Hamiltonian methods (with internal or potential energy variables serving as generalized coordinates) are used at all scales. For each macroscale element, a mesoscale unit cell composed of an array of Lagrangian finite elements models elastic-plastic deformation at the grain scale, including explosives and binder (voids may be modeled implicitly, using internal states). For each macroscale particle, a molecular dynamics ensemble models chemical reactions and the release of explosive energy, with morphing potentials reflecting the evolution of the electronic structure. The three scales are linked by nonholonomic constraints: macroscale deformation determines both the motion of the mesoscale unit cell boundaries and transient changes in the volume of the molecular ensemble. Figure 2.1 shows the structure of the synchronous multiscale model.

The hybrid particle-element kinematics used at the macroscale level allow for Lagrangian frame simulation of shock induced fracture, fragmentation, and melting processes of the type most often modeled using Eulerian hydrocodes. In the reacting shock physics application of interest here, where detonation will fail the macroscale elements, the hybrid kinematics allow for a seamless and thermodynamically consistent transition to a pure particle model of the explosive products. In previous work the hybrid kinematics adopted here have been validated in a wide range of macroscale simulations, including ordnance velocity impacts [31], hypervelocity impacts [65], and fabric perforation [64].

In the sections which follow, both the macroscale and mesoscale finite element kinematics are large strain Lagrangian, and the elements are homogeneously deformed. For clarity, a single prime ($'$) is used to denote mesoscale variables while a double prime ($''$) is used to denote molecular scale variables. All variables are defined as they are introduced.

2.3 Macroscale Model

The macroscale Hamiltonian (H) is

$$H = T + V \tag{2.1}$$

where the kinetic (T) and potential (V) energy are (for n ellipsoidal particles)

$$T = \frac{1}{2}\sum_{i=1}^{n}\left(\frac{\mathbf{p}^{(i)2}}{m^{(i)}} + \mathbf{h}^{(i)T}\mathbf{J}^{(i)-1}\mathbf{h}^{(i)}\right), \qquad V = \sum_{i=1}^{n} U^{(i)} \tag{2.2}$$

and the particle internal energies ($U^{(i)}$) are state variables. The generalized momenta are

$$\mathbf{p}^{(i)} = m^{(i)}\dot{\mathbf{c}}^{(i)}, \qquad \mathbf{h}^{(i)} = \mathbf{J}^{(i)}\boldsymbol{\omega}^{(i)} \tag{2.3}$$

where $\mathbf{c}^{(i)}$ is a center of mass position vector, $\boldsymbol{\omega}^{(i)}$ is a particle angular velocity vector described in a body fixed, co-rotating frame, $m^{(i)}$ is a particle mass, and $\mathbf{J}^{(i)}$ is a particle inertia tensor.

The particle densities ($\rho^{(i)}$) are computed from the rate equations ($\zeta^{(i,j)}$ is an ellipsoidal coordinate)

$$\frac{\dot{\rho}^{(i)}}{\rho_o{}^{(i)}} = -\frac{3}{N^{(i)}}\sum_{j=1}^{n}\left(\frac{\zeta^{R(i,j)}}{\zeta^{(i,j)}}\right)^3 \frac{\dot{\zeta}^{(i,j)}}{\zeta^{(i,j)}}\, W^{(i,j)} \tag{2.4}$$

where $N^{(i)}$ is a neighbor count, $W^{(i,j)}$ is an interpolation kernel, $\zeta^{R(i,j)}$ determines the particle interaction range, and

$$\dot{\zeta}^{(i,j)} = \frac{1}{\zeta^{(i,j)}} \left[\left(\hat{\mathbf{H}}^{(j)} \mathbf{r}^{(i,j)} \right)^T \dot{\mathbf{r}}^{(i,j)} + 2 \left(\mathbf{H}^{(j)} \hat{\mathbf{r}}^{(i,j)} \times \hat{\mathbf{r}}^{(i,j)} \right)^T \mathbf{G}^{(j)} \dot{\mathbf{e}}^{(j)} \right] \tag{2.5}$$

$$\mathbf{r}^{(i,j)} = \mathbf{c}^{(i)} - \mathbf{c}^{(j)}, \qquad \hat{\mathbf{r}}^{(i,j)} = \mathbf{R}^{(j)T} \mathbf{r}^{(i,j)} \tag{2.6}$$

The coefficient matrices $\mathbf{R}^{(j)}$, $\mathbf{G}^{(j)}$, $\mathbf{H}^{(j)}$, and $\hat{\mathbf{H}}^{(j)}$ are functions of the macroscale particle center of mass coordinates and the Euler parameters ($\mathbf{e}^{(j)}$, which allow for arbitrary rotations).

The evolution equations for the internal energy are (additional terms, due for example to viscosity and heat conduction, may be added)

$$\dot{U}^{(i)} = \dot{U}^{mol(i)} + \dot{U}^{mes(i)} + \dot{U}^{mac(i)} \tag{2.7}$$

and include molecular scale, mesoscale, and macroscale terms. The macroscale and molecular terms are ($P''^{(i)}$ is a molecular ensemble pressure)

$$\dot{U}^{mac(i)} = -U_o^{(i)} \sum_{j=1}^{n} \left(\frac{\zeta^{R(i,j)}}{\zeta^{(i,j)}} \right)^3 \frac{\dot{\zeta}^{(i,j)}}{\zeta^{(i,j)}} W^{(i,j)} \tag{2.8}$$

$$\dot{U}^{mol(i)} = \alpha^{(i)} \frac{m^{(i)} P''^{(i)}}{\rho^{(i)2}} \dot{\rho}^{(i)} \tag{2.9}$$

where $U_o^{(i)}$ is a repulsion potential energy and the coefficients $\alpha^{(i)}$ model the transition from an intact to a fragmented state. The later coefficients and the mesoscale terms $\dot{U}^{mes(i)}$ are

$$\dot{U}^{mes(i)} = \sum_{j=1}^{n_e} \frac{m^{(i,j)}}{m^{(i)}} (1 - d^{(j)}) \nu^{(j)} \mathbf{T}'^{(j)} : \mathbf{D}^{(j)} \tag{2.10}$$

where

$$\alpha^{(i)} = 1 - \sum_{j=1}^{n_e} \frac{m^{(i,j)}}{m^{(i)}}(1 - d^{(j)}) \tag{2.11}$$

and $m^{(i,j)}$ is an element mass fraction, $\mathbf{D}^{(j)}$ is the macroscale rate of deformation tensor, $\mathbf{T}'^{(j)}$ is a mesoscale true stress tensor, $d^{(j)}$ is an element damage variable, and $\nu^{(j)}$ is an element volume.

The rate of deformation for each macroscale element may be expressed as a function of the particle positions and velocities, using

$$\mathbf{D}^{(j)} = \sum_{k=1}^{n} \mathbf{A}^{(j,k)}\dot{\mathbf{c}}^{(k)}, \qquad \mathbf{A}^{(j,k)} = \mathbf{A}^{(j,k)}(\mathbf{c}^{(k)}) \tag{2.12}$$

The final nonholonomic constraints take the form

$$\dot{U}^{(i)} = \sum_{j=1}^{n} \left(\mathbf{a}^{c(i,j)T}\dot{\mathbf{c}}^{(j)} + \mathbf{a}^{e(i,j)T}\dot{\mathbf{e}}^{(j)}\right) \tag{2.13}$$

where the coefficients have the functional dependence

$$\mathbf{a}^{c(i,j)} = \mathbf{a}^{c(i,j)}(\mathbf{c}^{(k)}, \mathbf{e}^{(k)}, d^{(k)}, P''^{(k)}, \mathbf{T}'^{(k)}) \tag{2.14}$$

$$\mathbf{a}^{e(i,j)} = \mathbf{a}^{e(i,j)}(\mathbf{c}^{(k)}, \mathbf{e}^{(k)}, d^{(k)}, P''^{(k)}) \tag{2.15}$$

Note that the constraints serve to link the scales, since the coefficients of the generalized velocities will determine generalized forces in the momentum balance equations.

The canonical macroscale Hamilton's equations are

$$\dot{\mathbf{p}}^{(i)} = \mathbf{q}^{c(i)}, \quad \dot{\mathbf{c}}^{(i)} = m^{(i)-1}\,\mathbf{p}^{(i)}, \quad 0 = -\frac{\partial H}{\partial U^{(i)}} + q^{U(i)} \tag{2.16}$$

$$\dot{\mathbf{h}}^{(i)} = -\mathbf{J}^{(i)-1}\mathbf{h}^{(i)} \times \mathbf{h}^{(i)} + \frac{1}{2}\mathbf{G}^{(i)}\mathbf{q}^{e(i)}, \quad \dot{\mathbf{e}}^{(i)} = \frac{1}{2}\mathbf{G}^{(i)T}\mathbf{J}^{(i)-1}\mathbf{h}^{(i)} \tag{2.17}$$

where $\mathbf{G}^{(i)}$ depends only on the Euler parameters and the generalized nonconservative forces $\mathbf{q}^{c(i)}$, $\mathbf{q}^{e(i)}$, and $q^{U(j)}$ are determined from the nonholonomic constraints. Since the degenerate Hamilton's equations for the $U^{(i)}$ allow the Lagrange multipliers (associated with the constraints) to be determined in closed form, the final formulation will take a state-space form. The nonconservative generalized forces may be computed as (the generalized force associated with $U^{(i)}$ is one)

$$\mathbf{q}^{c(i)} = -\sum_{j=1}^{n} \left(\mathbf{a}^{c(i,j)} + \mathbf{a}^{c(j,i)}\right), \quad \mathbf{q}^{e(i)} = -\sum_{j=1}^{n} \mathbf{a}^{e(i,j)} \tag{2.18}$$

The effects of external loads may be added to the model by introducing an appropriate virtual work expression.

2.4 Mesoscale Model

The mesoscale model is an array of large strain Lagrangian finite elements, a unit cell of the mass represented in a macroscale element. (*There is one mesoscale unit cell per macro element; superscripts denoting the unit cell are omitted, for clarity*). The mesoscale Hamiltonian for a generic unit cell, with n'_e finite elements and n'_n interior nodes, is

$$H' = T' + V' = \frac{1}{2}\mathbf{p}'^{T}\mathbf{M}'^{-1}\mathbf{p}' + \sum_{i=1}^{n'_e} U'^{(i)}, \qquad \mathbf{p}' = \mathbf{M}'\dot{\mathbf{c}}' \tag{2.19}$$

where $\mathbf{M}'$ is the mass matrix, the element internal energies ($U'^{(i)}$) are state variables, $\mathbf{p}'$ is the momentum vector, and $\mathbf{c}'$ is the vector of nodal coordinates.

Motion of the boundary of the mesoscale unit cell is specified by the macroscale rate of deformation tensor. Hence the mesoscale unit cell models deformation, not rigid body translation or rotation. The present work employs no 'partitioning' of kinetic energy between the scales; instead independent momentum states are introduced at both the meso and molecular scales.

The macroscale deformation rate ($\mathbf{D}$) determines the velocities $\dot{\mathbf{b}}'^{(i)}$ of the nodes (of number n'_b) with coordinates $\mathbf{b}'^{(j)}$ on the mesoscale boundary

$$\dot{\mathbf{b}}'^{(i)} = \sum_{j=1}^{n'_b} \mathbf{B}'^{(i,j)} \mathbf{b}'^{(j)}, \qquad \mathbf{B}'^{(i,j)} = \mathbf{B}'^{(i,j)}(\mathbf{D}, \mathbf{b}'^{(k)}) \tag{2.20}$$

Then the boundary and internal node velocities determine the rates of deformation ($\mathbf{D}'^{(i)}$) in the mesoscale elements

$$\mathbf{D}'^{(i)} = \sum_{j\,=\,1}^{n'_b} \mathbf{A}'^{b(i,k)} \dot{\mathbf{b}}'^{(j)} + \sum_{j\,=\,1}^{n'_n} \mathbf{A}'^{c(i,k)} \dot{\mathbf{c}}'^{(j)} \tag{2.21}$$

where the coefficient matrices depend only on the nodal coordinates. The nodal coordinates also determine the mesoscale strains ($\mathbf{E}'^{(i)}$). Assuming an additive decomposition of the strain into elastic and plastic parts completes the mesoscale kinematic framework:

$$\mathbf{E}'^{(i)} = \mathbf{E}'^{(i)}(\mathbf{b}'^{(j)}, \mathbf{c}'^{(j)}), \qquad \mathbf{E}'^{(i)} = \mathbf{E}'^{e(i)} + \mathbf{E}'^{p(i)} \tag{2.22}$$

The evolution equations for the mesoscale internal energies are (additional terms, due for example to viscosity or heat conduction, may be added)

$$\dot{U}'^{(i)} = \dot{U}'^{ese(i)} + \dot{U}'^{irr(i)} \tag{2.23}$$

and include elastic strain energy and irreversible entropy production (plasticity) terms. For the preceding kinematics,

$$\dot{U}'^{ese(i)} = \nu_o'^{(i)} \mathbf{S}'^{(i)} : \dot{\mathbf{E}}'^{e(i)}, \quad \dot{U}'^{irr(i)} = \nu_o'^{(i)} \mathbf{S}'^{(i)} : \dot{\mathbf{E}}'^{p(i)} \tag{2.24}$$

where $\mathbf{S}'^{(i)}$ is a second Piola-Kirchoff stress tensor and $\nu_o'^{(i)}$ is a reference volume. For simple elastic-viscoplastic materials, the constitutive relations are

$$\mathbf{S}'^{(i)} = \mathbf{S}'^{(i)}(\mathbf{E}'^{e(i)}, U'^{(i)}), \quad \dot{\mathbf{E}}'^{p(i)} = \eta'^{(i)}(U'^{(i)}, \epsilon'^{p(i)})\, \mathbf{C}'^{(i)} \mathbf{S}'^{(i)} \mathbf{C}'^{(i)} \tag{2.25}$$

where $\eta'^{(i)}$ is a flow coefficient, $\epsilon'^{p(i)}$ is an accumulated plastic strain, and $\mathbf{C}'^{(i)} = \mathbf{F}'^{(i)T} \mathbf{F}'^{(i)}$ is a right Cauchy-Green strain tensor.

The canonical mesoscale Hamilton's equations are

$$\dot{\mathbf{p}}'^{(i)} = \mathbf{q}'^{(i)}, \quad \dot{\mathbf{c}}' = \mathbf{M}'^{-1}\, \mathbf{p}', \quad 0 = -\frac{\partial H'}{\partial U'^{(i)}} + q'^{U(i)} \tag{2.26}$$

where $\mathbf{q}'^{U(i)}$ and $q'^{U(i)}$ are generalized nonconservative forces. The mesoscale constraints take the form

$$\dot{U}'^{(i)} = \mathbf{A}'^{D(i)} : \mathbf{D} + \sum_{j=1}^{n_n'} \mathbf{a}'^{c(i,j)T} \dot{\mathbf{c}}'^{(j)} \tag{2.27}$$

where $\mathbf{A}'^{D(i)}$ and $\mathbf{a}'^{c(i,j)}$ are functions of $\mathbf{b}'^{(i)}$,$\mathbf{c}'^{(i)}$,$\mathbf{E}'^{p(i)}$, and $U'^{(i)}$.

These constraints determine the generalized forces $\mathbf{q}'^{(i)}$ (the generalized forces $q'^{U(i)}$ are one) and the average true stress ($\mathbf{T}'$) for the mesoscale unit cell as

$$\mathbf{q}'^{(i)} = -\sum_{j=1}^{n_n'} \left(\mathbf{a}'^{c(i,j)} + \mathbf{a}'^{c(j,i)} \right), \quad \mathbf{T}' = \frac{1}{\nu'} \sum_{j=1}^{n_e'} \mathbf{A}'^{D(j)} \tag{2.28}$$

where ν' is the mesoscale model volume.

2.5 Molecular Scale Model

The molecular scale model is based on a novel nonholonomic formulation of reacting molecular dynamics [4–6]. The Hamiltonian (for n'' spherical particles) is

$$H'' = T'' + V'' = \sum_{i=1}^{n''} \frac{\mathbf{p}''^{(i)2}}{2m''^{(i)}} + V''; \quad \mathbf{p}''^{(i)} = m''^{(i)}\dot{\mathbf{c}}''^{(i)} \tag{2.29}$$

The molecular potential energy (V'') is computed by integrating

$$\dot{V}'' = \dot{V}^{sig} + \dot{V}^{cou} + \dot{V}^{vdw} + \dot{V}^{ext} \tag{2.30}$$

where the terms represent chemical (two-body bonds, three-body and four-body bonds may be added), Coulomb, and van der Waals effects, as well as external loading of the ensemble control volume. *There is one ensemble for each macroscale particle (the macro superscript is omitted).* This formulation provides an energy-conserving description of bond breaking and forming, and allows for step cutoff functions, state dependent bond stiffnesses and equilibrium bond lengths, and other nonlinear effects.

To illustrate the morphing potentials, consider the two-body, Coulomb, and Van der Waals terms. Previous reacting molecular dynamics work has attempted to describe such potentials with analytic functions (holonomic formulation), for example

$$V^{sig} = \frac{1}{4}\sum_{i=1}^{n''}\sum_{j=1}^{n''} b_{ij}(\mathbf{c}''^{(k)})K_{ij}(r_{ij} - r_{ij}^{o})^2, \; V^{cou} = \frac{1}{4}\sum_{i=1}^{n''}\sum_{j=1}^{n''} \frac{C\, q_i q_j}{r_{ij}} \tag{2.31}$$

in which bond orders b_{ij} vary with position. As a result, non-analytic functions (e.g. step cutoffs) are inadmissible and parameter adjustments (made to equilibrium bond lengths, charges, etc.) violate conservation of energy. Adopting a nonholonomic approach, one can instead write

$$\dot{V}^{sig} = \frac{1}{2}\sum_{i=1}^{n''}\sum_{j=1}^{n''} w_{ij} b_{ij} K_{ij}(r_{ij} - r_{ij}^{o}) \frac{(\mathbf{c}''^{(i)} - \mathbf{c}''^{(j)})}{r_{ij}} \cdot (\dot{\mathbf{c}}''^{(i)} - \dot{\mathbf{c}}''^{(j)}) \tag{2.32}$$

where the step cutoff function w_{ij}, bond order b_{ij}, equilibrium bond length r_{ij}^{o}, and bond stiffness K_{ij} may all depend on the states.

In the case of the Coulomb potential,

$$\dot{V}^{cou} = -\frac{1}{4}\sum_{i=1}^{n''}\sum_{j=1}^{n''} \frac{C\, q_i q_j}{r_{ij}^2}\, w_{ij} \frac{(\mathbf{c}''^{(i)} - \mathbf{c}''^{(j)})}{r_{ij}} \cdot (\dot{\mathbf{c}}''^{(i)} - \dot{\mathbf{c}}''^{(j)}) \tag{2.33}$$

both the introduction of step cutoff functions (w_{ij}) and the adjustment of charges (q_i) at each time step are allowed (on physical grounds, total charge must be conserved). An example is an electronegativity equilibration calculation $q_i = q_i(b_{ij}, \mathbf{c}''^{(k)})$, performed at each time step. Similarly, the range and strength of the van der Waals interactions may be adjusted (for example, σ and ε may be taken to vary with the state variables) using

$$\dot{V}^{vdw} = -\sum_{i=1}^{n''}\sum_{j=1}^{n''} \frac{6\,\varepsilon}{r_{ij}}\, w_{ij} \left[2\left(\frac{\sigma}{r_{ij}}\right)^{12} - \left(\frac{\sigma}{r_{ij}}\right)^{6}\right] \frac{(\mathbf{c}''^{(i)} - \mathbf{c}''^{(j)})}{r_{ij}} \cdot (\dot{\mathbf{c}}''^{(i)} - \dot{\mathbf{c}}''^{(j)}) \tag{2.34}$$

The molecular ensemble control volume evolves to match the density of the associated macroscale particle. Using a wall potential in VDW form

$$\dot{V}^{ext} = -12\,\varepsilon \sum_{i=1}^{n''}\sum_{j=1}^{3} \left[\frac{\hat{w}_{ij}}{\hat{r}_{ij}}\left(\frac{\sigma}{\hat{r}_{ij}}\right)^{12} (\dot{c}_j''^{(i)} - \dot{L}) + \frac{\tilde{w}_{ij}}{\tilde{r}_{ij}}\left(\frac{\sigma}{\tilde{r}_{ij}}\right)^{12} (\dot{c}_j''^{(i)} + \dot{L})\right] \tag{2.35}$$

where $\hat{r}_{ij} = c_j^{\prime\prime(i)} - L$, $\tilde{r}_{ij} = c_j^{\prime\prime(i)} + L$, $\hat{w}_{ij}$ and $\tilde{w}_{ij}$ are cutoff functions, and the control volume is a cube with volume $\nu^{''} = 8\,L^3$. Hence the final constraint equation for the potential energy evolution takes the form

$$\dot{V}'' = \frac{m''}{\rho''^2}\dot{\rho}\sum_{i=1}^{n''} a''^{L(i)} + \sum_{i=1}^{n''}\sum_{j=1}^{n''} \mathbf{a}''^{c(i,j)T}\dot{\mathbf{c}}''^{(j)}, \quad \dot{\nu}^{''} = -\frac{m''}{\rho''^2}\dot{\rho}'' = 24\,L^2\,\dot{L} \tag{2.36}$$

where $a''^{L(i)} = a''^{L(i)}(\mathbf{c}''^{(j)}, L)$, $\mathbf{a}''^{c(i,j)} = \mathbf{a}''^{c(i,j)}(\mathbf{c}''^{(k)}, L)$, and $\dot{\rho}'' = \dot{\rho}$.

The canonical molecular scale Hamilton's equations are

$$\dot{\mathbf{p}}''^{(i)} = \mathbf{q}''^{c(i)}, \quad \dot{\mathbf{c}}''^{(i)} = m''^{(i)-1}\,\mathbf{p}''^{(i)}, \quad 0 = -\frac{\partial H''}{\partial V''} + q'' \tag{2.37}$$

The constraint determines the generalized forces (the generalized force q'' is one) and the pressure for the molecular ensemble (P'') using

$$\mathbf{q}''^{c(i)} = -\sum_{j\,=\,1}^{n''} \mathbf{a}''^{c(j,i)}, \quad P'' = \sum_{j\,=\,1}^{n''} a''^{L(j)} \tag{2.38}$$

Since the formulation is fully Lagrangian, reactions are modeled explicitly, at the molecular level. However, additional physics (e.g. species concentration dependence of the mesoscale material properties) may be added.

2.6 Summary

This chapter has developed the first unified discrete Hamiltonian approach to synchronous multiscale simulation of reacting shock physics. It incorporates a fundamentally new approach to reacting molecular dynamics; some advantages of the reacting molecular dynamics formulation include:

1. General nonlinear effects, such as state dependent equilibrium bond lengths, are admitted.

2. Electronegativity equilibration calculations may be properly incorporated into the simulation.

3. Integer (step) changes in bond order are permitted; this can eliminate partial bonding and over-coordination, and ambiguity in the reacted state of the system is eliminated.

4. Energy is conserved, hence the method offers a sound and flexible foundation for further development; an example might include the introduction of additional energy domains (electric or magnetic loads).

Some advantages of the multiscale formulation include:

1. A unified model formulation approach, based on nonholonomic thermomechanical Hamiltonian methods, is applied at all scales.

2. No reference is made to any partial differential equations; hence the introduction of non-continuum effects, such as fracture and fragmentation, is greatly facilitated.

3. General geometric and material nonlinearities are admitted.

4. The method offers a sound and flexible foundation for further development; an example might include the introduction of additional scales (an electronic structure scale, or additional mesoscales).

Future research opportunities include extension of the formulation to additional energy domains, additional scales, and additional reference frames.

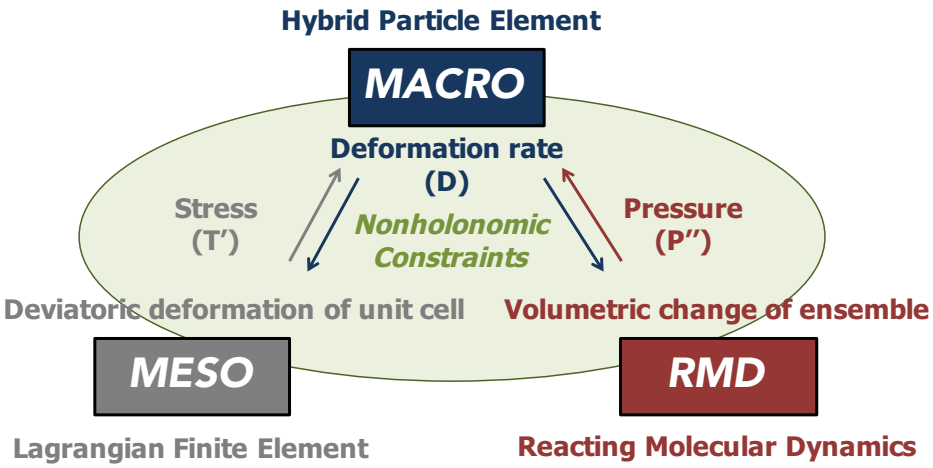

Figure 2.1: Structure of the synchronous multiscale model

Chapter 3

Asynchronous Multiscale Approach

3.1 Introduction

Previous research on the development of reacting shock physics models has employed a wide variety of techniques. Continuum finite element, mesoscale particle, and molecular dynamics methods have all been employed with success, but at very different scales. The systematic merger of these methods has been hindered by dramatic differences in the model formulation techniques normally used at the different scales. They range from weighted residual solution methods for partial differential equations (at the continuum scale) to discrete Hamiltonian methods (at the molecular scale). Extending previous research [18, 31], this research is developing the first unified approach to multiscale reacting shock physics simulation.[2]

The formulation is discrete nonholonomic Hamiltonian, at all scales. At the meso scale, the rate law for the particle internal energy coordinates is a function of the particle velocities, so that the formulation is inherently nonholo-

[2]This chapter is based on the previous publication: Lee, S., and Fahrenthold, E.P., "Nonholonomic Hamiltonian method for meso-macroscale simulations of reacting shocks," *AIP Conference Proceedings*, Vol. 1793, 2017, pp.080006. The co-author is an expert in finite element and hybrid particle element methods, the dissertation author's expertise is in the integration of these methods to form multiscale numerical methods.

nomic. At the macro scale, the rate laws for the element masses and the element internal energy coordinates are functions of the element nodal velocities, so that the formulation is inherently nonholonomic. Although Hamiltonian methods are typically associated with Lagrangian frames and the molecular scale, this research incorporates both Eulerian and Lagrangian frames, and a combination of finite element, particle, and hybrid particle-element kinematics. General geometric and material nonlinearities are included. The general theoretical approach, described in this chapter only at the meso and macro scales, may be extended to address a wide range of computational materials design problems.

3.2 Hamiltonian Formulation

The paragraphs which follow outline a one dimensional formulation. The development is based on general Hamiltonian modeling concepts (e.g. generalized conservative and nonconservative forces, true and quasi coordinates, holonomic and nonholonomic systems, virtual work, etc.) [24] as well as previous work extending general Hamiltonian formulations to shock physics applications, in both Eulerian and Lagrangian frames [18, 31]. Interested readers are referred to the last three cited references (and numerous papers cited therein) for a more detailed description of the general method.

As indicated in Figure 3.1, the macroscale model is composed of Eulerian finite elements, while the mesoscale model represents a unit cell of one Eulerian finite element. The mesoscale model is composed of a Lagrangian

hybrid particle-finite element array; voids may be represented explicitly (Figure 3.1, left) or implicitly (Figure 3.1, right). In the later case each particle is a mixture of a solid and a gas. The macroscale Hamiltonian (with n_e finite elements and n_n nodes) is [18, 28]

$$H = T + V = \frac{1}{2}\,\mathbf{p}^T\mathbf{M}^{-1}\mathbf{p} + \sum_{i=1}^{n_e} U^{(i)}, \qquad \mathbf{p} = \mathbf{M}\mathbf{v} \tag{3.1}$$

where $\mathbf{M}$ is the mass matrix, the element internal energies ($U^{(i)}$) are state variables, $\mathbf{p}$ is the momentum vector, and $\mathbf{v}$ is the n_n dimensional vector of nodal velocities. To obtain a system level model, the macroscale Hamiltonian is combined with the canonical Hamilton's equations, a virtual work expression, and nonholonomic constraints describing the evolution of the element internal energies, the element masses ($m^{(i)}$), and the element species mass fractions ($s^{(i,j)}$). The canonical macroscale Hamilton's equations are [29]

$$\dot{\mathbf{p}} = \mathbf{q}, \quad \mathbf{0} = -\frac{\partial H}{\partial \mathbf{U}} + \mathbf{q}^U, \quad \mathbf{0} = -\frac{\partial H}{\partial \mathbf{m}} + \mathbf{q}^m, \quad \mathbf{0} = -\frac{\partial H}{\partial \mathbf{s}} + \mathbf{q}^s \tag{3.2}$$

where $\mathbf{q}, \mathbf{q}^U, \mathbf{q}^m, \mathbf{q}^s$ are generalized nonconservative forces determined by the virtual work and the nonholonomic constraints. The virtual work, expressed in terms of the quasi-coordinates ($\mathbf{w}$) defined by $\mathbf{v} = \dot{\mathbf{w}}$, balances the rate of change of kinetic energy in the elements and at the nodes [18]. The nonholonomic constraints, for example the evolution equations for the macroscale internal energies (including convection and irreversible entropy production terms)

$$\dot{\mathbf{U}} = \dot{\mathbf{U}}_{cvc} + \dot{\mathbf{U}}_{irr} \tag{3.3}$$

determine additional generalized nonconservative forces. The degenerate Hamilton's equations for $\mathbf{m}$, $\mathbf{s}$, and $\mathbf{U}$ determine in closed form the Lagrange multipliers associated with the nonholonomic contstraints, and complete the macroscale formulation.

The mesoscale Hamiltonian takes the same functional form used in the macroscale case, but with $\mathbf{M}$ a diagonal mass matrix (the diagonal elements are the particle masses) and $\mathbf{v} = \dot{\mathbf{c}}$, where $\mathbf{c}$ is a vector of n_n particle center of mass coordinates. The Lagrangian particles are located at the finite element nodes, while the elements quantify the large strain Lagrangian forces associated with tension and shear. The canonical mesoscale Hamilton's equations are [31]

$$\dot{\mathbf{p}} = \mathbf{q}, \quad \dot{\mathbf{c}} = \mathbf{M}^{-1}\mathbf{p}, \quad \mathbf{0} = -\frac{\partial H}{\partial \mathbf{U}} + \mathbf{q}^U \tag{3.4}$$

where $\mathbf{q}, \mathbf{q}^U$ are generalized nonconservative forces and $U^{(i)}$ is a particle internal energy. The internal energy evolution equations are again nonholonomic constraints

$$\dot{\mathbf{U}} = \dot{\mathbf{U}}_{wrk} + \dot{\mathbf{U}}_{irr} \tag{3.5}$$

and in this case include mechanical power and irreversible entropy production terms. The degenerate Hamilton's equations for the internal energies determine the Lagrange multipliers associated with the constraints, and a virtual work expression is introduced to account for external loads [31]. The final evolution equations for the particle positions, internal energies, and momenta take an explicit state space form. Since the mesoscale formulation incorporates true Lagrangian modeling of fracture and fragmentation, numerical fracture

and tensile instability are eliminated. The particle method used here employs singular interpolation kernels, avoiding particle streaming; the method is routinely used to model shock physics problems at orbital debris impact velocities [15, 16].

Note that no reference is made, at either scale, to partial differential equations; hence the introduction of non-continuum effects, such as fracture and fragmentation, is greatly facilitated. Large strain kinematics, general chemical-themomechanical coupling, plastic compaction of voids, mixed solid-gas thermodynamics, general ignition and reaction kinetics, and nonuniform void distributions may be modeled at either scale. Finally the multiscale method offers a sound and flexible foundation for further development; examples might include the introduction of additional energy domains or scales. The next section describes a set of example simulations.

3.3 Example Simulations

The simulations which follow illustrate application of the meso-macroscale models to test problems of central importance in multiscale modeling of explosives. The mesoscale simulations model thermomechanical wall shocks in an inert medium containing voids, and have application in the prediction of 'hot spots' which may lead to explosive ignition [81]. The macroscale simulations model first thermomechanical and second reacting themomechanical wall shocks, and have application in the prediction of shock induced detonation in energetic materials [85]. Since the examples model shock compression, tensile

fracture is not simulated. However, the hybrid-particle element method used at the mesoscale has been validated in three dimensional simulations of shock fragmentation [31]. Fracture and fragmentation at the macroscale may be represented using a history state variable dependent constitutive model [23].

The first hot spot (mesoscale) model employs an explicit representation of voids, as gaps between solid particles. The simulation shown in Figure 3.2 models a 1 km/s impact in RDX, for an array of particles incorporating two intervals with 20% void fraction. Particle size in this simulation is 2.00 μm, so that the modeled void size is 400 nm, in the mid range of those reported for RDX-based explosives [69]. The simulation assumes a simplified Mie-Grüneisen equation of state for both reactant and product.

$$P = C_s^2 (\rho - \rho_o) + \gamma \rho_o (e - e_o) \tag{3.6}$$

$$\theta = \frac{1}{C_v} (e - e_o) \tag{3.7}$$

where P denotes a pressure, θ denotes a temperature, C_s denotes a sound speed, ρ denotes a density, γ denotes a Grüneisen coefficient, and e denotes an internal energy per unit mass. ρ_o and e_o are reference density and internal energy respectively. The coefficients are listed in Table 3.1.

The simulation results show pronounced temperature peaks in the void containing regions. Note that the hybrid-particle element method used at the mesoscale eliminates the need for legacy contact-impact modeling methods (such as master-slave nodes) by representing all contact-impact physics using singular particle kernels [31]; contact forces are thereby determined from the

particle pressures, and penalty springs are avoided.

The second hot spot (mesoscale) model employs mixture theory to simulate mixed solid-gas particle thermodynamics. In this case the solid and the gas are assumed to have the same pressure and temperature (other thermodynamics may be assumed). The simulation shown in Figure 3.3 models a 1 km/s impact in RDX, for an array of particles incorporating two intervals with 10% gas volume fraction. Particle size in this simulation is 1.56μm, so that the modeled void size is 156 nm, in the mid range of those reported for RDX-based explosives [69]. The simulation assumes a simplified Mie-Grüneisen equation of state for both reactant and product. The coefficients are listed in Table 3.1. Again the simulation results show pronounced temperature peaks in the void containing regions.

The first macroscale validation simulation models a 5 km/s wall shock in an inert material, assuming the Mie-Grüneisen equation of state parameters are those of RDX. The simulation results are in good agreement with the exact solution (shown by the dotted lines in Figure 3.4), computed by solving the Rankine-Hugoniot equations.

The second validation simulation (Figure 3.5) models a wall shock to detonation in TNT. In this case, the velocity field in the vicinity of the wall is initialized to 5.6 km/s [36]. The simulation assumes JWL equations of state for the solid reactant and gas product, and an 'ignition and growth' model for the explosive (both are taken from the published literature [12]).

The JWL equations of state for both solid reactant and gas product in TNT [11] are defined as follows:

$$P = A\left(1-\frac{\omega}{R_1\mu}\right)e^{-R_1\mu} + B\left(1-\frac{\omega}{R_2\mu}\right)e^{-R_2\mu} + \omega\frac{(e+e_i)}{\mu} \quad (3.8)$$

$$\theta = \frac{1}{C_v}(e-e_o) \quad (3.9)$$

where

$$\mu = \frac{\rho_o}{\rho} \quad (3.10)$$

and the JWL coefficients A, B, R_1, R_2, ω, and e_i are listed in Table 3.2. The following mixture relation interpolates between solid reactant and gas product.

$$P = (1-F)P_{solid} + FP_{gas} \quad (3.11)$$

The ignition and growth model for TNT [11] is

$$\frac{dF}{dt} = \underbrace{I(1-F)^b\left(\frac{\rho}{\rho_o}-1-a\right)^x}_{0<F<F_{igmax}} + \underbrace{G_1(1-F)^c F^d P^y}_{0<F<F_{G_1max}} + \underbrace{G_2(1-F)^e F^g P^z}_{F_{G_2min}<F<1} \quad (3.12)$$

where F denotes a reacted progress variable and P denotes a pressure. All the coefficients are listed in Table 3.3.

The simulation results for the particle pressure and particle velocity in the detonating explosive, plotted in Figure 3.5, show good agreement with published experimental values [11, 36] for the von Neumann spike pressure (25 GPa) and particle velocity (2,310 m/s) in detonating TNT.

3.4 Summary

Application of nonholonomic Hamiltonian methods offers the first unified model formulation approach to multiscale simulation of energetic materials. Models developed using this approach can be used to predict temperature and pressure conditions at mesoscale hot spots and simulate macroscale shock to detonation in condensed phase explosives. The succeeding chapters are integrating these meso-macroscale simulations with a new reacting molecular dynamics formulation, developed using a similar nonholonomic Hamiltonian methodology.

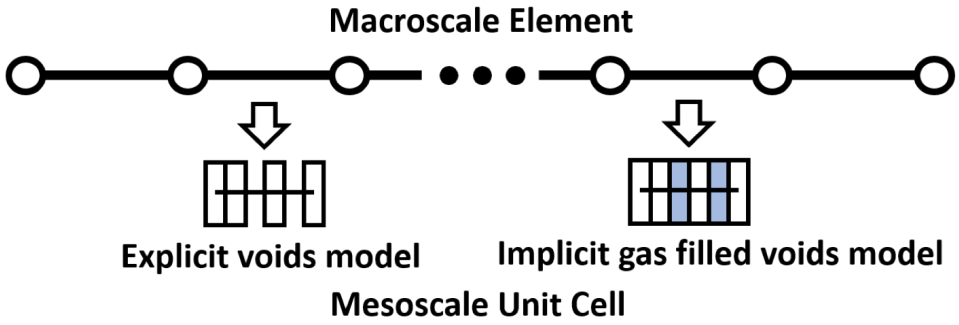

Figure 3.1: Structure of the meso-macroscale model.

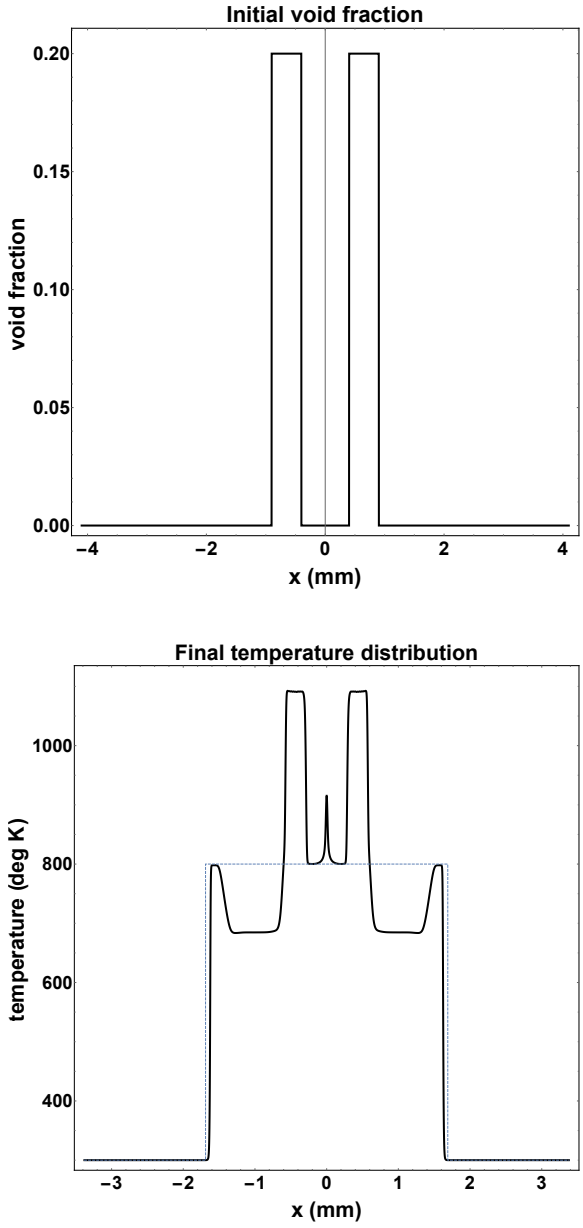

Figure 3.2: Shock induced hot spot for a 1 km/s impact in RDX; voids are modeled explicitly (stop time 0.703 microseconds). The dotted line (lower figure) shows the exact solution for the case without voids.

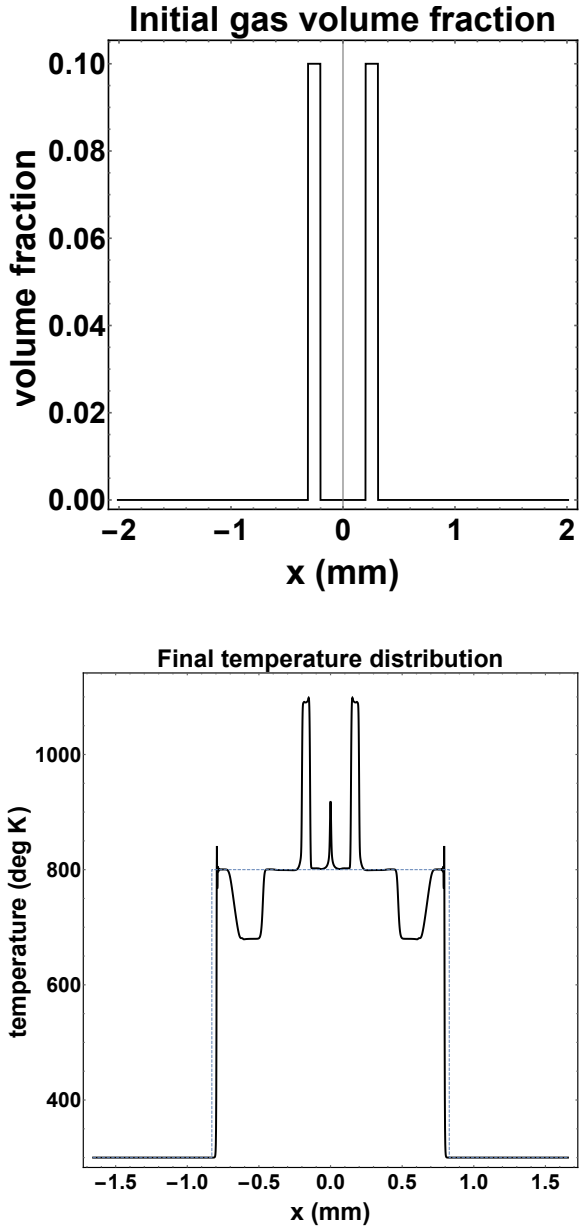

Figure 3.3: Shock induced hot spot for a 1 km/s impact in RDX; gas-filled voids (stop time 0.351 microseconds). The dotted line (lower figure) shows the exact solution for the case without gas-filled voids.

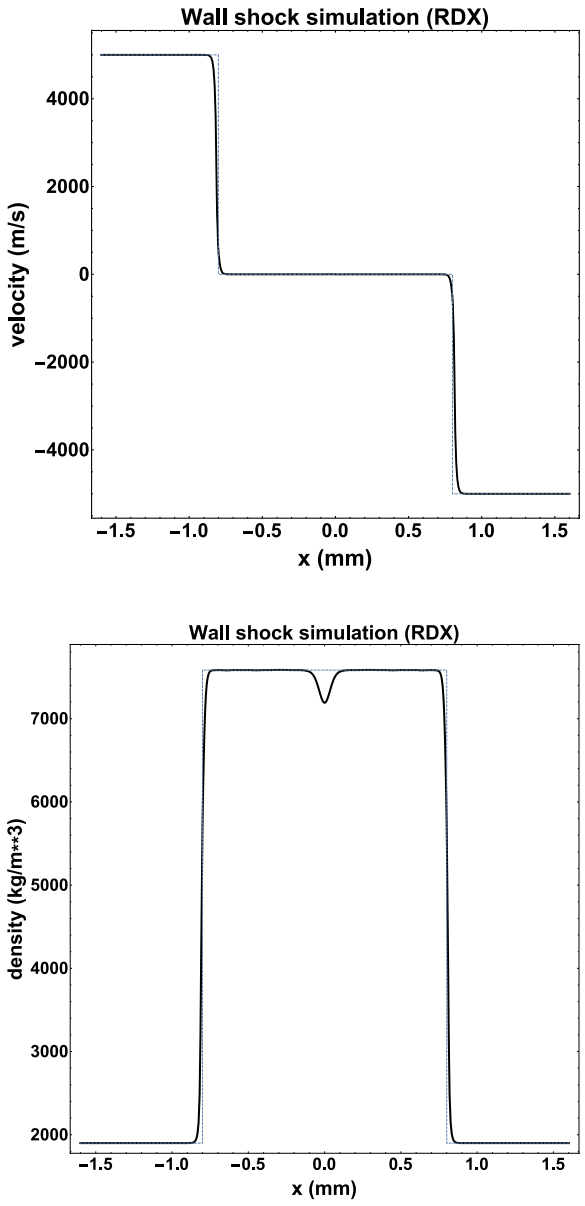

Figure 3.4: Macroscale simulation of a 5 km/s wall shock; inert material with the Mie Grüneisen properties of RDX (stop time 0.480 microseconds). The dotted lines show the exact solution, computed by solving the Rankine-Hugoniot equations.

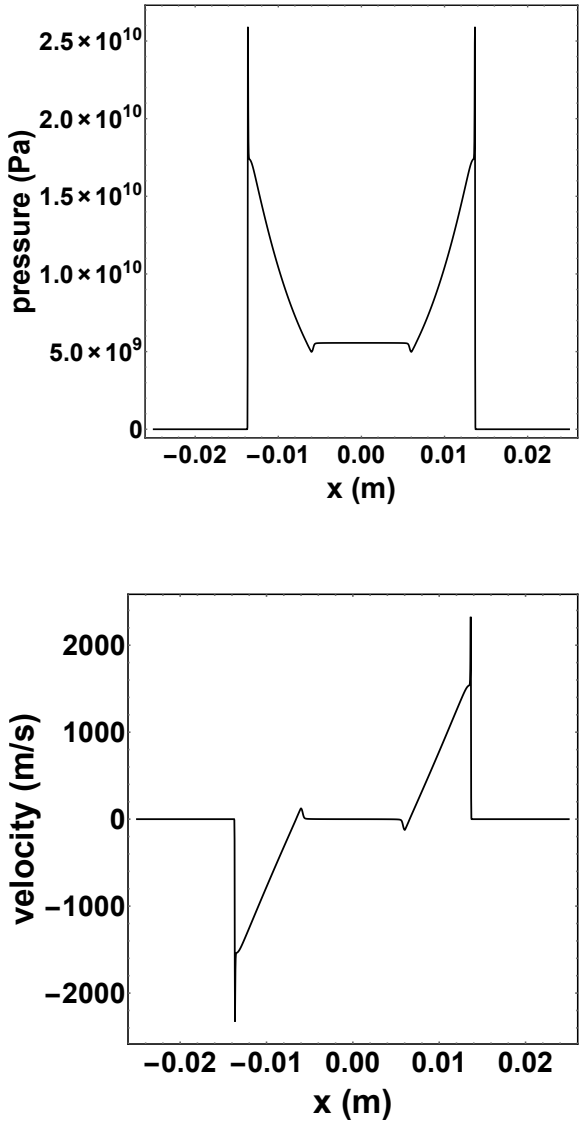

Figure 3.5: Macroscale simulation of shock induced detonation in TNT (stop time 2.00 microseconds). Peak values for pressure (upper figure) and particle velocity (lower figure) are in good agreement with the corresponding experimental values [11, 36] of 25 GPa and 2,310 m/s for detonating TNT.

Table 3.1: Equation of state parameters for RDX.

Density ρ_o	1806 kg/m^3	[80]
Sound speed C_s	2620 m/s	[35]
Grüneisen γ	2.2	[35]
Specific Heat C_v	1256 J/KgK	[1]
Melting temperature θ_m	478 K	[13]
Young's Modulus E	18.4 GPa	[9]
Yield Stress Y	300 MPa	[9]

Table 3.2: Equation of state parameters for TNT: solid reactant and detonation gas products [11].

	Reactant	Product
A	17101 GPa	673.1 GPa
B	-3.745 GPa	21.988 GPa
R_1	9.8	5.4
R_2	0.98	1.8
ω	0.5675	0.3
C_v	2.70386×10^{-3} GPa/K	1×10^{-3} GPa/K
ρ_o	1624 kg/m^3	1624 kg/m^3
e_i	0 GPa/m^3	7.0 GPa/m^3

Table 3.3: Ignition and growth model parameters for TNT [11].

I	$5.0 \times 10^7\ s^{-1}$
a	0
b	0.667
x	4.0
G_1	$3.6 \times 10^8\ Mbar^{-1.2}s^{-1}$
y	1.2
c	1.0
d	0.667
G_2	$0\ Mbar^{-1}s^{-1}$
e	1
g	0.111
z	1.0
F_{igmax}	0.03
F_{G1max}	1.0
F_{G2max}	0
ρ_o	$1624\ kg/m^3$

Chapter 4

Incorporation of Chemistry Models and Equations of State

The molecular, mesoscale, and macroscale component models must now be integrated, in order to obtain an engineering model of the detonation process for use in materials design or other applications. A variety of different integration methods have been developed [44, 52, 60, 83]. Their general utility may be evaluated on the basis of accuracy, computational cost, range of applicability, ease of use, or other criteria. It appears that no particular method has gained wide favor, suggesting that research on the development of well structured approaches to hierarchical multiscale modeling problems is well motivated.

4.1 Introduction

The integration approach suggested here may be summarized as follows:

1. Reacting molecular dynamics simulations are used to determine two chemistry models: (1) simplified initial reaction mechanisms and an associated kinetics model, describing decomposition of the explosive and the formation of explosive product intermediates, and (2) simplified fi-

nal reaction mechanisms and associated kinetic relations and parameters, describing formation of the final explosive products.

2. Reacting molecular dynamics simulations are used to determine an equation of state for the explosive product intermediates, by either: (1) formulating a tabulated equation of state, or (2) fitting coefficients to an analytic equation of state.

3. Mesoscale simulations incorporating the short time kinetic model and the explosive product intermediates equation of state are performed to develop an internal state variable model which: (a) relates local conditions at the hot spots to macroscale thermodynamic states, and (b) quantifies the time delay associated with the development of those hot spots.

4. Macroscale simulations incorporating the long time kinetic model (from reacting molecular dynamics) and an internal state variable model (from mesoscale simulations) of hot spot conditions are used to model shock to detonation.

The preceding integration approach is intended to replace the ignition and growth models widely employed in macroscale detonation simulations, replacing an essentially empirical detonation modeling component with one more directly connected to the detonation chemistry, facilitating the application of accumulated knowledge to the development of improved energetic materials.

Two particular tasks are critical to the successful implementation of the four step multiscale modeling approach just outlined. The first is the effective use of reacting molecular dynamics to formulate the required short time and long time kinetics models. Recent research [4] has applied a new formulation of reacting molecular dynamics to develop one such model; the reader is referred to the last cited reference for details, including reaction mechanisms, rate laws, and fitted coefficients for initial detonation products in the explosives. The second critical task is the formation of equation of state models which effectively employ both: (1) detonation products equations of state, (2) analytic models of the solid and long time explosive products, in meso and macro scale simulations incorporating general chemical kinetics. The paragraphs which follow describe new formulations.

4.2 Kinematics and Structure

The systematic approach of asynchronous multiscale incorporation is presented in this chapter. The multiscale structure includes three scales and two chemical kinetics models. The concise schematic is shown in Figure 4.1.

At the molecular scale, reacting molecular dynamics is used to develop the chemical kinetics models. Development of the new reacting MD method is not included in this dissertation. Interested readers are referred to the references [4–6] for a detailed description of new RMD method. The reacting MD develops two types of chemical kinetics models, for use at different scales. A short time chemistry model simulates detonation, and a long time chemistry

model starts with detonation products and simulates recombination to obtain final products.

At the mesoscale, a Lagrangian hybrid particle-element method is used to simulate 'hotspot' generation in the explosive, due to void collapse. The short time chemistry model obtained from the RMD simulation describes the mesoscale chemical kinetics. The results of the mesoscale simulation are used to develop an ignition process model, for use in simulating shock induced detonation at the macroscale.

At the macroscale, an Eulerian finite element method is used to simulate shock to detonation. The long time chemistry model obtained from the RMD simulation describes the macroscale chemical kinetics. An internal state variable model obtained from the mesoscale simulation describes initiation and growth of the detonation.

The research develops two distinct integration approaches, one for the meso and one for the macro scale. The first approach integrates the short time chemistry model into the mesoscale. The second approach integrates an ignition and growth model into the macroscale. Each approach employs decoupling strategies to address great disparities in the chemical and thermomechanical temporal and spacial scales, which otherwise lead to very stiff ODE models. These approaches are validated in later chapters.

Table 4.1 illustrates the time steps and length scales spanned by the integrated multiscale modeling approach. The integration time steps vary by

five orders of magnitude. The characteristic lengths vary by six orders of magnitude. Note that the difference between the meso and molecular scales is sufficiently close that additional integration strategies are not needed. Both macro and meso scale simulations utilize one dimensional discretization while the reacting MD simulation [4–6] incorporates three dimensional models.

Each integration approache will be described in the following sequence. Nonholonomic constraints and momentum balance equations are first presented. The chemical kinetics models are obtained from reacting MD simulation results. The ignition and growth model is obtained from the mesoscale. Equations of state are formulated to describe the mixtures of interest. Finally state equations are developed to complete the formulations.

4.3 Short Time Chemistry Model

The short time chemistry model describes decomposition of the solid explosives and generation of the intermediate reaction products. The kinetics apply to ignition and growth of a detonation so that the model is suitable to describe mesoscale hotspot simulation, replacing widely used empirical modeling methods. The state equations employ an explicit rate description of species concentration $\frac{dC}{dt}$ variations. Figure 4.2 (upper) shows the function of the short time chemistry model.

In the case of HMX, the simplified four-step reaction mechanism is as follows [6]:

$$
\begin{aligned}
C_4H_8N_8O_8 &\rightarrow 4NO_2 + 4CH_2 + 4N \\
NO_2 + CH_2 &\rightarrow NOH + COH \\
4COH &\rightarrow 0.35CO_2 + 1.65CO + 4H + 1.65O + 2C \\
4NOH &\rightarrow 1.7N_2 + 0.6N + 0.15H_2O + 1.35OH + 2.5O + 2.35H
\end{aligned}
$$

4.4 Long Time Chemistry Model

The long time chemistry model describes the transition from intermediate reaction products to the long term products observed in bomb calorimeter experiments. This is a relatively slow process, compared to the detonation physics. In the macroscale simulation, the kinetics model addresses the later part of a complete detonation process. Figure 4.2 (lower) shows the function of the long time chemistry model.

The long time chemistry model employs a temperature dependent species concentration $\frac{dC}{d\theta}$ rate law, to be integrated at the macroscale

$$
\frac{dC}{dt} = \underbrace{\frac{dC}{d\theta}}_{RMD} \underbrace{\frac{d\theta}{dt}}_{MACRO} \tag{4.1}
$$

where the rate of change of temperature $\frac{d\theta}{dt}$ is obtained from the macroscale state space model.

In the case of HMX, the simplified nine-step reaction mechanism is as follows [6]:

$$C + O \rightarrow CO \qquad CO + O \rightarrow CO_2 \qquad OH + H \rightarrow H_2O$$

$$N + N \rightarrow N_2 \qquad O + H \rightarrow OH \qquad N + 3H \rightarrow NH_3$$

$$C + C \rightarrow C_2 \qquad H + H \rightarrow H_2 \qquad H_2 + O \rightarrow H_2O$$

4.5 Ignition Process Model

An internal state variable model, developed from the mesoscale simulation, is used in the macroscale model to describe initiation and growth of the detonation.

The ignition progress variable f is obtained by integrating a rate relation (additional ignition criteria based on temperature and density may be included), as follows:

$$\dot{f} = \underbrace{\frac{df}{dP}}_{MESO} \underbrace{\frac{dP}{dt}}_{MACRO} u_s(P - P_{ign}) \tag{4.2}$$

where the pressure dependent term $\frac{df}{dP}$ is obtained from the mesoscale model. Here the mesoscale simulation lead to a simple functional form. The time rate of change of pressure $\frac{dP}{dt}$ is determined in the macroscale simulation. The ignition criteria employ a unit step form. An ignition pressure P_{ign} may be obtained from the published experimental literature [66]. This decoupling process avoids a small time step issue which may arise due to sharp differences between the meso and macro time and length scales.

4.6 State Interpolation

A composite mesoscale equation of state may take the form

$$P_{meso} = \lambda^{mes} P_{gas} + (1 - \lambda^{mes}) P_{solid} \tag{4.3}$$

$$\theta_{meso} = \lambda^{mes} \theta_{gas} + (1 - \lambda^{mes}) \theta_{solid} \tag{4.4}$$

where P and θ are pressure and temperature which are analytically defined, the subscripts *gas* and *solid* denote the gas and solid constituents, and λ^{mes} is a reaction progress variable defined by

$$\lambda^{mes} = \left(\sum_{i=1}^{n_s} w_i \lambda_i^{mes} \right) / \left(\sum_{i=1}^{n_s} w_i \right) \tag{4.5}$$

The parameters w_i are species weighting coefficients, n_s is the number of species, and λ_i^{mes} is

$$\lambda_i^{mes} = \left| \frac{C_i - C_i^0}{C_i^1 - C_i^0} \right| \tag{4.6}$$

where C_i^0 and C_i^1 denote the initial and intermediate concentrations for the ith species. The species concentrations are state variables in the mesoscale model, obtained from integration of the kinetics model.

In the mesoscale integration of the short time chemistry model, obtained from reacting MD simulations, the species concentration of the solid reactant is used to calculate a reaction progress variable λ^{mes} which appears in the equation of state.

At the macroscale level, the composite equation of state must incorporate a solid equation of state, a detonation products equation of state, and

a mixture equation of state for the long term explosive products. Here the transition from a solid to a gas (initial detonation products), post-initiation, is represented by

$$P_{macro} = f P_{gas} + (1 - f)\, P_{solid} \tag{4.7}$$

$$\theta_{macro} = f \theta_{gas} + (1 - f)\, \theta_{solid} \tag{4.8}$$

where ignition process variable $f = f(m, s)$ is a function of the species mass fractions. The reaction progress variable λ^{mac} associated with the long time chemical kinetics is used to interpolate between the detonation products equation of state and a mixture equation of state for the explosive end products

$$P_{gas} = \lambda^{mac} P_{mix} + (1 - \lambda^{mac})\, P_{det} \tag{4.9}$$

$$\theta_{gas} = \lambda^{mac} \theta_{mix} + (1 - \lambda^{mac})\, \theta_{det} \tag{4.10}$$

where the subscripts det and mix denote the detonation gas and final mixture gas products, and λ^{mac} is a reaction progress variable defined by

$$\lambda^{mac} = \left(\sum_{i=1}^{n_s} w_i \lambda_i^{mac} \right) / \left(\sum_{i=1}^{n_s} w_i \right) \tag{4.11}$$

The parameters w_i are species weighting coefficients, n_s is the number of species, and λ_i^{mac} is

$$\lambda_i^{mac} = \left| \frac{C_i - C_i^0}{C_i^1 - C_i^0} \right| \tag{4.12}$$

where C_i^0 and C_i^1 denote the intermediate and final concentrations for the ith species. Likewise, the species concentrations are state variables in the macroscale model, obtained from integration of the kinetics model.

As an example, the long time detonation products for HMX may be taken as [4, 6]

$$HMX(C_4H_8N_8O_8) \rightarrow C, O, CO, CO_2, OH, H, H_2O, N, N_2, NH_3, C_2, H_2 \tag{4.13}$$

while the long time detonation products for RDX may be taken as [6]

$$RDX(C_3H_6N_6O_6) \rightarrow C, O, CO, CO_2, OH, H, H_2O, N, N_2, C_2, H_2 \tag{4.14}$$

Adopting a simplified Mie-Grüneisen equation of state for the end products, in an Eulerian frame simulation [47], for each constituent which admits an analytic calculation of equation of state

$$P = \rho_o C_s^2 \left(\frac{\rho}{\rho_o} - 1 \right) + \gamma \rho_o \left(e - e_o \right) \tag{4.15}$$

$$\theta = \frac{1}{C_v}(e - e_o) + \theta_o \tag{4.16}$$

where C_s denotes speed of sound and γ is the Grüneisen Parameter. In the absence of experimental data, it may be estimated as [74]

$$\gamma = \frac{\alpha K_s}{C_P \rho_o} = \frac{\alpha C_s^2}{C_P} \tag{4.17}$$

where α is a volumetric thermal expansion coefficient, K_s is a bulk modulus, and C_p is a specific heat. Assuming thermal expansion in a gas [54] (p.88), [10] (p.326):

$$\alpha = \frac{1}{\theta_o} \tag{4.18}$$

where θ_o is a reference temperature and

$$\gamma = \frac{C_s^2}{C_P \theta_o} \tag{4.19}$$

Such estimates may then be compared to theoretical data [14].

The preceding discussion emphasizes the important role of multiscale modeling in characterizing the equation of state for the initial deformation products, as well as the detonation chemistry.

4.7 Summary

The integrated formulation includes the following advantages:
(1) Widely used 'ignition and growth models' are replaced by a mesoscale based ignition process model and molecular dynamics-derived chemistry models (introduced at both the meso and macro scales). (2) The temperature-based chemistry model used at the macroscale avoids the very small time steps typically associated with molecular based kinetics formulations. (3) The reaction progress variables employed in the equations of state calculations are based on species concentrations obtained from the chemical kinetics models, rather than empirical rate laws, and (4) equation of state calculations involving early time detonation products are obtained from molecular dynamics simulations.

Chapters 6 and 7 will address validation simulations by expanding the general methodology which has been elucidated in this chapter.

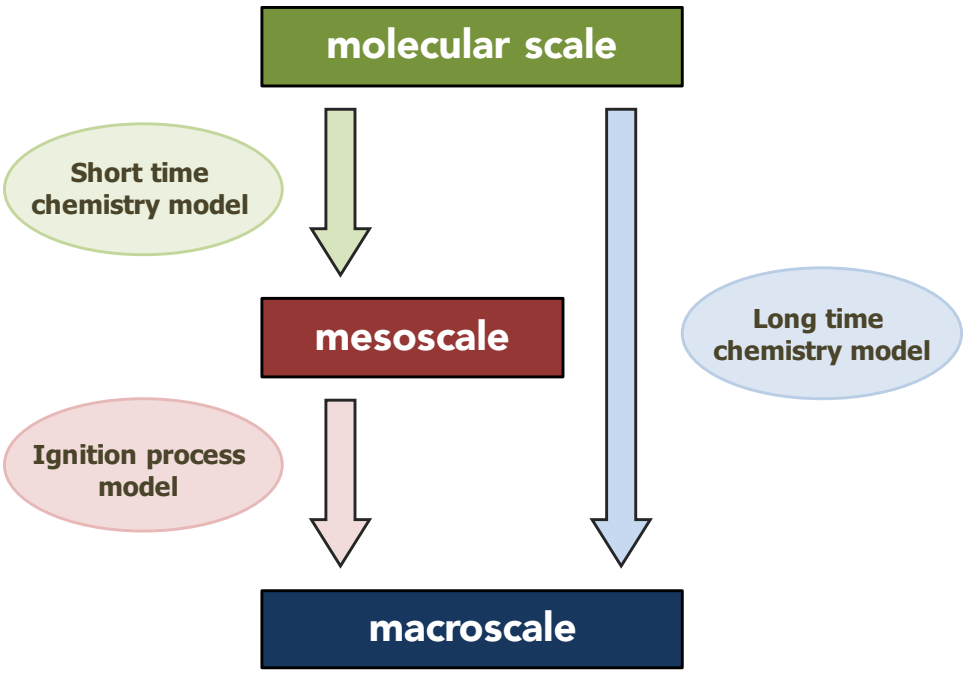

Figure 4.1: Asynchronous mutiscale integration strategy.

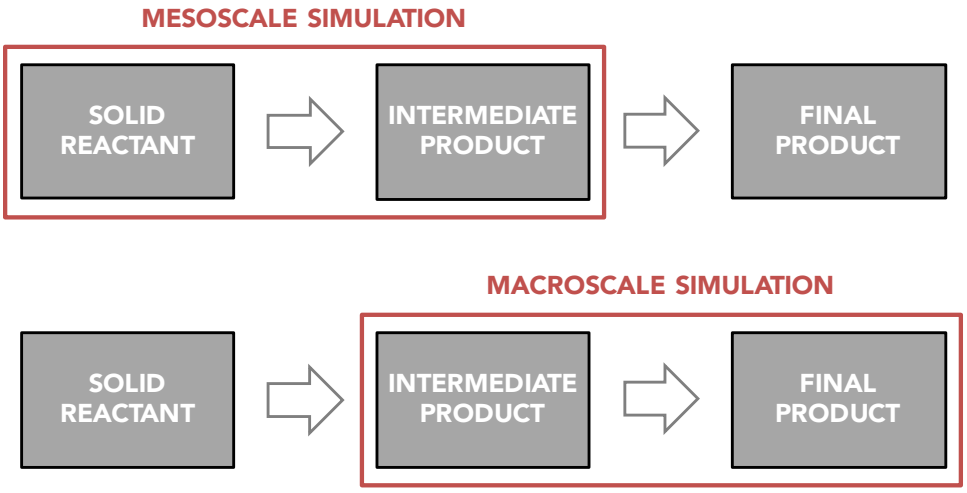

Figure 4.2: Functions of the short time chemistry model [6] (upper figure) and long time chemistry model [6] (lower figure).

Table 4.1: Comparison of the temporal and spacial scales for HMX and RDX.

Simulation	Scale	Time step	Final time	Cell length	Model length
HMX	Macro	0.343 ns	2 μs	31.25 μm	25 mm
	Meso	0.018 ps	0.35 ns	3.13 nm	2.5 μm
	Molecular	0.010 fs	150.462 ps	4.5 nm	4.5 nm
RDX	Macro	0.364 ns	2 μs	31.25 μm	25 mm
	Meso	0.019 ps	0.35 ns	3.13 nm	2.5 μm
	Molecular	0.010 fs	174.86 ps	2.4 nm	2.4 nm

Chapter 5

Validation of the Individual Scales

5.1 Introduction

A variety of numerical methods have been employed to develop multiscale models for materials design applications [34], in particular for energetic materials [60, 71]. In the case of energetic materials, multiscale modeling is most often aimed at relating mesoscale models of ignition mechanisms [2, 58, 61, 72] and molecular scale models of detonation chemistry [44, 86] to macroscale explosive performance [48, 84]. Methods which are systematic, applicable to a wide range of materials, and computationally efficient are needed to augment experimental research in the development of improved explosives and propellants.[3]

Recent research [5, 39] has developed the first unified Hamiltonian approach to multiscale modeling of reacting shock physics, applying discrete nonholonomic modeling techniques proven in previous research [64, 65] to address the energetic materials design problem. The cited works describe a three

[3]This chapter is based on the previous publication: Lee, S., and Fahrenthold, E.P., "Multiscale simulation of shock to detonation," presented at AIAA Propulsion and Energy Forum, July, Salt Lake City, UT, *AIAA 2016-4615*, 2016. The co-author is an expert in shock physics modeling at distinct scales, the dissertation author's expertise is in the integration of models developed at various scales.

scale formulation, including an Eulerian macroscale finite element model, a Lagrangian mesoscale hybrid particle-element model, and a new approach to reacting molecular dynamics. This chapter describes a series of simulations employed to validate the macoscale and mesoscale models, against experimental data on shock to detonation in nitroaromatic and nitramine explosives. In addition it develops a systematic approach to asynchronous [19] integration of the meso and macro scale models with detonation chemistry obtained from reacting molecular dynamics simulations.

5.2 Multiscale Formulation

In typical detonation simulation applications [5, 39], the multiscale formulation developed here would employ Eulerian and Lagrangian frames at the macro and meso scales respectively, although the finite element and hybrid-particle element methods used are scale agnostic. In this case the macroscale unit cell is an Eulerian finite element and the mesoscale model represents a unit cell of an Eulerian finite element. In the mesoscale model voids may be represented explicitly or implicitly. In the former case the void is simply an inter-particle gap; in the later case there are no initial-particle gaps, instead each particle is a mixture of a solid and a gas-filled void. Both the macroscale Eulerian finite element formulation and the mesoscale Lagrangian hybrid particle-element formulation may incorporate:

- large strain kinematics and general reacting-themomechanical coupling,

- plastic compaction of voids and mixed solid-gas thermodynamics, and
- nonuniform initial void distributions with general ignition and reaction kinetics models.

Unlike some alternative particle based methods, the mesoscale Lagrangian hybrid particle-element formulation can be effectively employed over a very wide range of velocities [64, 65], since it incorporates:

- true Lagrangian modeling of fracture and fragmentation, avoiding numerical fracture and tensile instability, and
- singular interpolations kernels, avoiding particle streaming; the method has been routinely applied to model shock impact problems at orbital debris impact velocities.

The molecular scale model consists of phase space evolution equations for the atoms, augmented by nonholonomic constraints. The later constraints are evolution equations for the bond states and molecular potential energies. The reacting molecular dynamics formulation incorporates [4–6]:

- general nonlinear effects, such as pressure or temperature dependent bond stiffnesses,
- an explicit description of the bond state, so that ambiguity in the reacted state of the system is avoided,

- a reduced model parameter count, since (as compared to holonomic formulations) smoothness requirements are greatly relaxed, and
- an energy conserving model of integer (step) changes in bond order.

Validation of the reacting molecular dynamics model has been performed in recent research [4]. The next section describes a series of simulations performed to validate the meso and macroscale components of the multiscale model.

5.3 Validation of the Component Models

The simulations discussed in this section evaluate the meso and macroscale models using a flyer plate impact test problem (Figure 5.1). The simulations model shock to detonation for flyer plate impacts at 5.6 km/s in TNT and at 7.0 km/s in Composition B. They employ: (1) Jones-Wilkins-Lee (JWL) equations of state for the solid reactant and gas product, and (2) an ignition and growth model for the explosive, both taken from the published literature [11, 85].

The JWL equations of state for the solid reactants and the gas products in both TNT [11] and Composition B [85] are defined as follows:

$$P = A\left(1-\frac{\omega}{R_1\mu}\right)e^{-R_1\mu} + B\left(1-\frac{\omega}{R_2\mu}\right)e^{-R_2\mu} + \omega\frac{(e+e_i)}{\mu} \quad (5.1)$$

$$\theta = \frac{1}{C_v}(e-e_o) \quad (5.2)$$

where

$$\mu = \frac{\rho_o}{\rho} \quad (5.3)$$

and the JWL coefficients A, B, R_1, R_2, ω, and e_i are listed in Tables 3.2 and 5.1. The following mixture relation interpolates between solid reactant and gas product.

$$P = (1 - F)P_{solid} + FP_{gas} \tag{5.4}$$

The ignition and growth model for TNT [11] is

$$\frac{dF}{dt} = \underbrace{I(1-F)^b \left(\frac{\rho}{\rho_o} - 1 - a\right)^x}_{0<F<F_{igmax}} + \underbrace{G_1(1-F)^c F^d P^y}_{0<F<F_{G_1max}} + \underbrace{G_2(1-F)^e F^g P^z}_{F_{G_2min}<F<1} \tag{5.5}$$

where F denotes a reaction progress variable and P denotes a pressure. All the coefficients are listed in Table 3.3. The ignition and growth model for Composition B [85] is

$$\frac{dF}{dt} = I(1-F)^b \left(\frac{\rho}{\rho_o} - 1\right)^x + G(1-F)^e F^g P^z \tag{5.6}$$

All the coefficients are listed in Table 5.2.

Simulation results are compared to published experimental data [7, 36] on the von Neumann spike pressure, the C-J pressure, the particle velocity, and the detonation velocity in these explosives. Table 5.3 lists the published experimental data. Figures 5.2 and 5.3 show the Lagrangian mesoscale hybrid particle-finite element simulation results, while Figures 5.4 and 5.5 show the Eulerian macroscale finite element simulation results. The plots show good agreement of the models with experiment for von Neumann spike pressure, C-J pressure, and particle velocity in the detonating explosives.

Figure 5.6 shows convergence of the mesoscale model simulations, comparing the predicted detonation velocities with the corresponding experimental detonation velocities, as a function of model resolution, for both TNT and Composition B. Accurate numerical results are obtained at the converged resolution.

Chapter 5 focused on the validation of models at individual scales. The succeeding chapters will address multiscale simulations, incorporating individual scale models of the type which have been validated in this chapter.

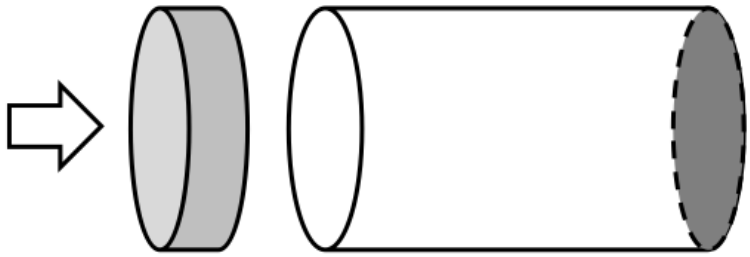

Figure 5.1: Flyer plate impact test problem.

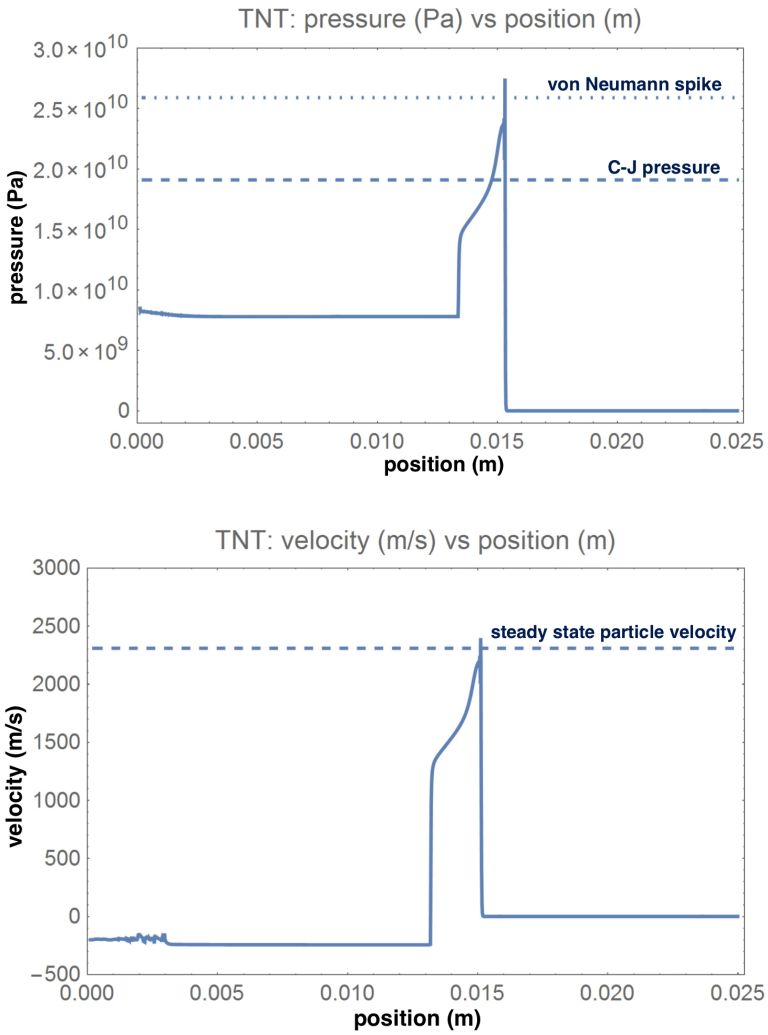

Figure 5.2: Mesoscale simulations: shock to detonation in TNT. The dotted line denotes von Neumann spike pressure (25 GPa) while the dashed lines denote CJ pressure (19 GPa) and velocity (2,310 m/s). The published experimental data are listed in Table 5.3

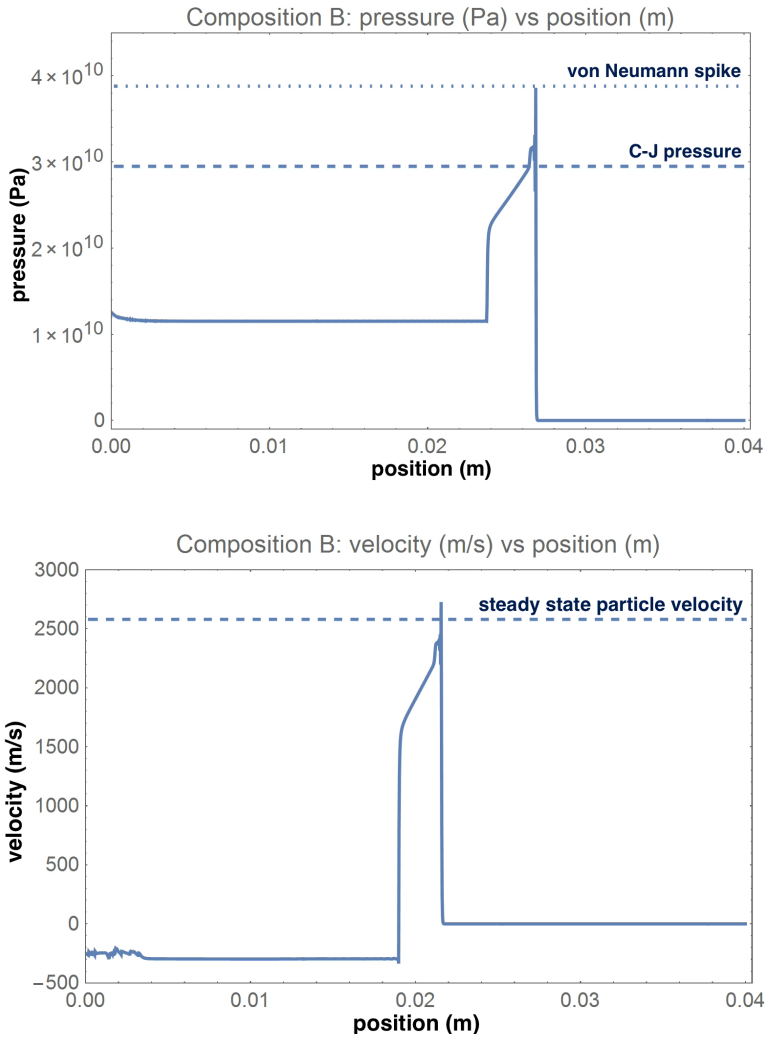

Figure 5.3: Mesoscale simulations: shock to detonation in Composition B. The dotted line denotes von Neumann spike pressure (38.8 GPa) while the dashed lines denote CJ pressure (30.1 GPa) and CJ velocity (2,590 m/s). The published experimental data are listed in Table 5.3

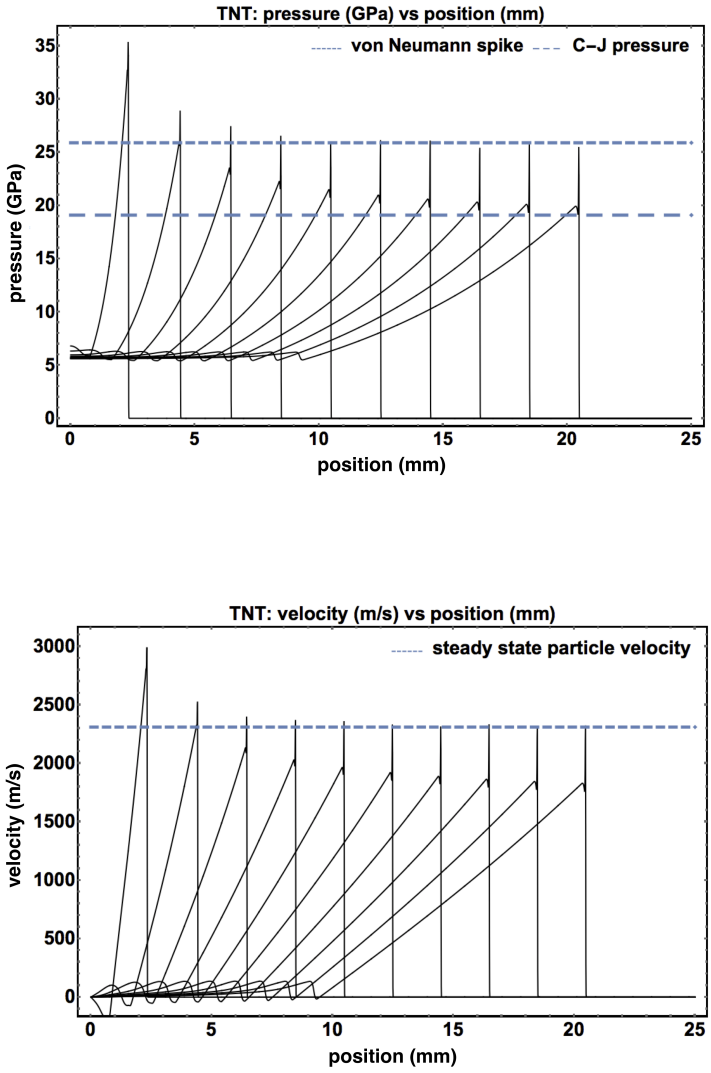

Figure 5.4: Macroscale simulations: shock to detonation in TNT. The dotted line denotes von Neumann spike pressure (25 GPa) while the dashed lines denote CJ pressure (19 GPa) and CJ velocity (2,310 m/s). The published experimental data are listed in Table 5.3

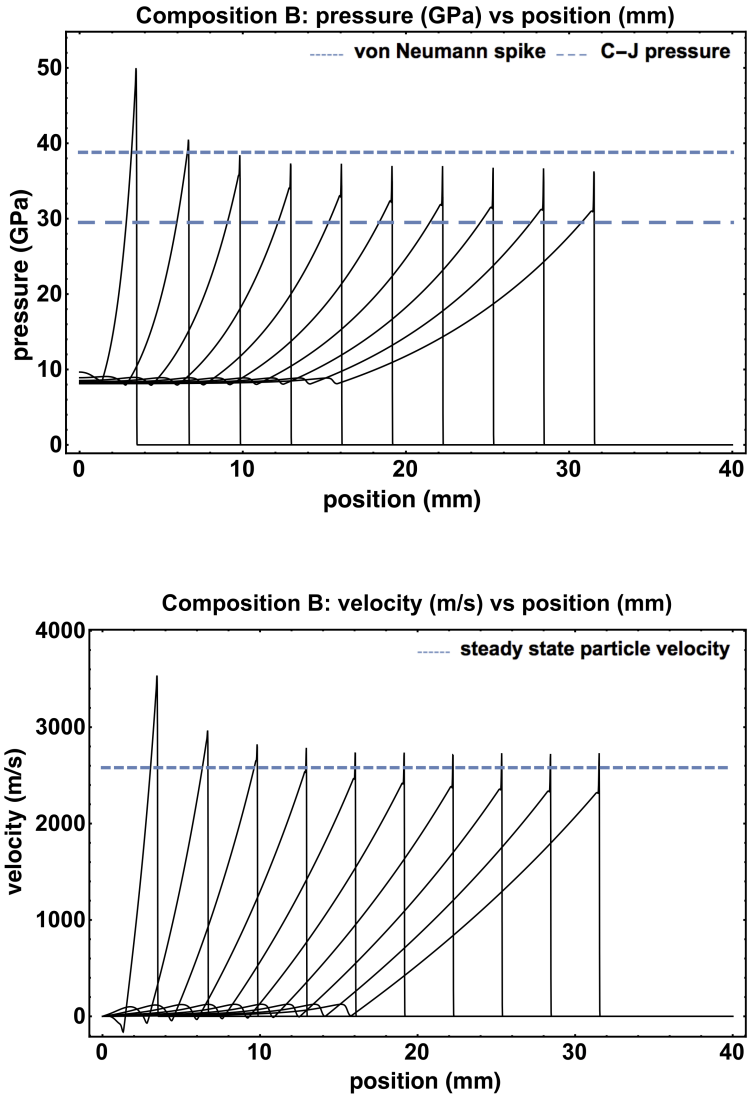

Figure 5.5: Macroscale simulations: shock to detonation in Composition B. The dotted line denotes von Neumann spike pressure (38.8 GPa) while the dashed lines denote CJ pressure and CJ velocity (2,590 m/s). The published experimental data are listed in Table 5.3

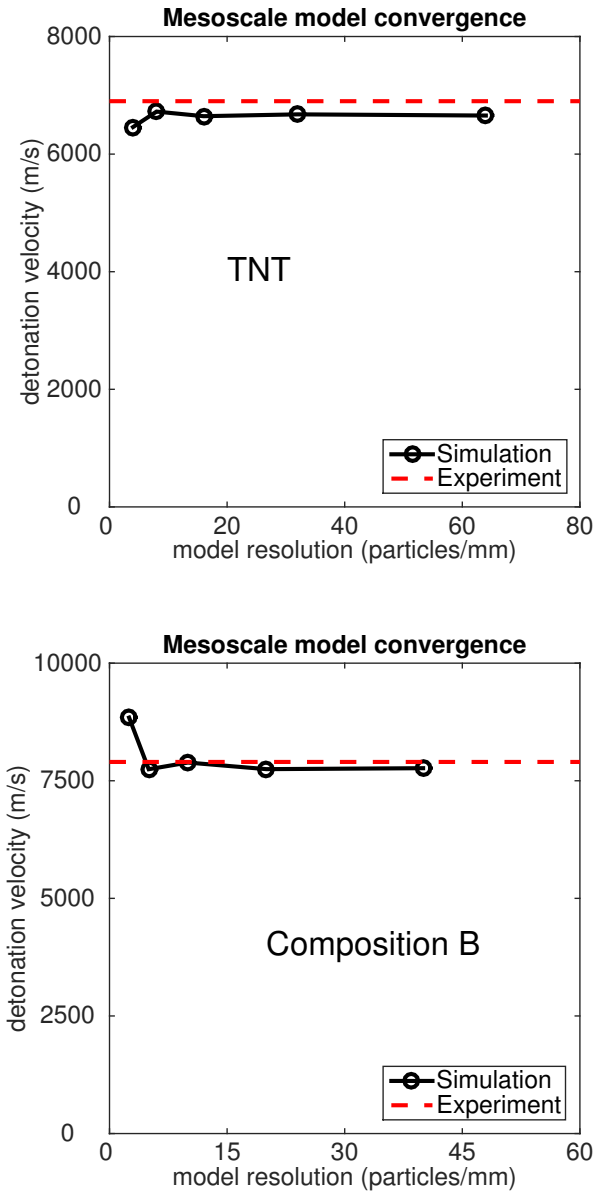

Figure 5.6: Mesoscale simulations: convergence test results for TNT (upper figure) and Composition B (lower figure).

Table 5.1: Equation of state parameters for Composition B: solid reactant and detonation gas products.

	Reactant	Product	Reference
A	77810 GPa	524.2 GPa	[85]
B	-5.03 GPa	7.678 GPa	[85]
R_1	11.3	4.2	[85]
R_2	1.13	1.1	[85]
ω	0.8938	0.34	[85]
C_v	2.487×10^{-3} GPa/K	1×10^{-3} GPa/K	[79]
ρ_o	1712 kg/m^3	1712 kg/m^3	[85]
e_i	0.6118 GPa/m^3	8.5 GPa/m^3	[85]

Table 5.2: Ignition and growth model parameters for Composition B [85].

I	$44.6 \times 10^6\ s^{-1}$
b	2/9
x	4.0
G	$414.0 \times 10^6\ Mbar^{-2}s^{-1}$
e	2/9
g	2/3
z	2.0
ρ_o	$1712\ kg/m^3$

Table 5.3: Published experimental data for TNT and Composition B.

Parameter	TNT	Reference	Composition B	Reference
CJ pressure (P_{CJ})	19 GPa	[11, 36]	27.2 GPa	[7]
			33 GPa	[85]
			30.1 GPa	average
VN pressure (P_{VN})	25 GPa	[11, 36]	38.8 GPa	[7]
VN velocity (v_{VN})	2310 m/s	[11, 36]	2590 m/s	[7, 85]
Detonation velocity (v_D)	6849 m/s	[36]	8220 m/s	[85]

Chapter 6

Validation of the Integrated Models: HMX

Chapters 6 and 7 validate the multiscale model of condensed phase explosives by extending the previously presented methodology. Each chapter includes both mesoscale and macroscale simulations. A description of the individual scale formulations is provided here but is not repeated in the next chapter.

6.1 Mesoscale Simulation

The mesoscale simulation of HMX models the integration of a short time chemistry model with a mesoscale hotspot generation model, the latter of great research interest [2, 46, 53]. The mesoscale formulation is first outlined, based on an extension of previous work. The short time chemical kinetics model, obtained from recent reacting MD simulation results, and the equations of state relation are then presented to complete the formulation. The simulation results provide an ignition process model to be applied in the macroscale simulation described in the next section.

6.1.1 Mesoscale Formulation

The mesoscale formulation described here extends previous work [31] by focusing on a reacting multiscale application. The system is modeled with a Lagrangian hybrid particle-element array, using discrete Hamilton's equations. The system model components describing plasticity and damage are obtained from previous development work [31]. In order to avoid reiteration of previously developed results, this section briefly describes the extended characteristics of the model.

1. The mesoscale formulation in this dissertation is the first to employ chemistry models and reaction dynamics in a hybrid particle-element discretization. Previous hybrid particle-element formulations focused solely on non-reacting, macroscale simulations in applications such as hypervelocity impacts [15], fabric perforation [64], and ordnance velocity impacts [31]. Introducing a chemical kinetics model requires additional state variables: species concentrations, $C_k^{(i)}$.

2. In addition to previous nonholonomic constrains for internal energies $U^{(i)}$, plastic strains $\epsilon^{p(i)}$, and damage variables $d^{(i)}$, species concentration evolution equations $C_k^{(i)}$ are now introduced as new nonholonomic constraints.

$$\dot{C}_k^{(i)} = \dot{C}_k^{(i)} \left(C_j^{(i)}, \rho^{(i)}, e^{(i)} \right) \tag{6.1}$$

3. In addition to the previous canonical mesoscale Hamilton's equations,

additional equations are added here:

$$0 = -\frac{\partial H}{\partial C_k^{(i)}} + q^{C_k(i)} \tag{6.2}$$

where the generalized nonconservative forces $q^{c_k(i)}$ are determined from the nonholonomic constraints. Introducing Lagrange multipliers $\gamma^{C_k(i)}$ for the nonholonomic constraints, we obtain

$$q^{C_k(i)} = \gamma^{C_k(i)} \tag{6.3}$$

The degenerate Hamilton's equations for $C_k^{(i)}$ allow the constraint Lagrange multipliers to be determined in closed form:

$$\gamma^{C_k(i)} = 0 \tag{6.4}$$

The nonconservative generalized forces for species concentrates are therefore:

$$q^{C_k(i)} = 0 \tag{6.5}$$

Note that no new terms will appear in the final momentum balance equations.

4. The mesoscale formulation employs new equations of state which depend on reaction progress variables $\lambda^{mes(i)}$:

$$P^{(i)} = P^{(i)}\left(\rho^{(i)}, e^{(i)}, \lambda^{mes(i)}\right) \tag{6.6}$$

$$\theta^{(i)} = \theta^{(i)}\left(\rho^{(i)}, e^{(i)}, \lambda^{mes(i)}\right) \tag{6.7}$$

$$\lambda^{mes(i)} = \lambda^{mes(i)}\left(C_j^{(i)}\right) \tag{6.8}$$

Note that both a solid reactant EOS and a detonation products EOS are now needed to complete the global model

$$P^{(i)}_{solid} = P^{(i)}_{solid}\left(\rho^{(i)}, e^{(i)}\right) \qquad \theta^{(i)}_{solid} = \theta^{(i)}_{solid}\left(\rho^{(i)}, e^{(i)}\right) \tag{6.9}$$

$$P^{(i)}_{det} = P^{(i)}_{det}\left(\rho^{(i)}, e^{(i)}\right) \qquad \theta^{(i)}_{det} = \theta^{(i)}_{det}\left(\rho^{(i)}, e^{(i)}\right) \tag{6.10}$$

The specific EOS formulations and parameters used here are taken from the literature (Table 6.4, 6.5, 7.4, and 7.5)

6.1.2 Chemical Kinetics Model

The chemical kinetics models summarized were not developed in this dissertation, rather they are taken from separate research which has been conducted concurrently [4–6].

The simplified 4-step short time (detonation) chemistry model for $\beta-$HMX is as follows [4, 6]:

$$\begin{aligned}
C_4H_8N_8O_8 &\rightarrow 4NO_2 + 4CH_2 + 4N \qquad (6.11)\\
NO_2 + CH_2 &\rightarrow NOH + COH\\
4COH &\rightarrow 0.35CO_2 + 1.65CO + 4H + 1.65O + 2C\\
4NOH &\rightarrow 1.7N_2 + 0.6N + 0.15H_2O + 1.35OH + 2.5O + 2.35H
\end{aligned}$$

Note that the final products of this chemistry model are intermediate states, and are distinct from the final products of long time (recombination) chemistry model. In the detonation, the solid reactant is decomposed into 13 species of intermediate gas products. The short time chemistry model allows for time

dependent species concentration rates to be computed in the state space model which follows.

6.1.3 State Equations: Chemical Subsystem

The state equations for the species concentrations [4, 6] are

$$\begin{aligned}
C_4H_8N_8O_8: &\quad \tfrac{dC_1}{dt} &&= -r_1 \\
NO_2: &\quad \tfrac{dC_2}{dt} &&= 4r_1 - r_2 \\
CH_2: &\quad \tfrac{dC_3}{dt} &&= 4r_1 - r_2 \\
N_2: &\quad \tfrac{dC_4}{dt} &&= 1.7r_4 \\
NOH: &\quad \tfrac{dC_5}{dt} &&= r_2 - 4r_4 \\
COH: &\quad \tfrac{dC_6}{dt} &&= r_2 - 4r_3 \\
CO_2: &\quad \tfrac{dC_7}{dt} &&= 0.35r_3 \\
CO: &\quad \tfrac{dC_8}{dt} &&= 1.65r_3 \\
C: &\quad \tfrac{dC_9}{dt} &&= 2r_3 \\
H: &\quad \tfrac{dC_{10}}{dt} &&= 4r_3 + 2.35r_4 \\
O: &\quad \tfrac{dC_{11}}{dt} &&= 1.65r_3 + 2.5r_4 \\
N: &\quad \tfrac{dC_{12}}{dt} &&= 4r_1 + 0.6r_4 \\
H_2O: &\quad \tfrac{dC_{13}}{dt} &&= 0.15r_4 \\
OH: &\quad \tfrac{dC_{14}}{dt} &&= 1.35r_4
\end{aligned} \tag{6.12}$$

where the C_i are species concentrations and the r_j are reaction rates.

6.1.4 Rate Laws

The reaction rates [4, 6] are

$$\begin{aligned} r_1 &= k_1 C_1^{1.27} \left(\frac{\rho}{\rho_o}\right)^{1-m^{(j)}} u_s(\theta_{max}^{his} - \theta_{ign}) \\ r_2 &= k_2 C_2^{1.00} C_3^{1.00} \left(\frac{\rho}{\rho_o}\right)^{1-m^{(j)}} u_s(\theta_{max}^{his} - \theta_{ign}) \\ r_3 &= k_3 C_6^{1.41} \left(\frac{\rho}{\rho_o}\right)^{1-m^{(j)}} u_s(\theta_{max}^{his} - \theta_{ign}) \\ r_4 &= k_4 C_5^{1.23} \left(\frac{\rho}{\rho_o}\right)^{1-m^{(j)}} u_s(\theta_{max}^{his} - \theta_{ign}) \end{aligned} \tag{6.13}$$

where ρ and ρ_o are the particle density and the particle reference density, θ_{max}^{his} is the maximum historical temperature, θ_{ign} is the ignition temperature, and u_s denotes a unit step function. In the HMX validation example, $\theta_{ign} = 550$ K. The rate law constants k_j are shown in Table 6.1.

6.1.5 Equations of State

A reaction progress variable λ^{mes} is used to interpolate between the solid reactant pressure (P_{solid}) and the detonation gas products pressure P_{det}, so that the mesoscale particle pressure is

$$P_{meso} = (1 - \lambda^{mes})\, P_{solid} + \lambda^{mes}\, P_{det} \tag{6.14}$$

Similarly the mesoscale temperature is

$$\theta_{meso} = (1 - \lambda^{mes})\, \theta_{solid} + \lambda^{mes}\, \theta_{det} \tag{6.15}$$

The reaction progress variable is determined by the initial solid species concentration C^o_{solid} and the current solid species concentration C_{solid}

$$\lambda^{mes} = 1 - \frac{C_{solid}}{C^o_{solid}}, \qquad 0 \leq \lambda^{mes} \leq 1 \tag{6.16}$$

The solid equation of state takes a Mie-Grüneisen form [72]

$$P_{solid} = C_s^2 (\rho - \rho_o) + \gamma \rho_o (e - e_o) \tag{6.17}$$

$$\theta_{solid} = \frac{1}{C_v} (e - e_o) \tag{6.18}$$

where θ denotes a temperature, C_s denotes a sound speed, ρ denotes a density, γ denotes a Grüneisen coefficient, and e denotes an internal energy per unit mass. Note that ρ_o and e_o are reference density and reference internal energy respectively. The model parameters are listed in Table 6.4.

The detonation products are modeled using a Jones-Wilkins-Lee (JWL) equation of state [67, 84]

$$P_{det} = A \left(1 - \frac{\omega}{R_1 \mu}\right) e^{-R_1 \mu} + B \left(1 - \frac{\omega}{R_2 \mu}\right) e^{-R_2 \mu} + \omega \frac{(e + e_i)}{\mu} \tag{6.19}$$

$$\theta_{det} = \frac{1}{C_v} (e - e_o) \tag{6.20}$$

where

$$\mu = \frac{\rho_o}{\rho} \tag{6.21}$$

and the JWL coefficients A, B, R_1, R_2, ω, and e_i are shown in Table 6.5.

6.1.6 Simulation Results

The mesoscale validation simulation for HMX models a wall shock in a 2.5 μm long sample of HMX explosive, at an impact velocity of 500 m/s. The

voids are modeled explicitly, as shown in Figure 6.1. The simulation results are compared to published experimental data on the von Neumann spike state, the Chapman-Jouguet state, and the detonation speed in HMX, which are listed in Table 6.7. The computation employs a Runge-Kutta second order method to integrate the ordinary differential equations.

Note that 50% void regions are placed in the explosive, as indicated in Figure 6.2. Figure 6.3 shows the initial velocity distribution, where the magenta colored lines denote the void region.

The shock fronts propagate from the wall outward, in both directions. Figure 6.4 shows that the detonation waves are generated in each void region, propagating in both directions. The waves which propagate toward the wall collide, producing high pressure and temperature spikes. The outgoing waves propagate with prominent pressure peaks (similar results are shown in reference [52]), including both primary and secondary shocks. The simulation results for particle velocity show good agreement with published experimental data. The upper dashed lines denote steady state Von Neumann peaks (3510 m/s), while the lower dashed lines denote Chapman-Jouguet particle velocities (2316.7 m/s), which are listed in Table 6.7. Experimental averages are taken from all the listed test data. The predicted shock pressures also show good agreement with published experimental data. Figure 6.5 shows pressure profiles at 0.35 ns. As in the case of the particle velocity plots, the upper and lower dashed lines denote Chapman-Jouguet (40.2 GPa) and von Neumann peak (61.6 GPa) pressures respectively. Note that the experimental pressure

and velocity values used for validation represent peak values, not plateaus.

As expected for a wall shock, the reaction progress variable (λ) profile takes a step form, as shown in Figure 6.6. The species concentration for the solid reactant $C_4H_8N_8O_8$ goes to zero as the explosive is fully reacted (corresponding experimental data is not available for comparison). Figures 6.7, 6.8 show temperature and density profiles for the simulation. In this simulation the reaction zone spans five particles, and the energy conservation error is 0.224 percent.

Figure 6.16 shows convergence of the mesoscale simulation results, as a function of model resolution. The simulation results for the predicted detonation wave speed show both good convergence and good agreement with the corresponding experiment. The dashed red lines denote the published experimental data values [13].

6.1.7 Ignition Process Model

The mesoscale simulation results suggest a simple ignition progress model, for use in the macroscale simulation. In the mesoscale simulation, pressure P and reaction progress λ are computed for each particle at every time step. The profiles of reaction progress variables for detonated particles are plotted in Figure 6.17. A linearly fit ignition process rate ζ, as a function of pressure, is noted in the figure and is used in the macroscale simulation.

$$\frac{df}{dP} = \zeta(P) \tag{6.22}$$

In Figure 6.17, the linear slope ζ_o is:

$$\zeta_o = \frac{1}{17} GPa^{-1} \tag{6.23}$$

Note that the mesoscale reaction progress variable plotted in Figure 6.17 is denoted as f in the macroscale simulation section which follows.

6.2 Macroscale Simulation

The macroscale model of HMX detonation integrates a long time chemistry model and and ignition process model into the macroscale shock to detonation simulation, the desired end product of multiscale simulations in this class of problems [44, 58]. In this section the macroscale formulation is developed, building on previous work. The long time chemistry model is obtained from recent reacting MD simulation results and the ignition process model is obtained from the mesoscale simulation. Equations of state relations are developed to complete the formulation. Simulation results are compared to published experimental data to validate the method.

6.2.1 Macroscale Formulation

The macroscale model described here fundamentally extends previous work [17, 18, 29]. The system is modeled with a Eulerian finite element array, using discrete Hamilton's equations incorporating chemical kinetics for a reacting system. To preclude any reiteration of previous work, this section is focused on extensions of existing formulations.

6.2.1.1 Descretization and Constitutive Relations

The finite element interpolation [17] and the system level model [29] build on previous work, including the kinetic energy model of [18], which employs as quasi-velocities the fluid velocities at the finite element nodes.

The equations of state used express the pressure and temperature as

functions of the element masses $m^{(i)}$, internal energies $U^{(i)}$, ignition process variables $f^{(i)}$, macroscale reaction progress variables $\lambda^{mac(i)}$, and species concentrations $C^{(i,j)}$:

$$P^{(i)} = P^{(i)}\left(m^{(i)}, U^{(i)}, f^{(i)}, \lambda^{mac(i)}\right) \tag{6.24}$$

$$\theta^{(i)} = \theta^{(i)}\left(m^{(i)}, U^{(i)}, f^{(i)}, \lambda^{mac(i)}\right) \tag{6.25}$$

$$f^{(i)} = f^{(i)}\left(m^{(i)}, s^{(i,j)}\right) \tag{6.26}$$

$$\lambda^{mac(i)} = \lambda^{mac(i)}\left(C^{(i,j)}\right) \tag{6.27}$$

where $P^{(i)}$ are the mixture pressures and $\theta^{(i)}$ are the mixture temperatures.

The macroscale reaction progress variables $\lambda^{mac(i)}$ of Chapter 4 are here defined as

$$\lambda^{mac(i)} = \frac{\bar{C}^{(i)} - \bar{C}_0}{\bar{C}_1 - \bar{C}_0} \qquad 0 \leq \lambda^{mac(i)} \leq 1 \tag{6.28}$$

and

$$\bar{C}^{(i)} = \frac{s^{(i,j)}}{m^{(i)}} \frac{\mathbb{M}^{solid}}{\mathbb{M}^{(j)}} \tag{6.29}$$

where $\bar{C}^{(i)}$ are the selected species concentration ratios, $\bar{C}_0$ is an initial species concentration ratio, and $\bar{C}_1$ is a final concentration ratio (the units of these concentration ratios are moles per unit mole of solid reactant), $\mathbb{M}^{solid}$ is the molar mass of the solid, and $\mathbb{M}^{(j)}$ is the molar mass of species j. The selected species and reference values are provided in succeeding sections.

The reacted (detonated) masses $m_f^{(i)}$ are defined as

$$m_f^{(i)} = m^{(i)} f^{(i)} \tag{6.30}$$

and the reacted masses and species masses must satisfy

$$m_f^{(i)} = \sum_{j=1}^{N_s} s^{(i,j)} \tag{6.31}$$

where N_s is the total species count. Hence

$$\lambda^{mac(i)} = \lambda^{mac(i)} \left(m^{(i)}, s^{(i,j)} \right) \tag{6.32}$$

With the above equations, the equations of state have final functional forms

$$P^{(i)} = P^{(i)} \left(U^{(i)}, m^{(i)}, s^{(i,j)} \right) \tag{6.33}$$

$$\theta^{(i)} = \theta^{(i)} \left(U^{(i)}, m^{(i)}, s^{(i,j)} \right) \tag{6.34}$$

Note that a solid reactant EOS, a detonation product EOS, and a final product gas mixture EOS are needed to compute the element pressure and temperature.

6.2.1.2 Kinetic and Potential Energy

The macroscale Hamiltonian (with n_e finite elements and n_n nodes) is the sum of the kinetic energy T and the potential energy V

$$H = T + V = \frac{1}{2}\, \mathbf{p}^T \mathbf{M}^{-1} \mathbf{p} + \sum_{i=1}^{n_e} U^{(i)}, \qquad \mathbf{p} = \mathbf{M}\mathbf{v} \tag{6.35}$$

where $\mathbf{M}$ is the mass matrix, the element internal energies $U^{(i)}$ are state variables, $\mathbf{p}$ is the momentum vector, and $\mathbf{v}$ is the n_n dimensional vector of nodal velocities. Previous work has provided detailed developments [18].

To obtain a system level model, the macroscale Hamiltonian is combined with the canonical Hamilton's equations, a virtual work expression, and

nonholonomic constraints describing the evolution of the element masses $m^{(i)}$, the element internal energies $U^{(i)}$, the detonated masses $m_f^{(i)}$, and the element species masses $s^{(i,j)}$.

6.2.1.3 Conservation of Mass and Internal Energy Evolution

The mass conservation equations for the system and the evolution equation for the internal energy are taken from previous work [17, 29]. The mass conservation relations are

$$\dot{\mathbf{m}} = \mathbf{A}\mathbf{M}^{-1}\mathbf{p}, \qquad \mathbf{A} = \mathbf{A}(\mathbf{m}) \tag{6.36}$$

where $\mathbf{A}$ is the coefficient matrix which depends on the element masses [17].

The internal energy evolution equations depend on convection across element boundaries $\dot{\mathbf{U}}^{cvc}$, a mechanical power flow $\dot{\mathbf{U}}^{wrk}$, a dissipated power $\dot{\mathbf{U}}^{irr}$, and a heat conduction power flow $\dot{\mathbf{U}}^{con}$ [17]

$$\dot{\mathbf{U}} = \dot{\mathbf{U}}^{cvc} + \dot{\mathbf{U}}^{wrk} + \dot{\mathbf{U}}^{irr} - \dot{\mathbf{U}}^{con} \tag{6.37}$$

The convection term is [17]

$$\dot{\mathbf{U}}^{cvc} = \mathbf{R}\mathbf{M}^{-1}\mathbf{p}, \qquad \mathbf{R} = \mathbf{R}(\mathbf{m}, \mathbf{U}) \tag{6.38}$$

where $\mathbf{R}$ is a coefficient matrix which depends on the element masses and the element internal energies. The flow work term is [29]

$$\dot{\mathbf{U}}^{wrk} = \mathbf{G}\mathbf{M}^{-1}\mathbf{p}, \qquad \mathbf{G} = \mathbf{G}(\mathbf{m}, \mathbf{U}, \mathbf{s}) \tag{6.39}$$

where $\mathbf{G}$ is a coefficient matrix which depends on the thermodynamic pressures. The irreversible term is [29]

$$\dot{\mathbf{U}}^{irr} = \mathbf{C}\mathbf{M}^{-1}\mathbf{p}, \qquad \mathbf{C} = \mathbf{C}(\mathbf{m}, \mathbf{U}) \tag{6.40}$$

where $\mathbf{C}$ is a coefficient matrix which depends on the element densities and internal energies. The conduction term is [29]

$$\dot{\mathbf{U}}^{con} = \boldsymbol{\kappa}, \qquad \boldsymbol{\kappa} = \boldsymbol{\kappa}(\mathbf{m}, \mathbf{U}, \mathbf{s}) \tag{6.41}$$

where $\boldsymbol{\kappa}$ is a vector which depends on the element temperatures. For the system, the complete internal energy evolution equations are

$$\dot{\mathbf{U}} = (\mathbf{R} + \mathbf{G} + \mathbf{C})\mathbf{M}^{-1}\mathbf{p} - \boldsymbol{\kappa} \tag{6.42}$$

6.2.1.4 Ignition Process Model

In addition to nonholonomic constraints for the internal energy $U^{(i)}$ and element mass $m^{(i)}$ evolution, evolution equations are needed for the detonated masses $m_f^{(i)}$. They depends on an ignition process variable $f^{(i)}$ and the species masses $s^{(i,j)}$ and are new to this formulation.

The reacted (detonated) masses $m_f^{(i)}$ are defined as

$$m_f^{(i)} = m^{(i)} f^{(i)} \tag{6.43}$$

Evolution of the reacted masses depends on convection of the internal state variable $\dot{m}_f^{cvc(i)}$ as well as an ignition source term $\dot{m}_f^{src(i)}$

$$\dot{m}_f^{(i)} = \dot{m}_f^{cvc(i)} + \dot{m}_f^{src(i)} \tag{6.44}$$

The convected term is

$$\dot{m}_f^{cvc(i)} = -\int_{S^{(i)}} \hat{\rho}\frac{\hat{m}_f}{\hat{m}}\hat{\mathbf{v}}\cdot\hat{\mathbf{n}}dS \tag{6.45}$$

where $\hat{\rho}$ is an interface density, $\hat{m}_f$ is an interface reacted mass, $\hat{m}$ is an interface mass, and $\hat{\mathbf{v}}$ is an interface material velocity across an element surface $S^{(i)}$ with unit normal vector $\hat{\mathbf{n}}$. In discrete form

$$\dot{m}_f^{cvc(i)} = \sum_{j=1}^{n_S} \rho^{(i,j)}\frac{m_f^{(i,j)}}{m^{(i,j)}}\mathbf{a}^{(i,j)T}(\mathbf{M^{-1}p}) \tag{6.46}$$

where $\rho^{(i,j)}$ is the upwind density at the j^{th} surface of the i^{th} element, $m_f^{(i,j)}$ is the upwind reacted mass, $m^{(i,j)}$ is the upwind element mass, and $\mathbf{a}^{(i,j)T}$ is a constant vector which depends on the nodal coordinates.

The source terms are

$$\dot{m}_f^{src(i)} = max(0, m^{(i)} - m_f^{(i)})max\left[\frac{v_D}{L^{(i)}}, \zeta_o max\left(0, \frac{dP^{(i)}}{dt}\right)\right] u_s(P^{(i)} - P_{ign}) \tag{6.47}$$

where v_D is the detonation velocity, $L^{(i)}$ is an element characteristic length, ζ_o is obtained from the mesoscale simulation results, and u_s denotes a unit step function. The formulation employs a pressure dependent ignition criterion. The source terms have the general functional forms $D^{(i)}$

$$\dot{m}_f^{src(i)} = D^{(i)}(P^{(i)}, m^{(i)}, m_f^{(i)})\dot{P}^{(i)} \tag{6.48}$$

At the system level, the reacted mass evolution equations are

$$\dot{\mathbf{m}}_f = \mathbf{XM^{-1}p} + \mathbf{D}\dot{\mathbf{P}} \tag{6.49}$$

where the coefficient matrices depend on the element masses and the reacted masses

$$\mathbf{X} = \mathbf{X}(\mathbf{m}, \mathbf{m}_f), \qquad \mathbf{D} = \mathbf{D}(\mathbf{P}, \mathbf{m}, \mathbf{m}_f) \tag{6.50}$$

6.2.1.5 Species Mass Evolution Equations

The species mass evolution equations depend on convection of the species masses $\dot{s}^{cvc(i,j)}$, as defined in previous work [29], as well as reaction source terms.

Since the reaction source terms employ the results of reacting MD simulation, a homologous temperature variable $\theta_H^{(i)}$ is introduced to map molecular scale to macroscale temperatures, which may vary over distinct ranges:

$$\theta_H^{(i)} = \frac{\theta_1 - \theta^{(i)}}{\theta_1 - \theta_0}, \qquad 0 \leq \theta_H^{(i)} \leq 1 \tag{6.51}$$

where θ_0, θ_1 are minimum and maximum temperatures associated with the detonation energy release calculation.

$$\Delta E = C_v(\theta_1 - \theta_o) \tag{6.52}$$

Here ΔE denotes an energy release (heat of detonation) and C_v denotes the specific heat of a detonation gas

$$\theta_1 = \theta_o + \frac{\Delta E}{C_v} \tag{6.53}$$

Specific values are computed in succeeding sections.

The species mass conservation equations are

$$\dot{s}^{(i,j)} = \dot{s}^{cvc(i,j)} + \bar{Y}_o^{(j)} \dot{m}_f^{src(i)} - \nu^{(i)} \mathbb{M}^{(j)} \frac{dC}{d\theta_H}^{(i,j)} \frac{1}{\theta_1 - \theta_o} min\left(0, \frac{d\theta}{dt}^{(i)}\right) \tag{6.54}$$

where the $\nu^{(i)}$ are the element volumes, $\mathbb{M}^{(j)}$ is the molar mass of j^{th} species, the partial derivatives $\frac{dC}{d\theta_H}^{(i,j)}$ are defined by the reacting MD simulations, and $\bar{Y}_o^{(i,j)}$ are the reference species mass fractions at the end of the short time (detonation) simulation.

$$\bar{Y}_o^{(i,j)} = \frac{\mathbb{M}^{(j)}}{\mathbb{M}^{solid}} \bar{C}_o^{(j)} \tag{6.55}$$

Here $\mathbb{M}^{solid}$ is the molar mass of the solid reactant and the $\bar{C}_o^{(j)}$ are the initial species concentration ratios listed in Tables 6.3 (HMX) and 7.3 (RDX). Using the relation $\dot{m}_f^{src(i)} = D^{(i)} \dot{P}^{(i)}$, the reaction source terms are expressed in the general functional form

$$\dot{s}^{(i,j)} = \dot{s}^{cvc(i,j)} + W^{(i)}(P^{(i)}, m^{(i)}, m_f^{(i)}) \dot{P}^{(i)} + E^{(i)} \left(m^{(i)}, s^{(i,j)}, P^{(i)} \right) \dot{\theta}^{(i)} \tag{6.56}$$

At the global level, the species mass evolution equations are

$$\dot{\mathbf{s}} = \mathbf{Z}\mathbf{M}^{-\mathbf{1}}\mathbf{p} + \mathbf{W}\dot{\mathbf{P}} + \mathbf{E}\dot{\boldsymbol{\theta}} \tag{6.57}$$

where $\mathbf{Z}$ is a convection coefficient matrix (defined in previous work [29]), the coefficient matrix $\mathbf{W}$ depends on the reacted masses and the species masses, and the coefficient matrix $\mathbf{E}$ depends on the reaction source terms obtained from reacting MD simulations

$$\mathbf{Z} = \mathbf{Z}(\boldsymbol{\rho}, \mathbf{s}), \qquad \mathbf{W} = \mathbf{W}(\mathbf{P}, \mathbf{m}, \mathbf{m}_f), \qquad \mathbf{E} = \mathbf{E}(\mathbf{m}, \mathbf{s}, \mathbf{P}) \tag{6.58}$$

The next section will develop evolution equations for $\dot{\mathbf{P}}$ and $\dot{\boldsymbol{\theta}}$, required to finalize the constraint equations Eq.(6.49, 6.57).

6.2.1.6 Nonholomomic Constraints

Although the simulations employ a backward difference approximation to implement the overall model

$$\left.\frac{dP^{(i)}}{dt}\right|_{t_2} = \frac{P_2^{(i)} - P_1^{(i)}}{t_2 - t_1} \qquad \left.\frac{d\theta^{(i)}}{dt}\right|_{t_2} = \frac{\theta_2^{(i)} - \theta_1^{(i)}}{t_2 - t_1} \tag{6.59}$$

exact expressions for $\dot{\mathbf{P}}$ and $\dot{\boldsymbol{\theta}}$ are derived in the following paragraphs.

The thermodynamics pressures and temperatures are from Eq.(6.33 - 6.34)

$$\mathbf{P} = \mathbf{P}\left(\mathbf{U}, \mathbf{m}, \mathbf{s}\right), \qquad \boldsymbol{\theta} = \boldsymbol{\theta}\left(\mathbf{U}, \mathbf{m}, \mathbf{s}\right) \tag{6.60}$$

so that the pressure and temperature evolution equations are

$$\dot{\mathbf{P}} = \frac{d\mathbf{P}}{d\mathbf{U}}^T \dot{\mathbf{U}} + \frac{d\mathbf{P}}{d\mathbf{m}}^T \dot{\mathbf{m}} + \frac{d\mathbf{P}}{d\mathbf{s}}^T \dot{\mathbf{s}} \tag{6.61}$$

$$\dot{\boldsymbol{\theta}} = \frac{d\boldsymbol{\theta}}{d\mathbf{U}}^T \dot{\mathbf{U}} + \frac{d\boldsymbol{\theta}}{d\mathbf{m}}^T \dot{\mathbf{m}} + \frac{d\boldsymbol{\theta}}{d\mathbf{s}}^T \dot{\mathbf{s}} \tag{6.62}$$

Substituting the above equations into Eq.(6.57), the species mass evolution relation is

$$\begin{aligned} \dot{\mathbf{s}} = {} & \mathbf{Z}\mathbf{M}^{-1}\mathbf{p} + \mathbf{W}\left(\frac{d\mathbf{P}}{d\mathbf{U}}^T \dot{\mathbf{U}} + \frac{d\mathbf{P}}{d\mathbf{m}}^T \dot{\mathbf{m}} + \frac{d\mathbf{P}}{d\mathbf{s}}^T \dot{\mathbf{s}}\right) \\ & + \mathbf{E}\left(\frac{d\boldsymbol{\theta}}{d\mathbf{U}}^T \dot{\mathbf{U}} + \frac{d\boldsymbol{\theta}}{d\mathbf{m}}^T \dot{\mathbf{m}} + \frac{d\boldsymbol{\theta}}{d\mathbf{s}}^T \dot{\mathbf{s}}\right) \end{aligned} \tag{6.63}$$

Substituting $\dot{\mathbf{U}}$ from Eq.(6.42) and $\dot{\mathbf{m}}$ from Eq.(6.36), and rearranging,

$$\begin{aligned} \left(I - \mathbf{W}\frac{d\mathbf{P}}{d\mathbf{s}}^T - \mathbf{E}\frac{d\boldsymbol{\theta}}{d\mathbf{s}}^T\right)\dot{\mathbf{s}} = {} & \left[\mathbf{Z} + \left(\mathbf{W}\frac{d\mathbf{P}}{d\mathbf{U}}^T + \mathbf{E}\frac{d\boldsymbol{\theta}}{d\mathbf{U}}^T\right)(\mathbf{R} + \mathbf{G} + \mathbf{C})\right. \\ & \left. + \left(\mathbf{W}\frac{d\mathbf{P}}{d\mathbf{m}}^T + \mathbf{E}\frac{d\boldsymbol{\theta}}{d\mathbf{m}}^T\right)\mathbf{A}\right]\mathbf{M}^{-1}\mathbf{p} - \left(\mathbf{W}\frac{d\mathbf{P}}{d\mathbf{U}}^T + \mathbf{E}\frac{d\boldsymbol{\theta}}{d\mathbf{U}}^T\right)\boldsymbol{\kappa} \end{aligned} \tag{6.64}$$

This has the essential form

$$\mathbf{Y}\dot{\mathbf{s}} = \mathbf{B}\mathbf{M}^{-1}\mathbf{p} + \boldsymbol{\phi} \tag{6.65}$$

$$\dot{\mathbf{s}} = \mathbf{Y}^{-1}\mathbf{B}\mathbf{M}^{-1}\mathbf{p} + \mathbf{Y}^{-1}\boldsymbol{\phi} \tag{6.66}$$

so that the final evolution equation for the species masses is

$$\dot{\mathbf{s}} = \mathbf{N}\mathbf{M}^{-1}\mathbf{p} + \boldsymbol{\chi} \tag{6.67}$$

where the coefficient matrix and the right hand side vector are $\mathbf{N} = \mathbf{Y}^{-1}\mathbf{B}$ and $\boldsymbol{\chi} = \mathbf{Y}^{-1}\boldsymbol{\phi}$.

Similarly, the evolution relation for the reacted mass is, from Eq.(6.49, 6.61, 6.67),

$$\begin{aligned}\dot{\mathbf{m}}_f &= \left[\mathbf{X} + \mathbf{D}\frac{d\mathbf{P}}{d\mathbf{U}}^T(\mathbf{R}+\mathbf{G}+\mathbf{C}) + \mathbf{D}\frac{d\mathbf{P}}{d\mathbf{m}}^T\mathbf{A}\right. \\ &\quad \left. + \mathbf{D}\frac{d\mathbf{P}}{d\mathbf{s}}^T\mathbf{N}\right]\mathbf{M}^{-1}\mathbf{p} + \mathbf{D}\left(-\frac{d\mathbf{P}}{d\mathbf{U}}^T\boldsymbol{\kappa} + \frac{d\mathbf{P}}{d\mathbf{s}}^T\boldsymbol{\chi}\right)\end{aligned} \tag{6.68}$$

This has the essential form

$$\dot{\mathbf{m}}_f = \mathbf{Q}\mathbf{M}^{-1}\mathbf{p} + \boldsymbol{\eta} \tag{6.69}$$

In summary, the macroscale nonholonomic constraints are as follows:

$$\dot{\mathbf{U}} = (\mathbf{R}+\mathbf{G}+\mathbf{C})\mathbf{M}^{-1}\mathbf{p} - \boldsymbol{\kappa} \tag{6.70}$$

$$\dot{\mathbf{m}} = \mathbf{A}\mathbf{M}^{-1}\mathbf{p} \tag{6.71}$$

$$\dot{\mathbf{m}}_f = \mathbf{Q}\mathbf{M}^{-1}\mathbf{p} + \boldsymbol{\eta} \tag{6.72}$$

$$\dot{\mathbf{s}} = \mathbf{N}\mathbf{M}^{-1}\mathbf{p} + \boldsymbol{\chi} \tag{6.73}$$

6.2.1.7 Virtual Work and Hamilton's Equations

The virtual work, expressed in terms of the quasivelocities $\dot{\mathbf{q}}$ [24], balances the rate of change of kinetic energy in the elements and at the nodes [18] using

$$\delta W = \left(\dot{\mathbf{M}}\mathbf{v}\right)^T \delta\mathbf{q} - 2\mathbf{k}^T\delta\mathbf{m}, \quad \dot{\mathbf{q}} = \mathbf{v} \tag{6.74}$$

where $\mathbf{k}$ denotes the kinetic energy per unit mass [18]

$$\mathbf{k} = -\frac{\partial H}{\partial \mathbf{m}} \tag{6.75}$$

The canonical macroscale Hamilton's equations are

$$\dot{\mathbf{p}} = \mathbf{q}^c \tag{6.76}$$

$$\mathbf{0} = -\frac{\partial H}{\partial \mathbf{U}} + \mathbf{q}^U \tag{6.77}$$

$$\mathbf{0} = -\frac{\partial H}{\partial \mathbf{m}} + \mathbf{q}^m \tag{6.78}$$

$$\mathbf{0} = -\frac{\partial H}{\partial \mathbf{m_f}} + \mathbf{q}^{m_f} \tag{6.79}$$

$$\mathbf{0} = -\frac{\partial H}{\partial \mathbf{s}} + \mathbf{q}^s \tag{6.80}$$

where $\mathbf{q}^c, \mathbf{q}^U, \mathbf{q}^m, \mathbf{q}^{m_f}$, and $\mathbf{q}^s$ are generalized nonconservative forces determined by the virtual work and the nonholonomic constraints. Introducing Lagrange multipliers $\boldsymbol{\gamma}^U$, $\boldsymbol{\gamma}^m$, $\boldsymbol{\gamma}^{m_f}$, and $\boldsymbol{\gamma}^s$ for the nonholonomic constraints,

$$(\boldsymbol{\gamma}^U)^T \left(\dot{\mathbf{U}} - (\mathbf{R} + \mathbf{G} + \mathbf{C})\mathbf{M}^{-1}\mathbf{p} + \boldsymbol{\kappa}\right) = \mathbf{0} \tag{6.81}$$

$$(\boldsymbol{\gamma}^m)^T \left(\dot{\mathbf{m}} - \mathbf{A}\mathbf{M}^{-1}\mathbf{p}\right) = \mathbf{0} \tag{6.82}$$

$$(\boldsymbol{\gamma}^{m_f})^T \left(\dot{\mathbf{m}}_f - \mathbf{Q}\mathbf{M}^{-1}\mathbf{p} - \boldsymbol{\eta}\right) = \mathbf{0} \tag{6.83}$$

$$(\boldsymbol{\gamma}^s)^T \left(\dot{\mathbf{s}} - \mathbf{N}\mathbf{M}^{-1}\mathbf{p} - \boldsymbol{\chi}\right) = \mathbf{0} \tag{6.84}$$

the generalized forces are obtained as

$$\mathbf{q}^U = \boldsymbol{\gamma}^U, \qquad \mathbf{q}^m = \boldsymbol{\gamma}^m - 2\mathbf{k}, \qquad \mathbf{q}^{m_f} = \boldsymbol{\gamma}^{m_f}, \qquad \mathbf{q}^s = \boldsymbol{\gamma}^s \tag{6.85}$$

$$\mathbf{q}^c = \dot{\mathbf{M}}\mathbf{v} - (\mathbf{R} + \mathbf{G} + \mathbf{C})^T\boldsymbol{\gamma}^U - \mathbf{A}^T\boldsymbol{\gamma}^m - \mathbf{Q}^T\boldsymbol{\gamma}^{m_f} - \mathbf{N}^T\boldsymbol{\gamma}^s \tag{6.86}$$

The degenerate Hamilton's equations for $\mathbf{U}$, $\mathbf{m}$, $\mathbf{m_f}$, and $\mathbf{s}$ allow the constraint Lagrange multipliers to be determined, in closed form, as

$$\boldsymbol{\gamma}^U = \mathbf{1}, \qquad \boldsymbol{\gamma}^m = \mathbf{k}, \qquad \boldsymbol{\gamma}^{m_f} = \mathbf{0}, \qquad \boldsymbol{\gamma}^s = \mathbf{0} \tag{6.87}$$

Since the momentum convection terms satisfy the relations [18]

$$\dot{\mathbf{M}}\mathbf{v} = \mathbf{F}\dot{\mathbf{m}}, \qquad 2\mathbf{k} = \mathbf{F}^T\mathbf{v} \tag{6.88}$$

and the algebraic sum of the internal energy convection terms is zero [17]

$$\mathbf{R}^T\mathbf{1} = \mathbf{0} \tag{6.89}$$

the final momentum balance equation is

$$\dot{\mathbf{p}} = \mathbf{FAM}^{-1}\mathbf{p} - (\mathbf{G} + \mathbf{C})^T\mathbf{1} - \mathbf{A}^T\mathbf{k} \tag{6.90}$$

This completes the macroscale formulation.

6.2.2 Chemical Kinetics Model

The 9-step long time chemistry model used to represent recombination in $\beta-$HMX is [6]:

$$\begin{aligned} C + O &\rightarrow CO \\ CO + O &\rightarrow CO_2 \\ OH + H &\rightarrow H_2O \\ N + N &\rightarrow N_2 \\ O + H &\rightarrow OH \\ N + 3H &\rightarrow NH_3 \\ C + C &\rightarrow C_2 \\ H + H &\rightarrow H_2 \\ H_2 + O &\rightarrow H_2O \end{aligned} \tag{6.91}$$

To address important time step issues, temperature is taken as the independent variable in modeling these recombination reactions, specifically the homologous temperature $\theta_H^{(i)}$ previously defined in Section 6.2.1.5. The macroscale HMX simulation employs $C_v = 1422\ J/kg\cdot K$ [67], and $\Delta E = 1479$ cal/J [55]. Assuming $\theta_0 = 0\ K$ in Eq.(6.53), $\theta_1 = 4351.7\ K$.

6.2.3 State Equations: Chemical Subsystem

In the macroscale model, the evolution equations for species j in element i are taken [6], for HMX, to be

$$\begin{aligned}
C: \quad & \frac{dC}{d\theta_H}^{(i,1)} &= & -R_1^{(i)} - 2R_7^{(i)} \\
O: \quad & \frac{dC}{d\theta_H}^{(i,2)} &= & -R_1^{(i)} - R_2^{(i)} - R_5^{(i)} - R_9^{(i)} \\
CO: \quad & \frac{dC}{d\theta_H}^{(i,3)} &= & R_1^{(i)} - R_2^{(i)} \\
CO_2: \quad & \frac{dC}{d\theta_H}^{(i,4)} &= & R_2^{(i)} \\
OH: \quad & \frac{dC}{d\theta_H}^{(i,5)} &= & -R_3^{(i)} + R_5^{(i)} \\
H: \quad & \frac{dC}{d\theta_H}^{(i,6)} &= & -R_3^{(i)} - R_5^{(i)} - 3R_6^{(i)} - 2R_8^{(i)} \\
H_2O: \quad & \frac{dC}{d\theta_H}^{(i,7)} &= & R_3^{(i)} + R_9^{(i)} \\
N: \quad & \frac{dC}{d\theta_H}^{(i,8)} &= & -2R_4^{(i)} - R_6^{(i)} \\
N_2: \quad & \frac{dC}{d\theta_H}^{(i,9)} &= & R_4^{(i)} \\
NH_3: \quad & \frac{dC}{d\theta_H}^{(i,10)} &= & R_6^{(i)} \\
C_2: \quad & \frac{dC}{d\theta_H}^{(i,11)} &= & R_7^{(i)} \\
H_2: \quad & \frac{dC}{d\theta_H}^{(i,12)} &= & R_8^{(i)} - R_9^{(i)}
\end{aligned} \tag{6.92}$$

where $C^{(i,j)}$ denotes a spices concentration and $R_k^{(i)}$ denotes a reaction rate.

6.2.4 Rate Laws

The reaction rates [6] are

$$
\begin{aligned}
R_1^{(i)} &= k_1 \theta_H^{(i)\alpha_1} C^{(i,1)} C^{(i,2)} \left(\frac{\rho_o^{(i)}}{\rho^{(i)}} \right) u_s(P^{(i)} - P_{ign}) \\
R_2^{(i)} &= k_2 \theta_H^{(i)\alpha_2} C^{(i,3)} C^{(i,2)} \left(\frac{\rho_o^{(i)}}{\rho^{(i)}} \right) u_s(P^{(i)} - P_{ign}) \\
R_3^{(i)} &= k_3 \theta_H^{(i)\alpha_3} C^{(i,5)} C^{(i,6)} \left(\frac{\rho_o^{(i)}}{\rho^{(i)}} \right) u_s(P^{(i)} - P_{ign}) \\
R_4^{(i)} &= k_4 \theta_H^{(i)\alpha_4} C^{(i,8)} u_s(P^{(i)} - P_{ign}) \\
R_5^{(i)} &= k_5 \theta_H^{(i)\alpha_5} C^{(i,2)} C^{(i,6)} \left(\frac{\rho_o^{(i)}}{\rho^{(i)}} \right) u_s(P^{(i)} - P_{ign}) \\
R_6^{(i)} &= k_6 \theta_H^{(i)\alpha_6} C^{(i,8)} C^{(i,6)} \left(\frac{\rho_o^{(i)}}{\rho^{(i)}} \right) u_s(P^{(i)} - P_{ign}) \\
R_7^{(i)} &= k_7 \theta_H^{(i)\alpha_7} C^{(i,1)} u_s(P^{(i)} - P_{ign}) \\
R_8^{(i)} &= k_8 \theta_H^{(i)\alpha_8} C^{(i,6)} u_s(P^{(i)} - P_{ign}) \\
R_9^{(i)} &= k_9 \theta_H^{(i)\alpha_9} C^{(i,12)} C^{(i,2)} \left(\frac{\rho_o^{(i)}}{\rho^{(i)}} \right) u_s(P^{(i)} - P_{ign})
\end{aligned} \tag{6.93}
$$

where species concentrations $C^{(i,j)}$ and species masses are related by

$$C^{(i,j)} = \frac{s^{(i,j)}}{\nu^{(i)} \mathbb{M}^{(j)}} \tag{6.94}$$

Note that a thermostat was used to cool the RMD system; it's functional form is discussed in reference [6]. In these expressions $\rho^{(i)}$ and $\rho_o^{(i)}$ are the element density and the element reference density. The rate law constants k_k and the exponents α_k are listed in Table 6.2. The parameter $\nu^{(i)}$ is an element volume, while $\mathbb{M}^{(j)}$ is the species molar mass listed in Table 6.3. Note that pressure based ignition criteria are used, with $P_{ign} = 2.89\ GPa$.

The state equations for the chemical subsystem determine the source terms in the reacted mass evolution equations as well as the reaction source terms in the species mass evolution equations. The macroscale HMX simulation employs $\zeta_o = \frac{1}{17}\ GPa^{-1}$, obtained from the mesoscale simulation results. The parameters for the macroscale reaction source terms are listed in Tables 6.2 and 6.3.

6.2.5 Equations of State

In this section element superscripts are omitted, for clarity. The macroscale reaction progress variable λ^{mac} is defined by

$$\lambda^{mac} = \frac{\bar{C} - \bar{C}_0}{\bar{C}_1 - \bar{C}_0} \qquad 0 \leq \lambda^{mac} \leq 1 \tag{6.95}$$

and

$$\bar{C} = \frac{s^{(j)}}{m} \frac{\mathbb{M}^{solid}}{\mathbb{M}^{(j)}} \tag{6.96}$$

where $\bar{C}$ is a selected species concentration ratio (O_2 is chosen here), $\bar{C}_0$ is an initial species concentration ratio, and $\bar{C}_1$ is a final concentration ratio (the units of these concentration ratios are moles per unit mole of solid reactant), $\mathbb{M}^{solid}$ is the molar mass of the solid, and $\mathbb{M}^{(j)}$ is the molar mass of species j. The relevant parameters are listed in Table 6.3.

In the case of final product gases which admit an analytic equation of state, the simulation employs a Mie-Grüneisen form. Otherwise, an empirical detonation gas EOS is assumed to apply. The pressure of the gas mixture is

then defined as a summation of partial pressures

$$P_{mix} = \sum {C_s}^2 (\rho_k - \rho_o) + \gamma \rho_o (e - e_o), \qquad k = 1, 3, 4, 7, 9, 12 \tag{6.97}$$

where the density of each species ρ_k is determined by the mixture density ρ and its mass fraction Y_k

$$\rho_k = Y_k \rho \tag{6.98}$$

and the EOS coefficients are listed in Table 6.6 [68, 75–78].

The element pressure is finally defined by

$$P = (1 - f) P_{solid} + f_{non} P_{det} + f_{ana} \left[(1 - \lambda^{mac}) P_{det} + \lambda^{mac} P_{gas} \right] \tag{6.99}$$

where f is the solid mass fraction. The mass fraction fraction f_{non} for the non-analytic species O, OH, H, N, NH_3, C_2 is defined as

$$f_{non} = \sum Y_k, \qquad k = 2, 5, 6, 8, 10, 11 \tag{6.100}$$

and the mass fraction f_{ana} for the analytic species C, CO, CO_2, H_2O, N_2, H_2 is defined as

$$f_{ana} = \sum Y_k, \qquad k = 1, 3, 4, 7, 9, 12 \tag{6.101}$$

The solid equation of state takes a Mie-Grüneisen form [72]

$$P_{solid} = C_s^2 (\rho - \rho_o) + \gamma \rho_o (e - e_o) \tag{6.102}$$

$$\theta_{solid} = \frac{1}{C_v} (e - e_o) \tag{6.103}$$

where θ denotes the temperature, C_s denotes the sound speed, ρ denotes the density, γ denotes the Grüneisen coefficient, and e denotes an internal energy

per unit mass. Note that ρ_o and e_o are reference density and reference internal energy respectively. The EOS parameters are listed in Table 6.4.

The detonation products are modeled using a JWL equation of state [67, 84]

$$P_{det} = A\left(1-\frac{\omega}{R_1\mu}\right)e^{-R_1\mu} + B\left(1-\frac{\omega}{R_2\mu}\right)e^{-R_2\mu} + \hat{P} \quad (6.104)$$

$$\theta_{det} = \frac{1}{C_v}(e-e_o) \quad (6.105)$$

where

$$\mu = \frac{\rho_o}{\rho}, \qquad \hat{P} = \omega\frac{(e+e_i)}{\mu} \quad (6.106)$$

with the JWL coefficients A, B, R_1, R_2, ω, and e_i are listed in Table 6.5.

The mixture temperature is defined as

$$\theta = (1-f)\theta_{solid} + \sum_{k=1}^{N_s} Y_k\theta_k \quad (6.107)$$

where the partial temperatures θ_k are

$$\begin{cases} \theta_k = \theta_{det}, & k = 2,5,6,8,10,11 \text{ for } O, OH, H, N, NH_3, C_2 \\ \theta_k = \frac{1}{C_v}(e-e_o), & k = 1,3,4,7,9,12 \text{ for } C, CO, CO_2, H_2O, N_2, H_2 \end{cases}$$

6.2.6 Simulation Results

The macrocale validation simulation for HMX models a flyer plate impact experiment for a 25 mm long HMX explosive sample. Figure 6.18 shows a schematic of simulation. The explosive samples are symmetrically positioned on both sides of a plane of symmetry; the elements near the plane of symmetry are assigned initial velocities of 2 km/s, as indicated in Figure 6.19. The

detonation is initiated away from the wall, and propagates in both directions, resulting in a waves collision at the plane of symmetry. The outward moving shock fronts propagate, generating a steady state detonation. The simulation results may be compared to published experimental data on the von Neumann spike state, the Chapman-Jouguet state, and the detonation wave speed, all of which are listed in Table 6.7. As in the mesoscale case, we compare to average experimental data. A fourth order Runge-Kutta method was employed to integrate the ODE model.

The simulation results are in good agreement with the experimental data for von Neumann spike pressures (dotted lines) and Chapman-Jouguet pressures (dashed lines), as shown in Figure 6.20. Figure 6.21 shows that the particle velocity profiles are also in good agreement with steady state von Neumann velocity (dotted lines) and steady state CJ velocity (dashed lines) data. Note that the experimental pressure and velocity values used for validation represent peak values, not plateaus. Figure 6.22 shows the computed temperatures. The species mass fraction distributions are plotted in Figures 6.23-6.28 (corresponding experimental data is not available for comparison). In this simulation the reaction zone spans six elements, and the energy conservation error is 0.108 percent.

Figure 6.29 shows both: (1) converged results as model resolution is increased, and (2) good agreement with published experimental data for the detonation velocity in HMX (the red dashed line indicate the experimental results [13].

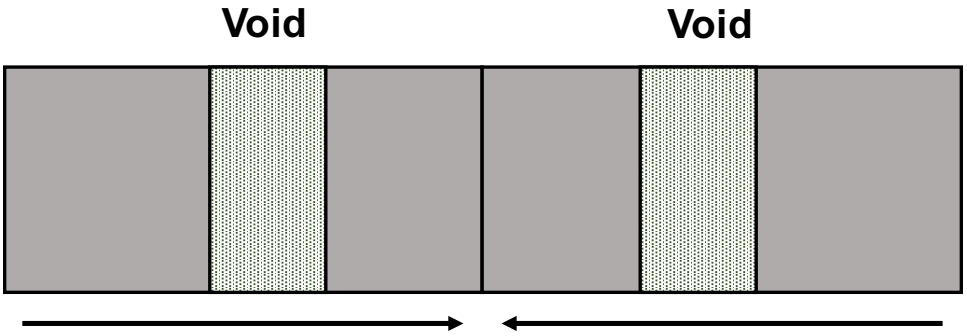

Figure 6.1: Mesoscale simulation of shock induced detonation.

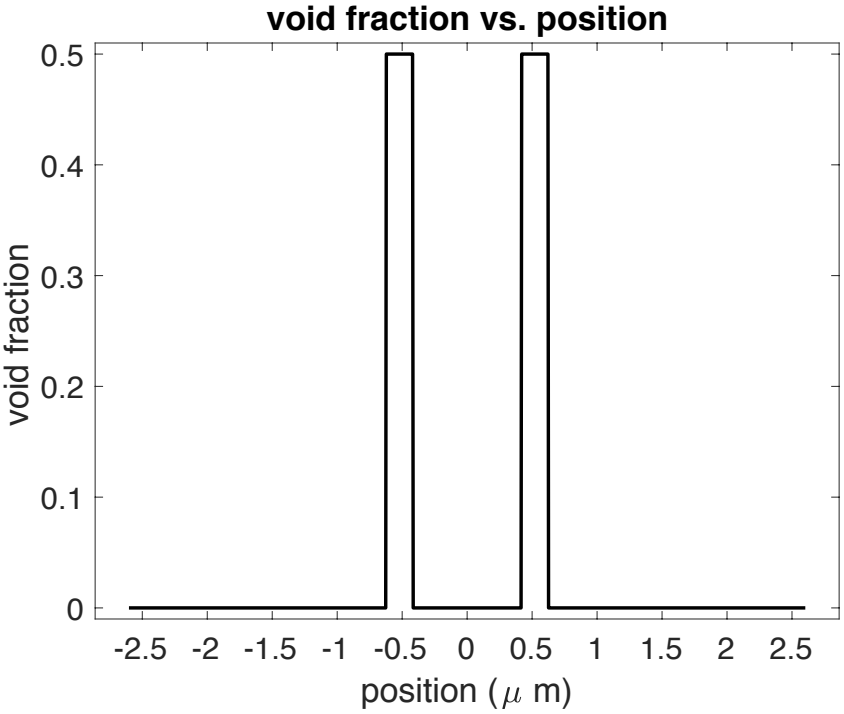

Figure 6.2: Void fraction distribution: mesoscale simulation in HMX.

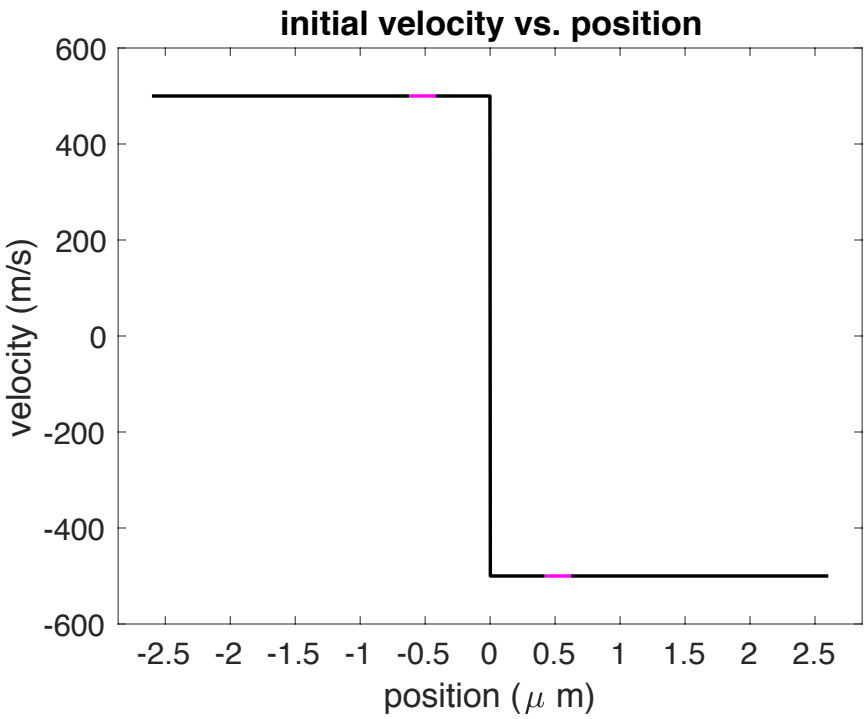

Figure 6.3: Initial velocity distribution: mesoscale simulation in HMX. The magenta colored lines denote the void regions.

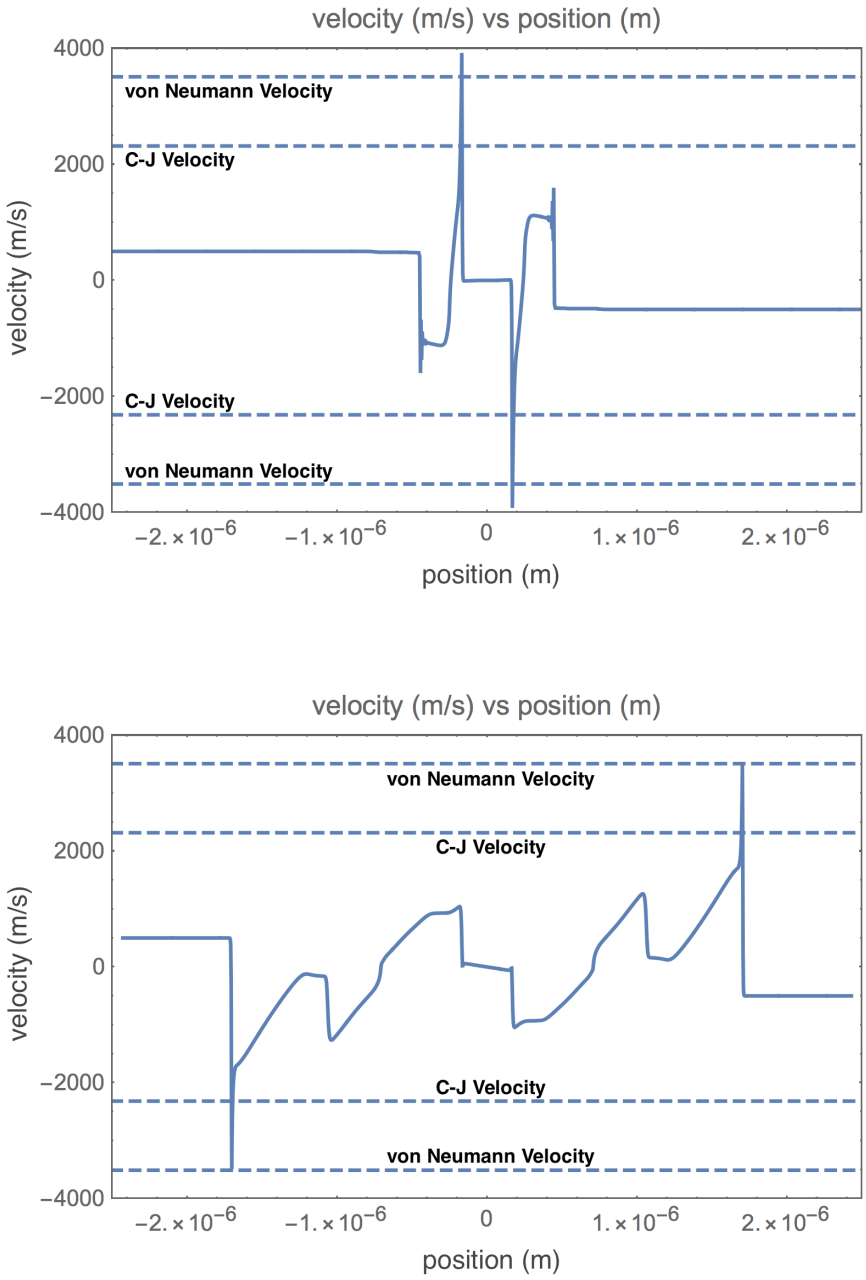

Figure 6.4: Mesoscale simulation of shock induced detonation in HMX: particle velocities at 0.182 ns (upper figure) and at 0.350 ns (lower figure). The dashed lines denote steady state von Neumann velocity (3510 m/s) and Chapman-Jouguet velocity (2316.7 m/s) from the published experimental data listed in Table 6.7.

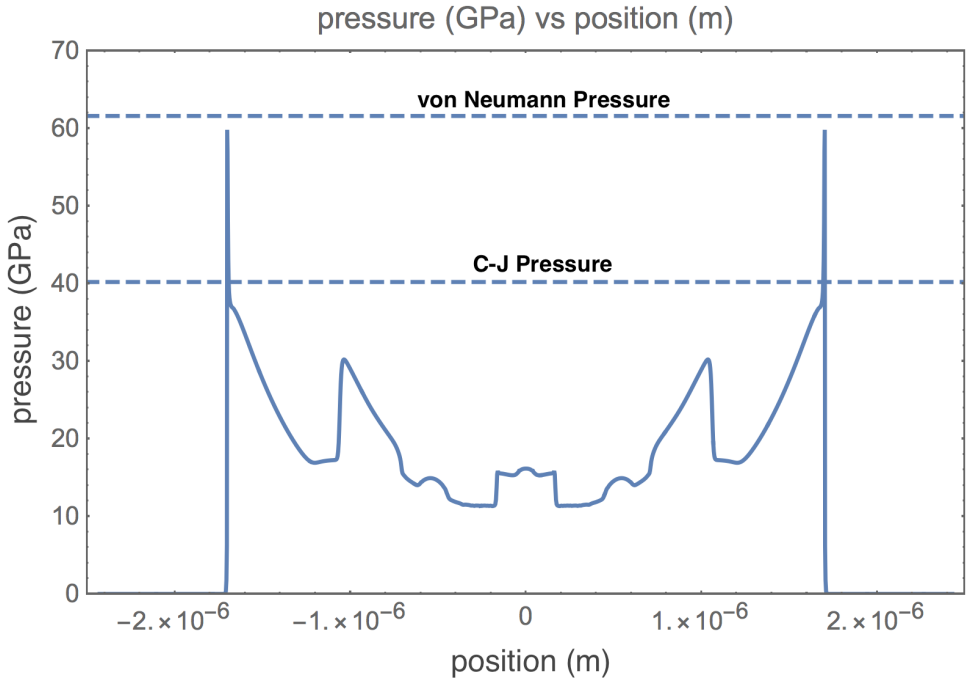

Figure 6.5: Mesoscale simulation of shock induced detonation in HMX: pressure. The dashed lines denote Chapman-Jouguet (40.2 GPa) pressure and von Neumann peak (61.6 GPa) pressure from published experimental data listed in Table 6.7

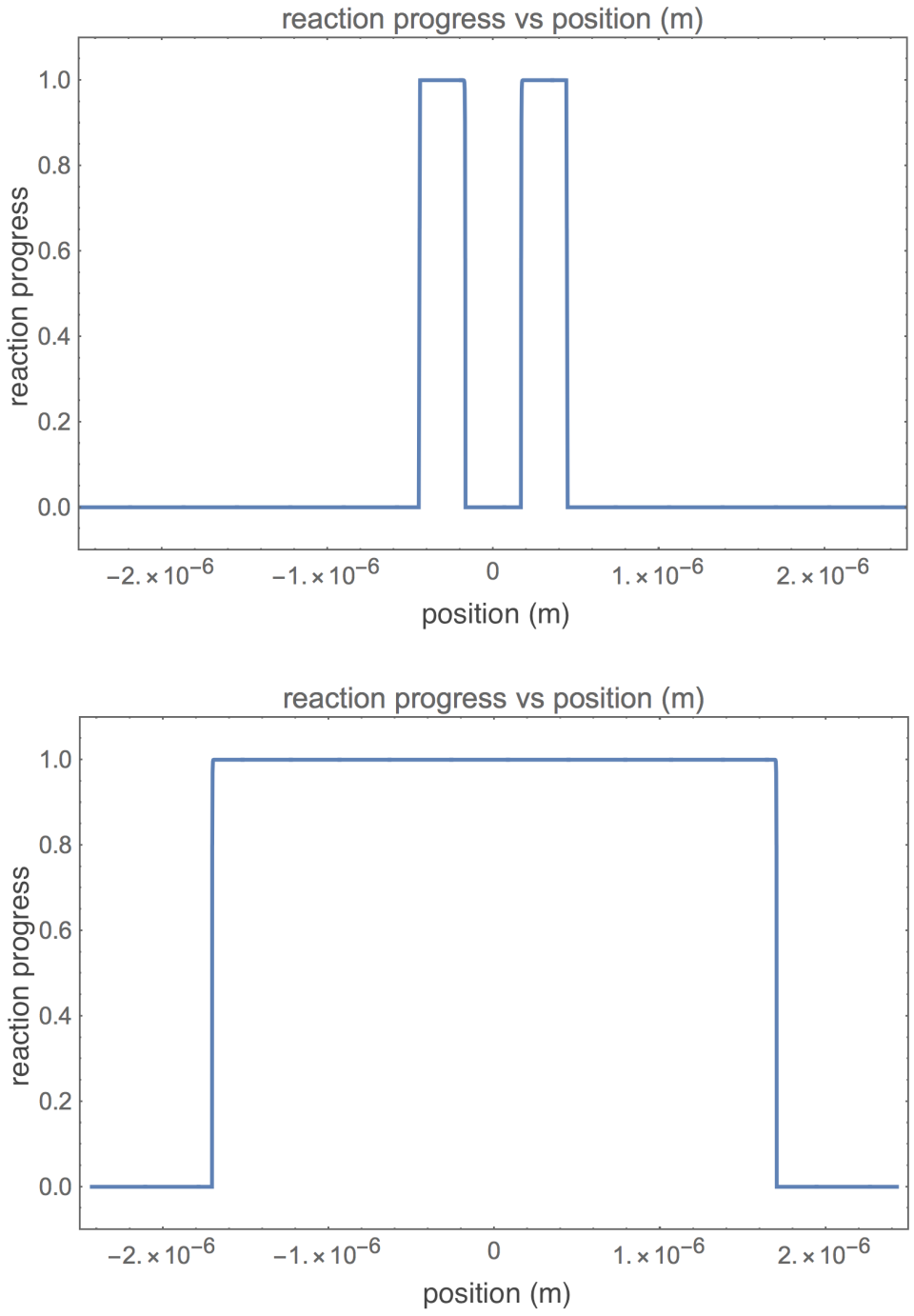

Figure 6.6: Mesoscale simulation of shock induced detonation in HMX: reaction progress variable at 0.182 ns (upper figure) and at 0.350 ns (lower figure).

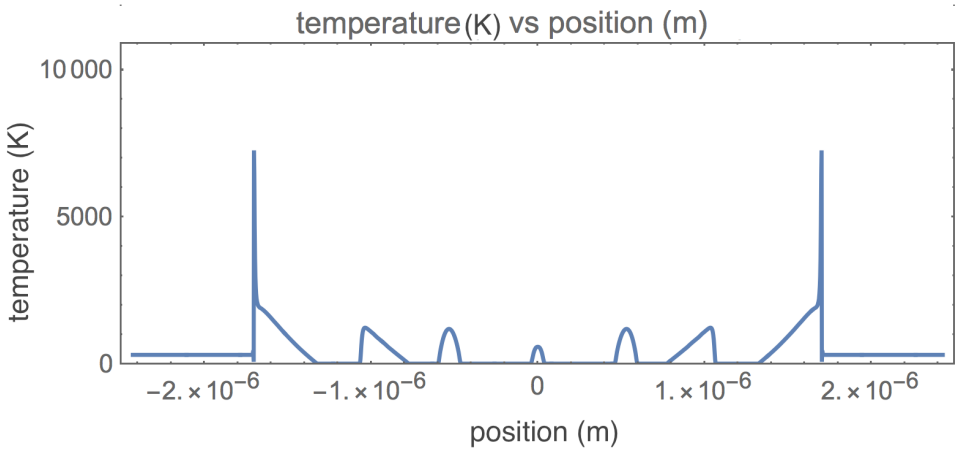

Figure 6.7: Mesoscale simulation of shock induced detonation in HMX: tempreautre.

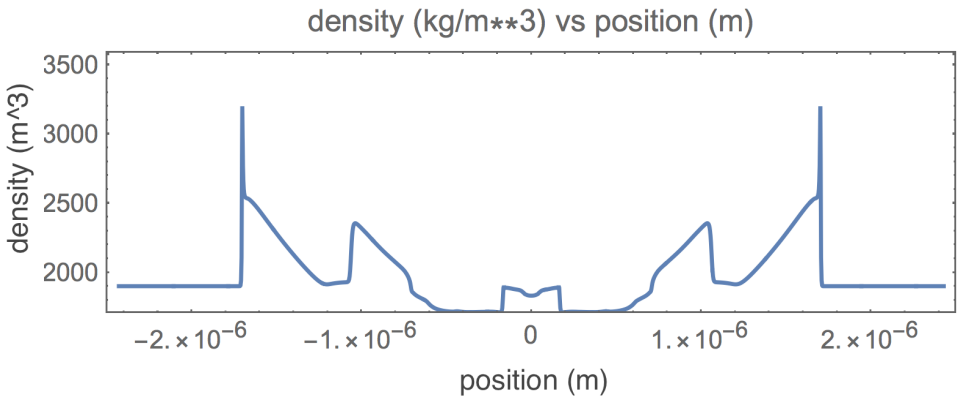

Figure 6.8: Mesoscale simulation of shock induced detonation in HMX: density.

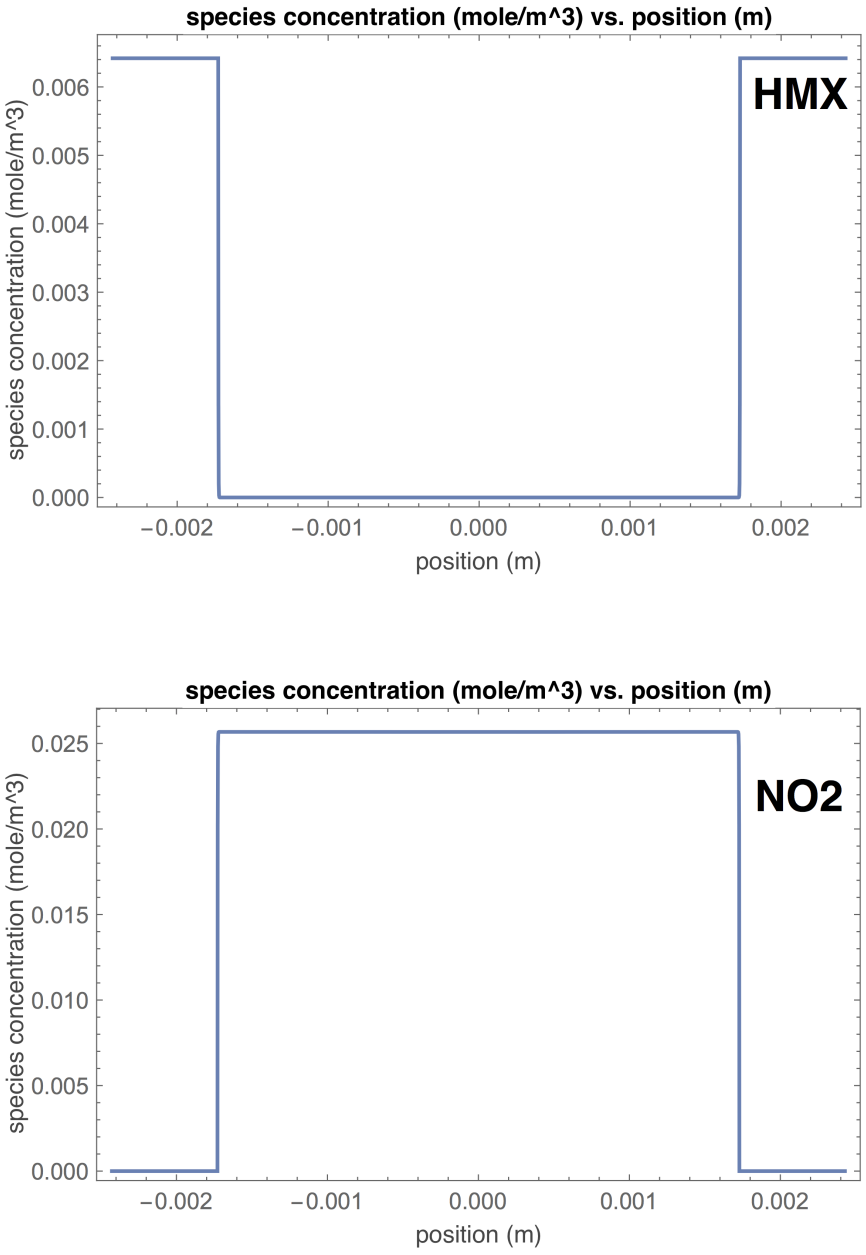

Figure 6.9: Mesoscale simulation of shock induced detonation in HMX: species concentrations for HMX and NO_2.

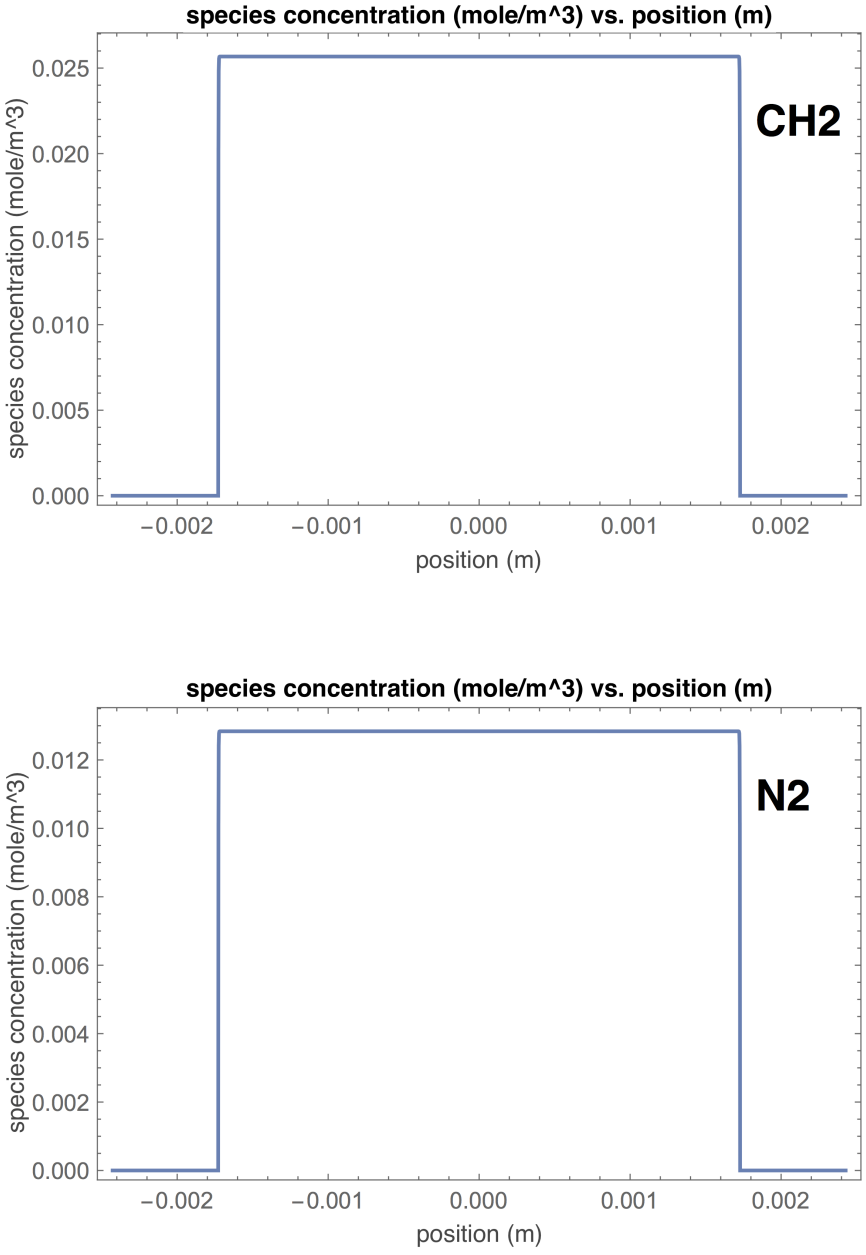

Figure 6.10: Mesoscale simulation of shock induced detonation in HMX: species concentrations for CH_2 and N_2.

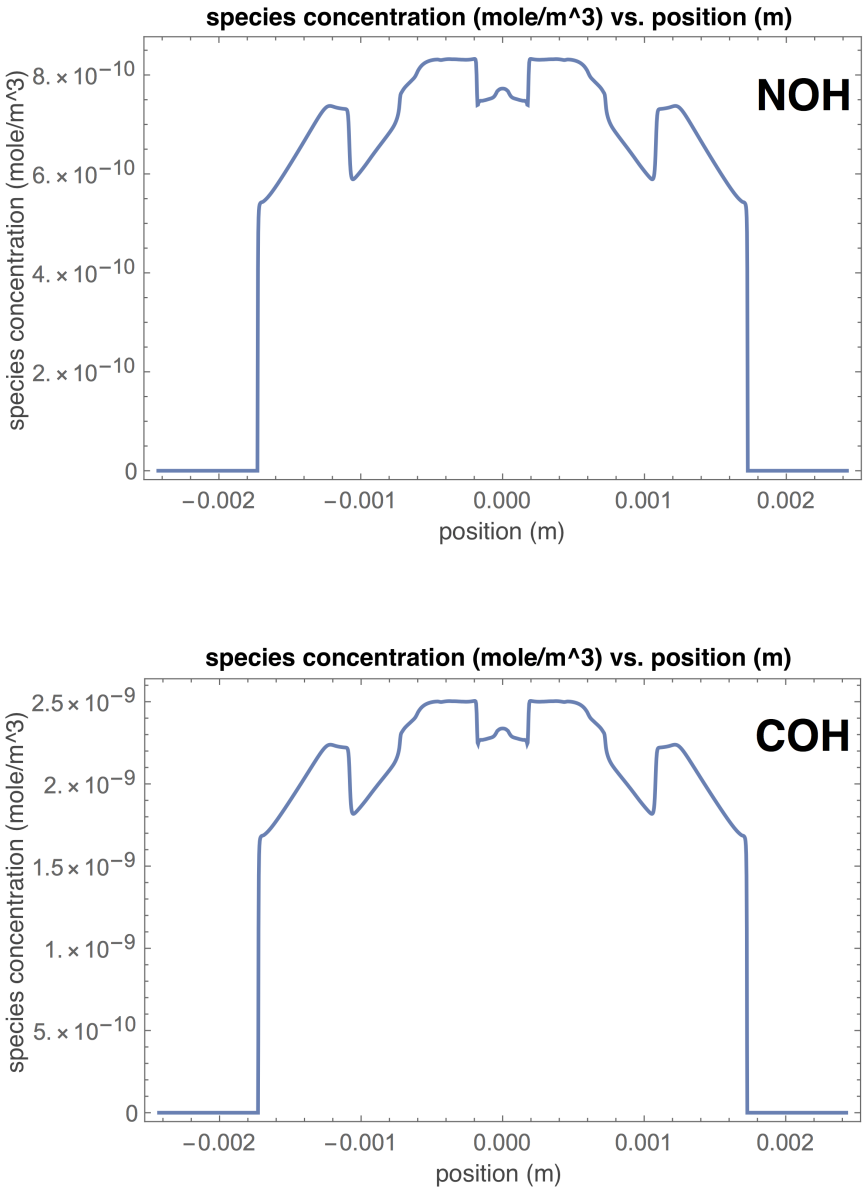

Figure 6.11: Mesoscale simulation of shock induced detonation in HMX: species concentrations for NOH and COH.

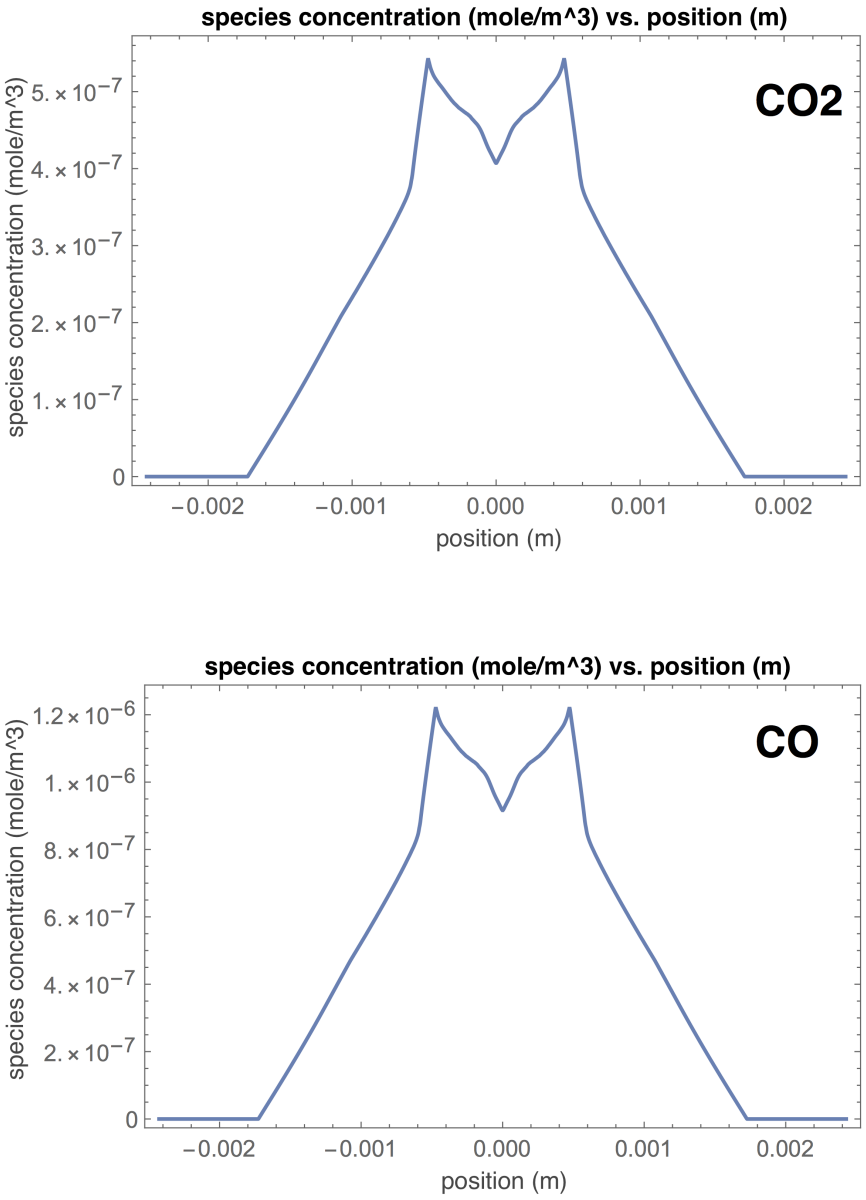

Figure 6.12: Mesoscale simulation of shock induced detonation in HMX: species concentrations for CO_2 and CO.

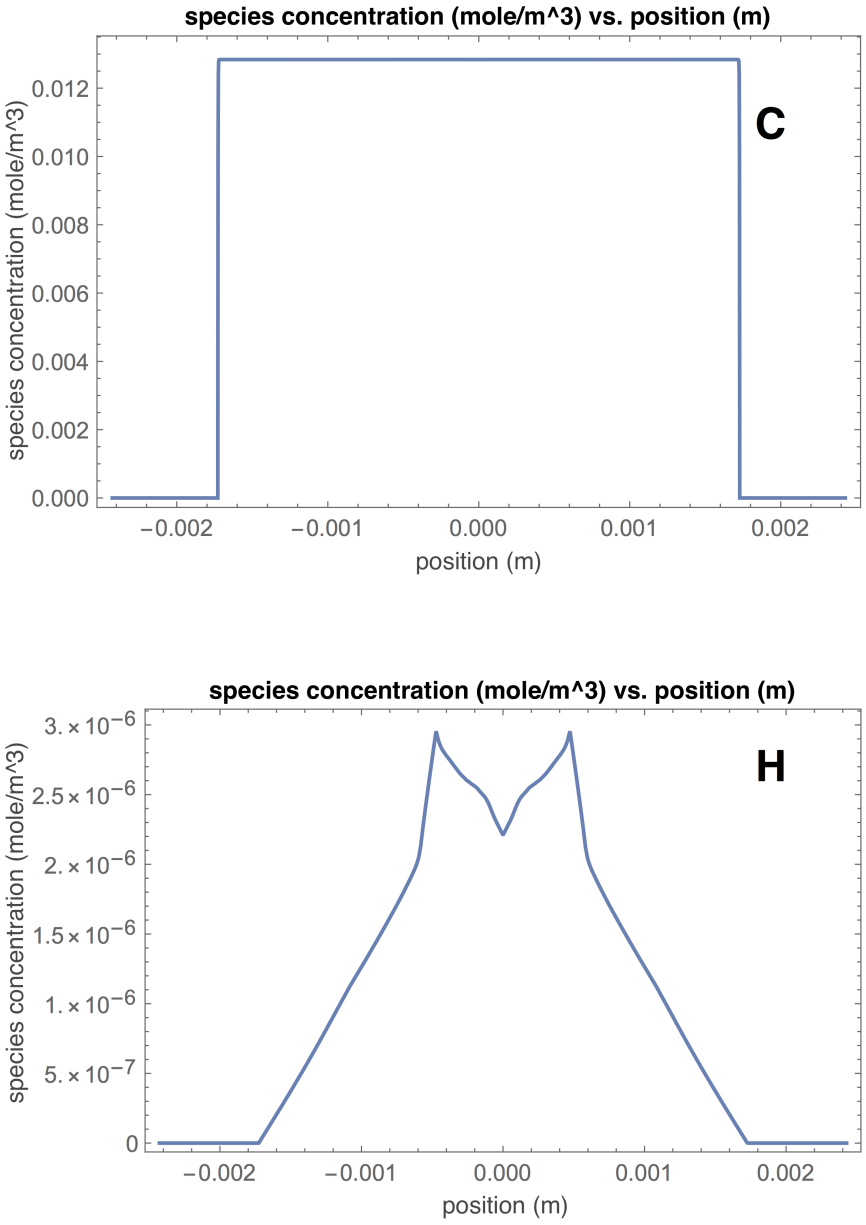

Figure 6.13: Mesoscale simulation of shock induced detonation in HMX: species concentrations for C and H.

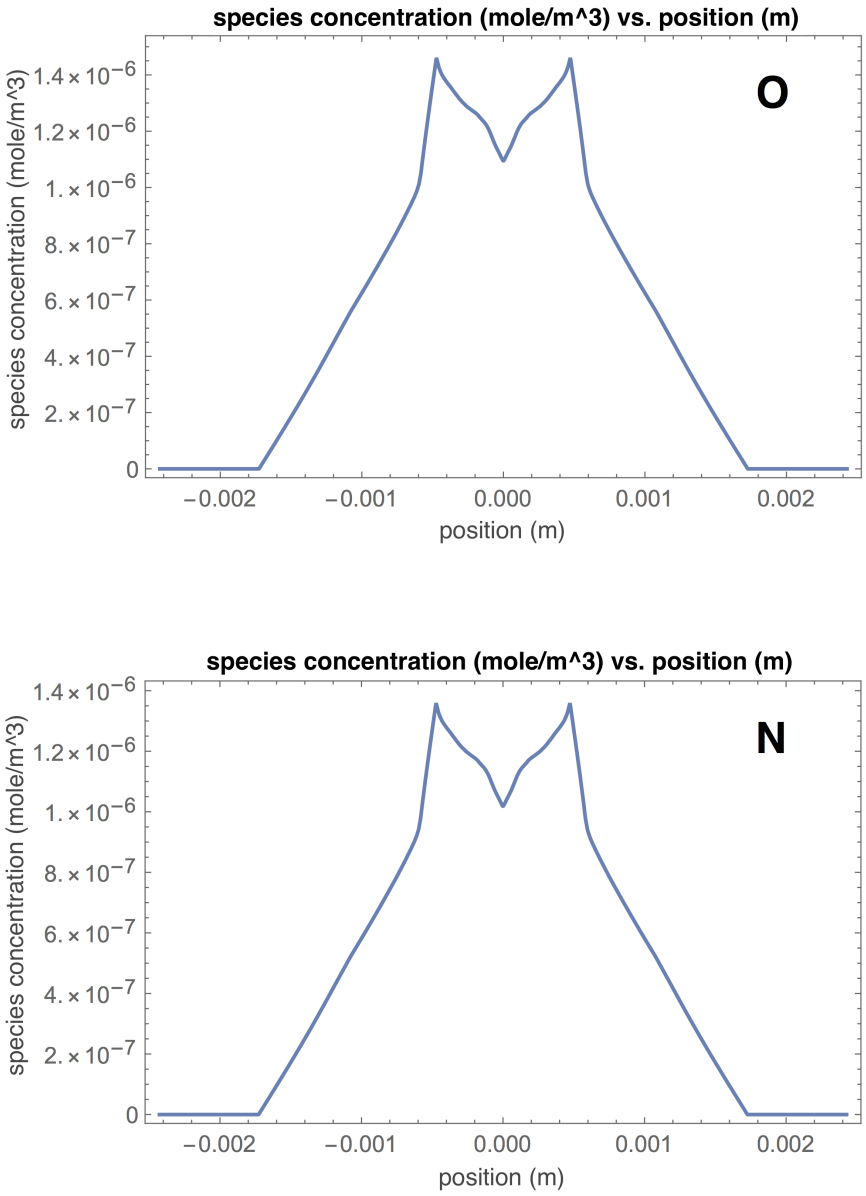

Figure 6.14: Mesoscale simulation of shock induced detonation in HMX: species concentrations for O and N.

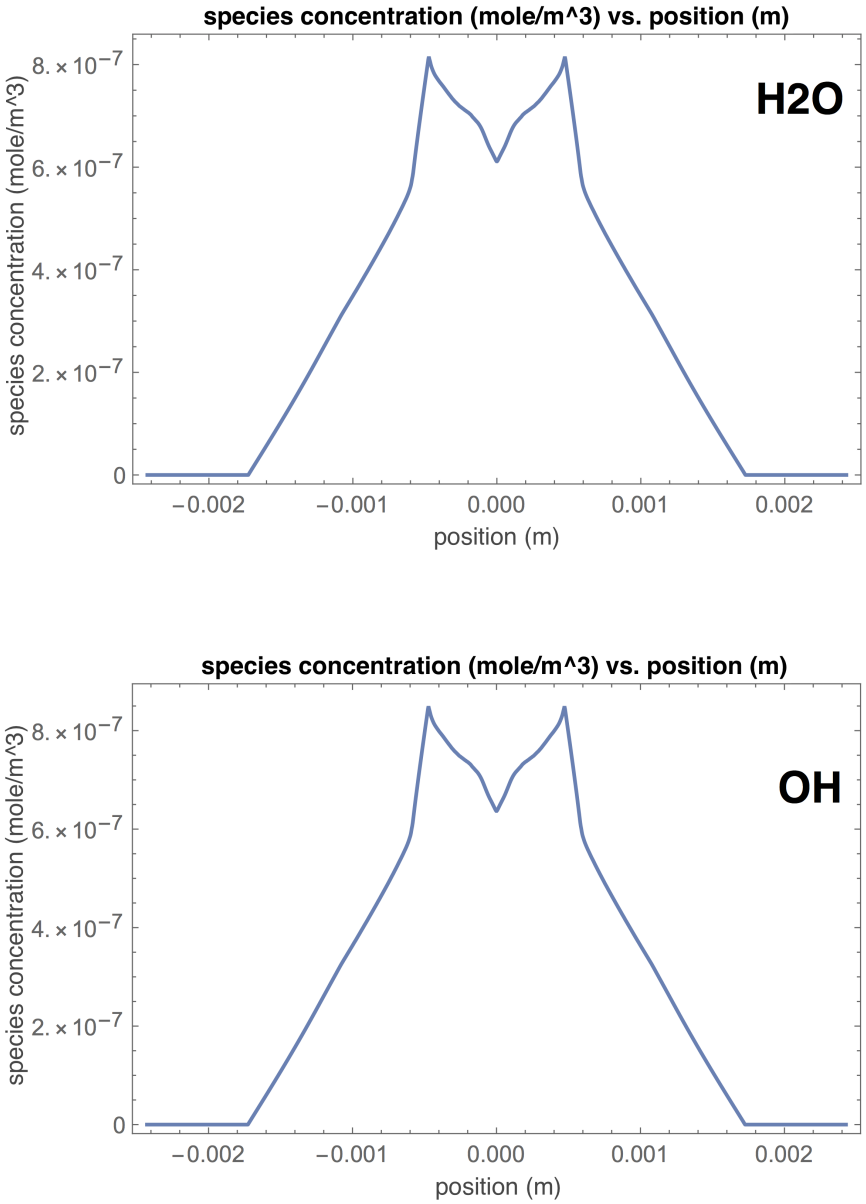

Figure 6.15: Mesoscale simulation of shock induced detonation in HMX: species concentrations for H_2O and OH.

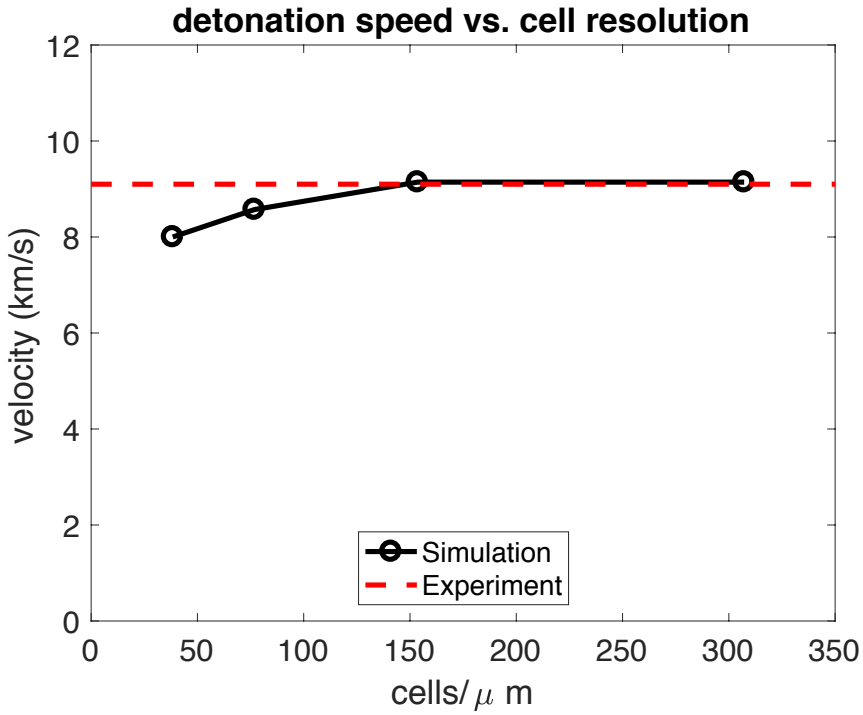

Figure 6.16: Convergence test: mesoscale simulation in HMX.

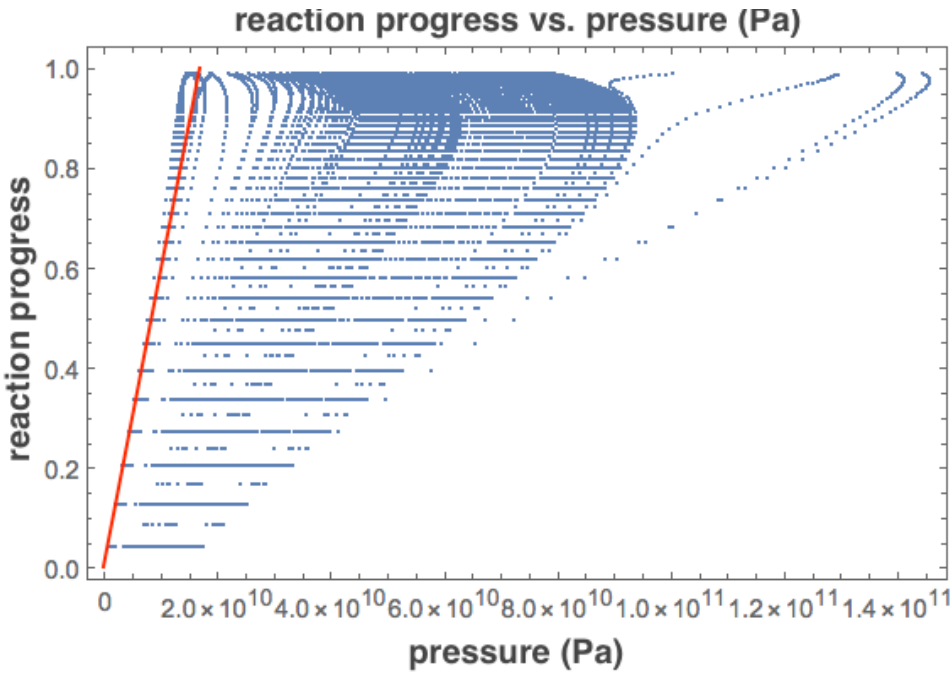

Figure 6.17: Reaction progress variable versus pressure (Pa) in HMX. The red line denotes the linear slope ($\zeta_o = \frac{1}{17}\ GPa^{-1}$).

Figure 6.18: Macroscale simulation of shock induced detonation.

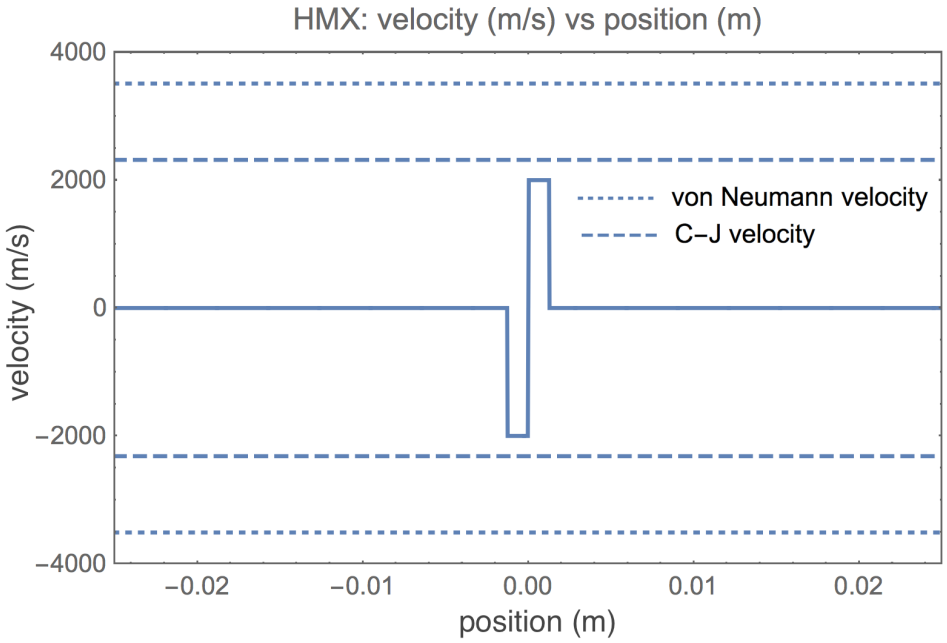

Figure 6.19: Initial velocities of macroscale simulation in HMX.

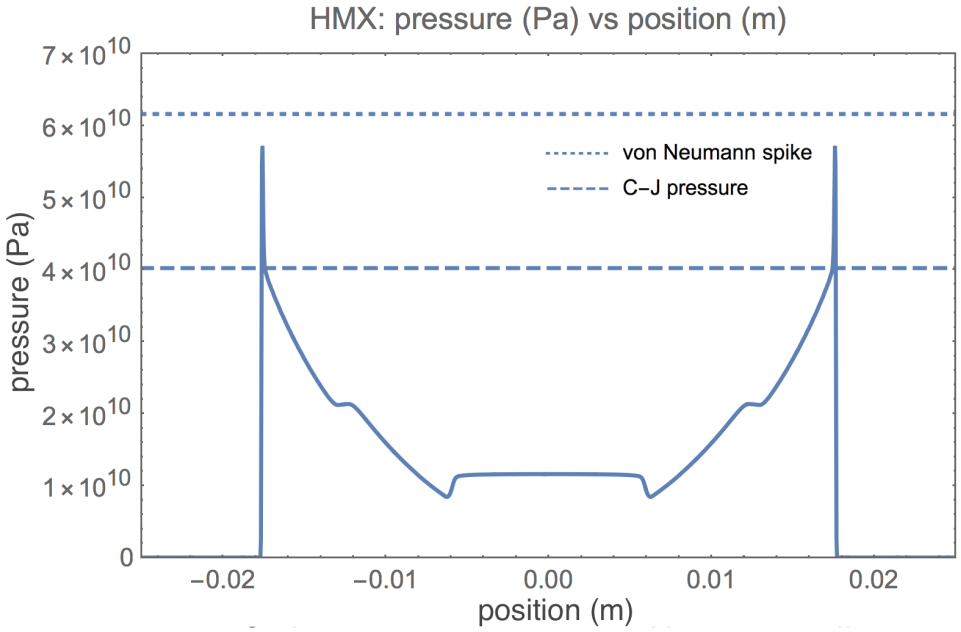

Figure 6.20: Macroscale simulation of shock induced detonation in HMX: pressure. The dotted line denotes the Chapman-Jouguet (40.2 GPa) pressure, and the dashed line denotes the von Neumann peak (61.6 GPa) pressure from the published experimental data listed in Table 6.7

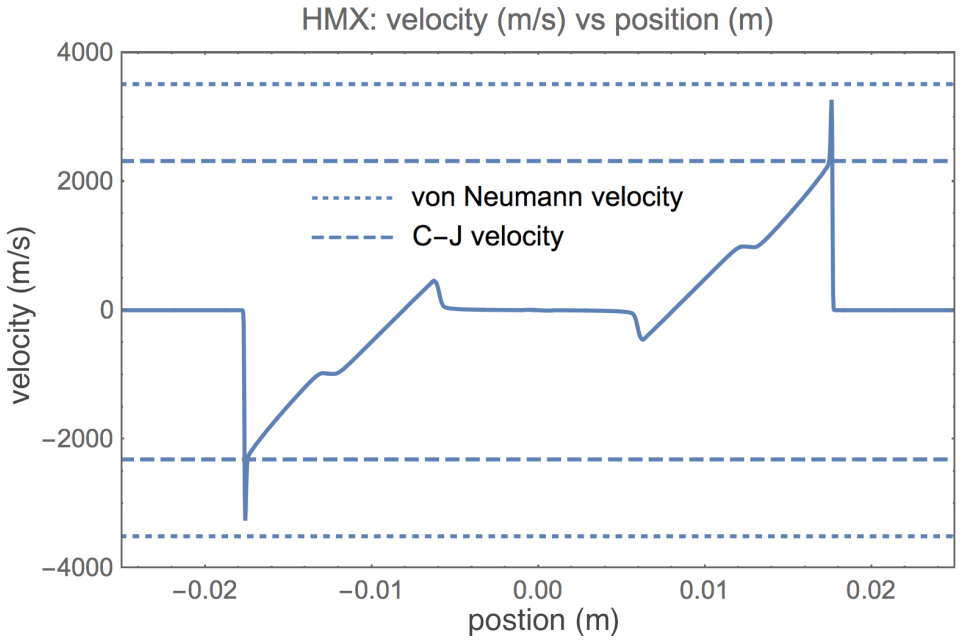

Figure 6.21: Macroscale simulation of shock induced detonation in HMX: velocity. The dotted line denotes the von Neumann (3510 m/s) velocity while the dashed line denotes the Chapman-Jouguet velocity (2316.7 m/s) from the published experimental data listed in Table 6.7.

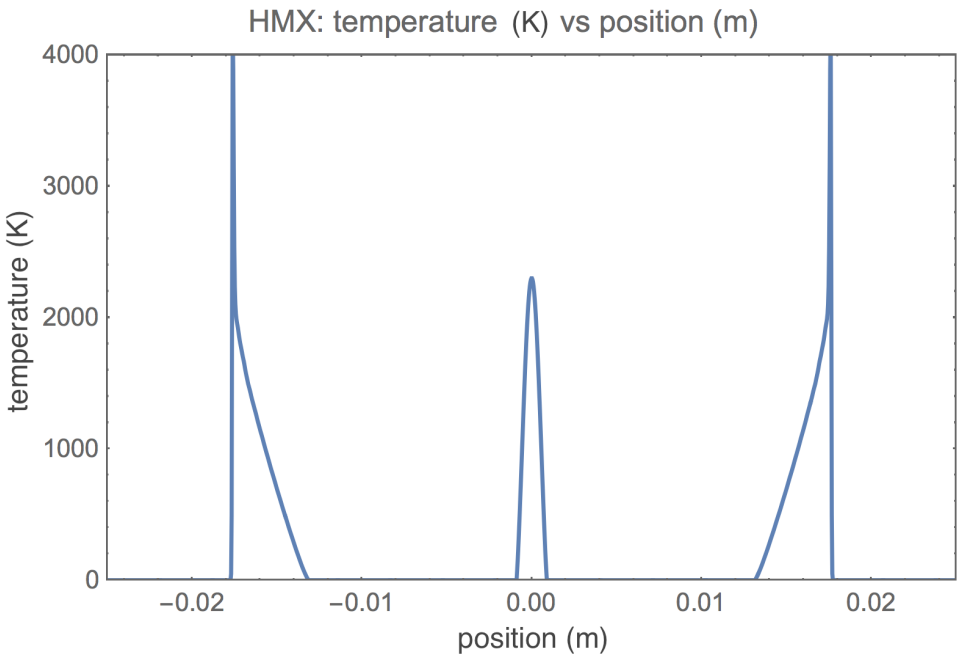

Figure 6.22: Macroscale simulation of shock induced detonation in HMX: temperature.

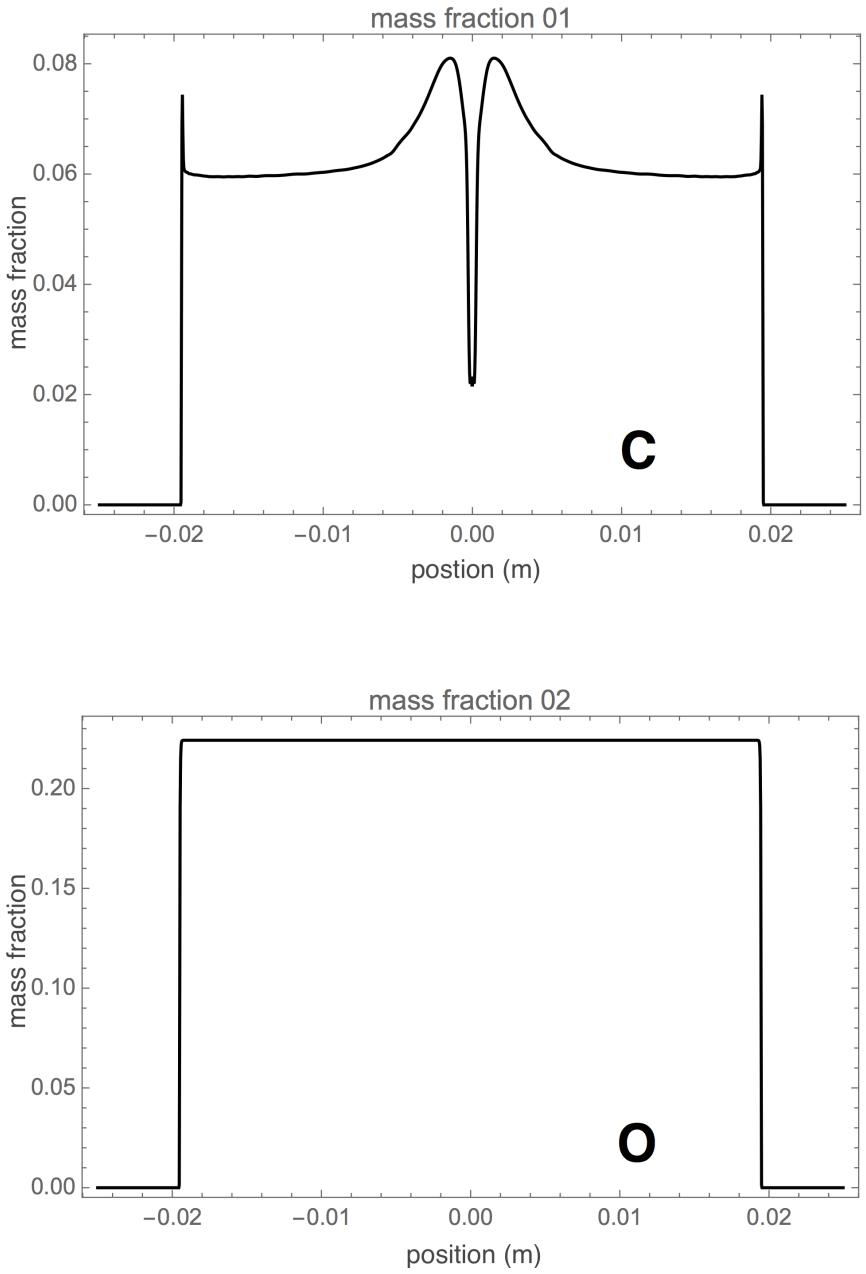

Figure 6.23: Macroscale simulation of shock induced detonation in HMX: species mass fractions for C and O.

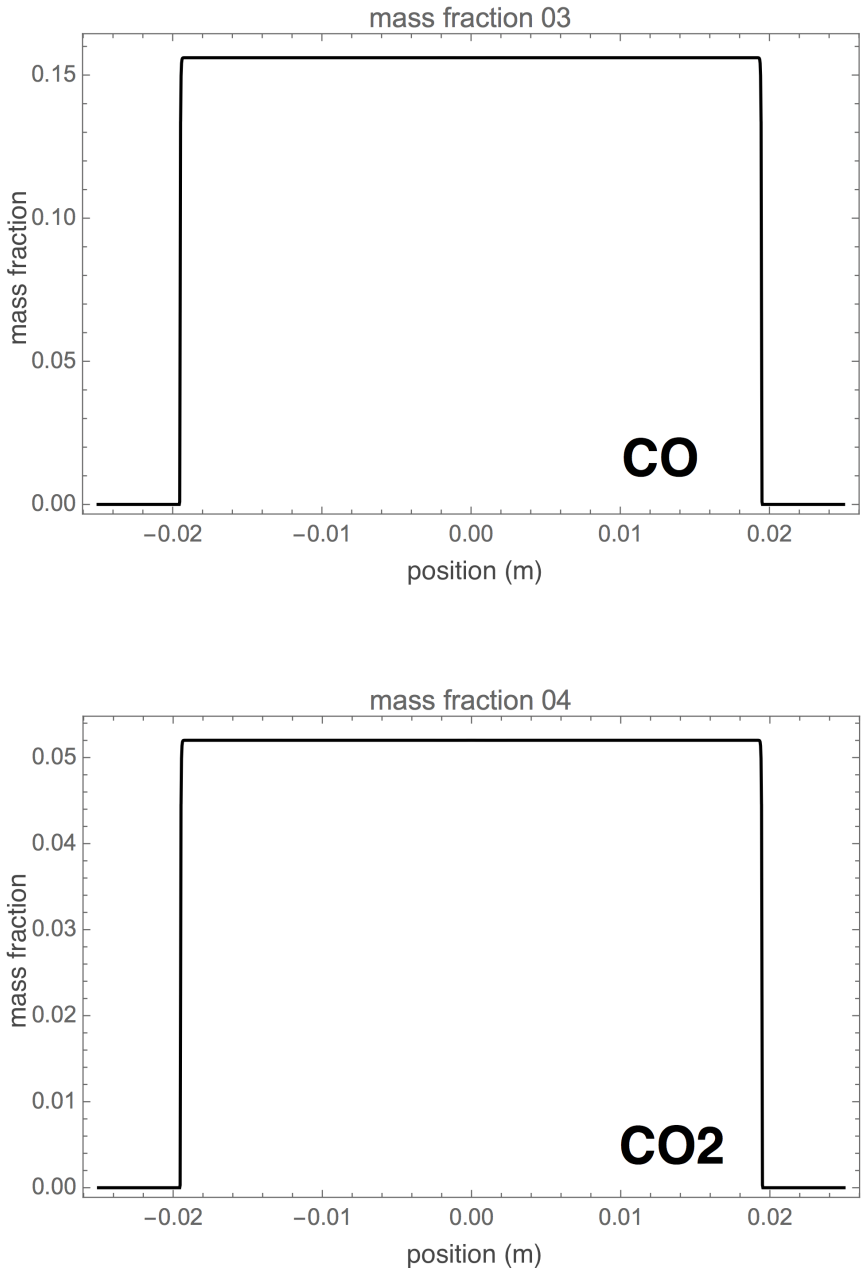

Figure 6.24: Macroscale simulation of shock induced detonation in HMX: species mass fractions for CO and CO_2.

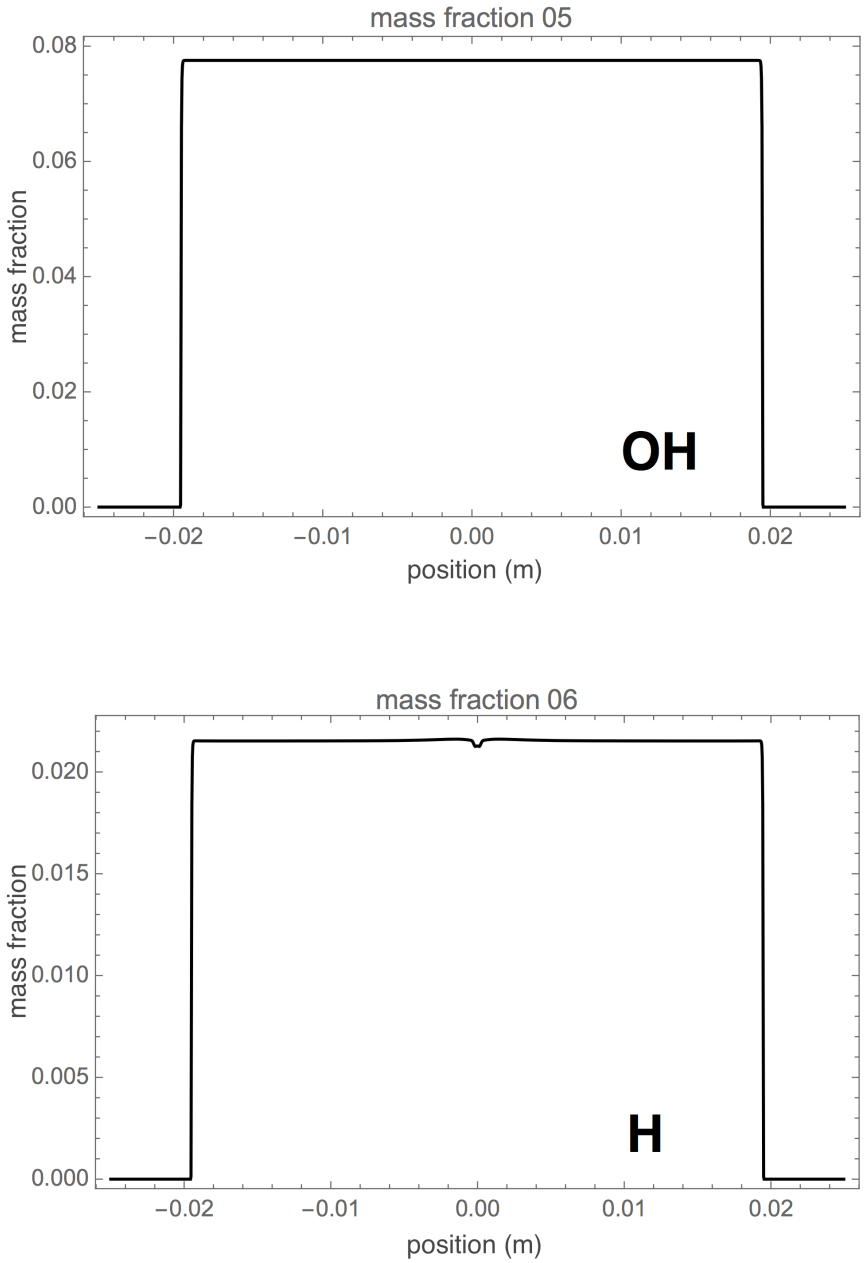

Figure 6.25: Macroscale simulation of shock induced detonation in HMX: species mass fractions for OH and H.

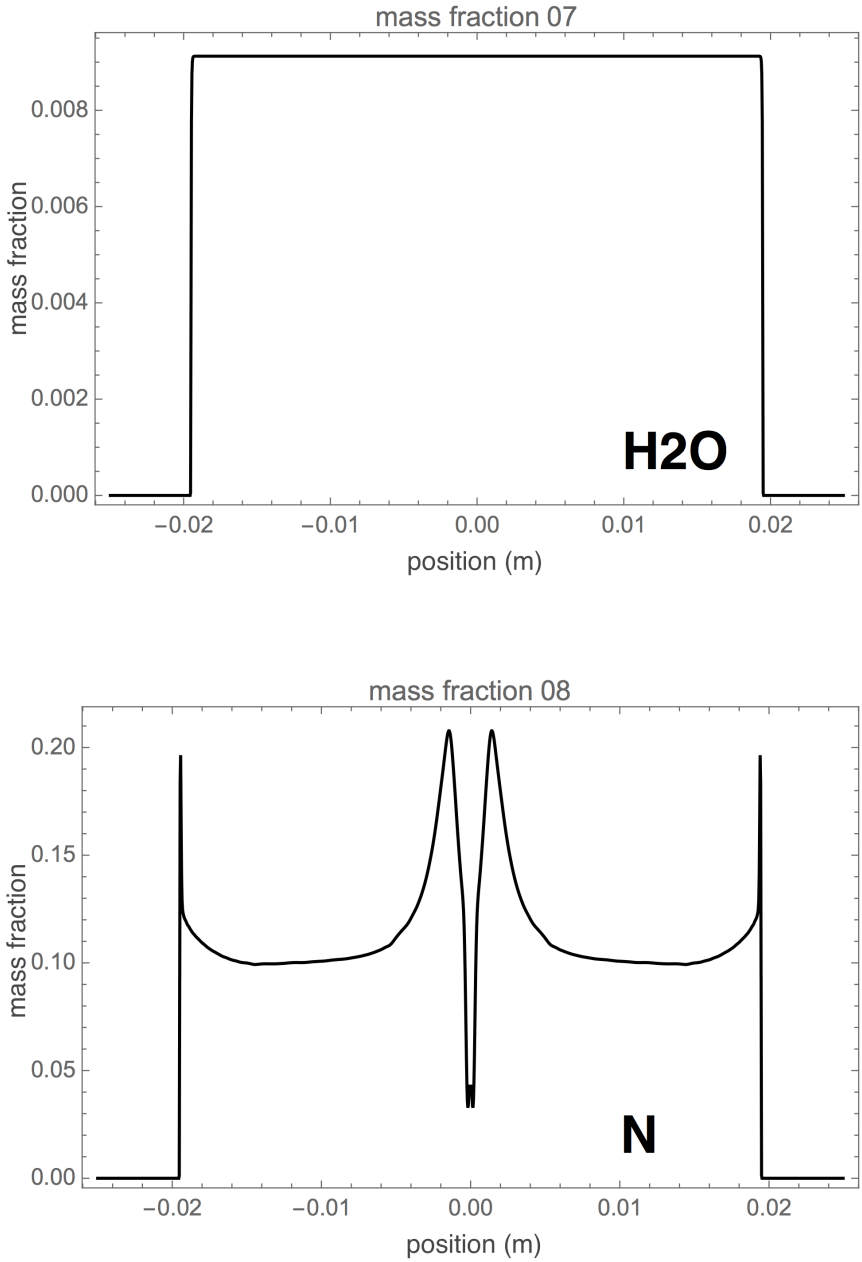

Figure 6.26: Macroscale simulation of shock induced detonation in HMX: species mass fractions for H_2O and N.

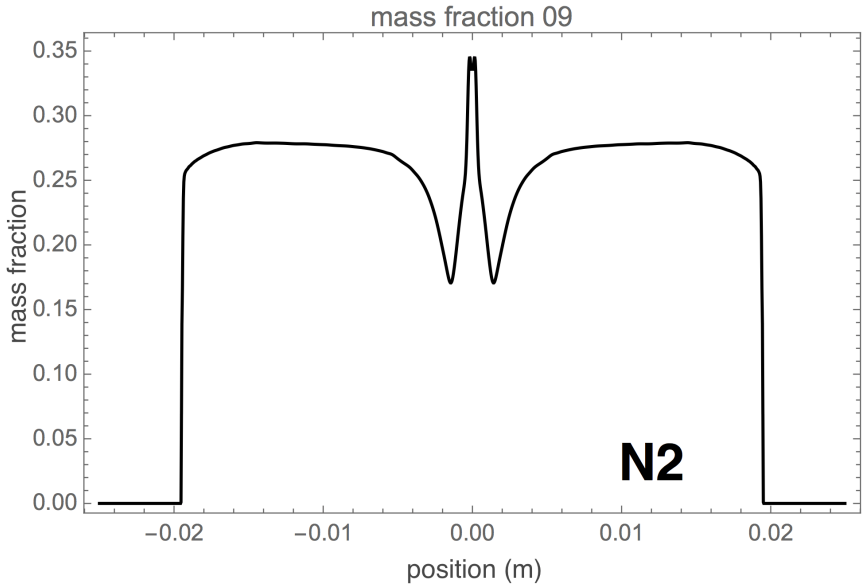

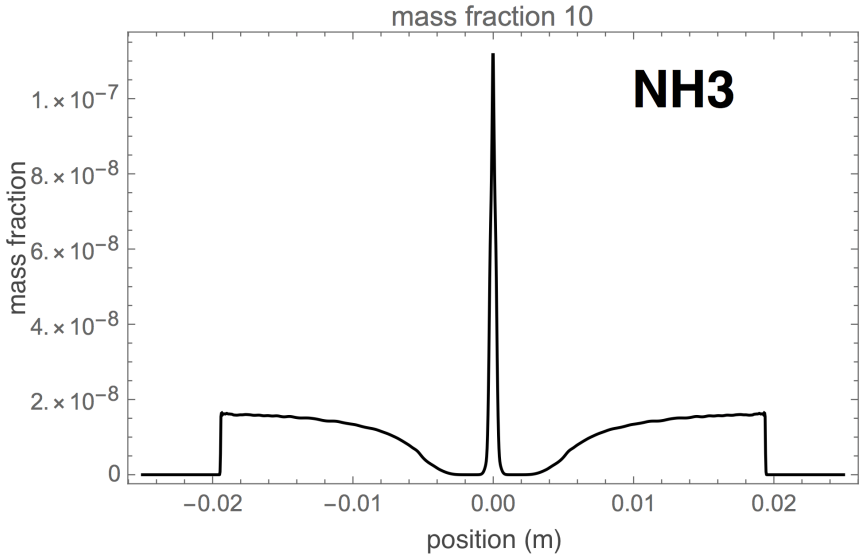

Figure 6.27: Macroscale simulation of shock induced detonation in HMX: species mass fractions for N_2 and NH_3.

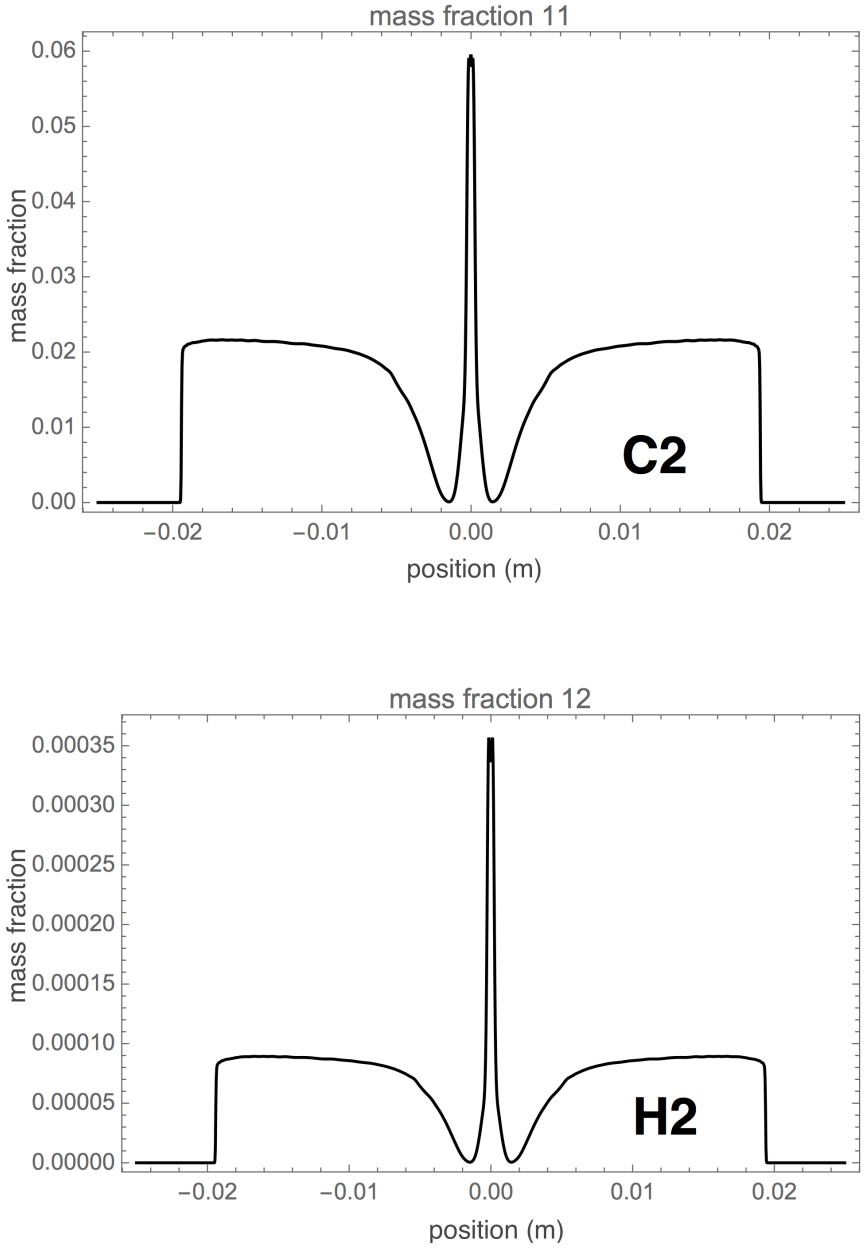

Figure 6.28: Macroscale simulation of shock induced detonation in HMX: species mass fractions for C_2 and H_2.

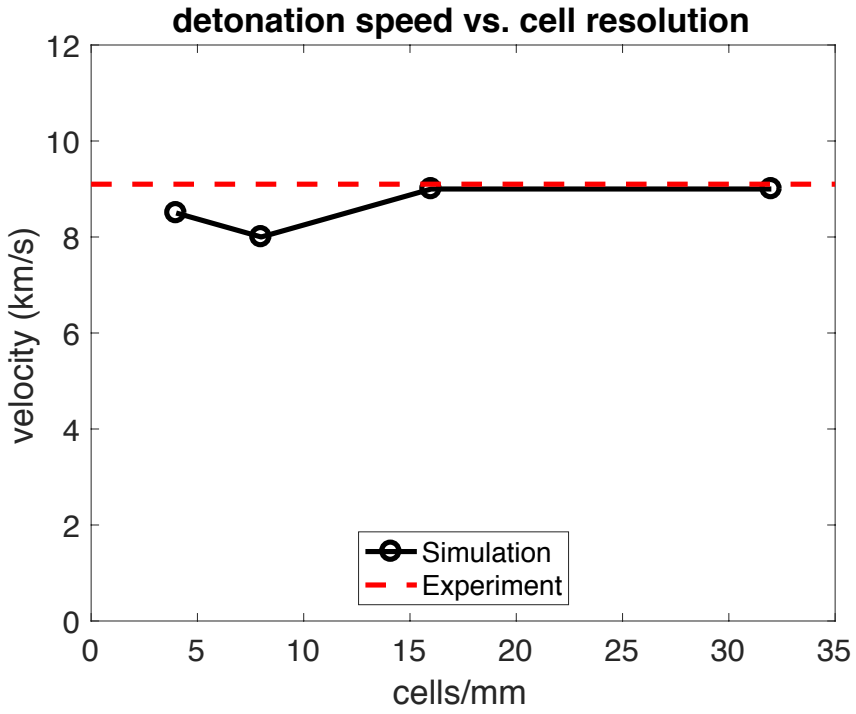

Figure 6.29: Convergence test: macroscale simulation in HMX.

Table 6.1: Rate law constants for the short time chemistry model in HMX [6].

j	k_j $(1/ps)(moles/cm^3)^{1-m^{(j)}}$	$m^{(j)}$
1	48.68	1.27
2	148.82	2.00
3	23.26	1.41
4	25.15	1.23

Table 6.2: Long time chemistry model for HMX [6].

i	Reaction			Rate constant (k_i) $(\frac{moles}{cm^3})^{1-m_i}$	Rate coefficient (α_i)	m_i
1	$C + O$	$\rightarrow$	CO	622.10	1.6519	2
2	$CO + O$	$\rightarrow$	CO_2	1454.4	2.9375	2
3	$OH + H$	$\rightarrow$	H_2O	1064.5	2.5222	2
4	$N + N$	$\rightarrow$	N_2	2.3172	0.6958	1
5	$O + H$	$\rightarrow$	OH	82.640	0.6583	2
6	$N + 3H$	$\rightarrow$	NH_3	2366.6	11.999	2
7	$C + C$	$\rightarrow$	C_2	2.3864	2.6451	1
8	$H + H$	$\rightarrow$	H_2	0.3390	2.3435	1
9	$H_2 + O$	$\rightarrow$	H_2O	0.0212	2.5449	2

Table 6.3: Long time chemistry model parameters for HMX.

No. (j)	Species	Initial state mole ratio $\bar{C}_0^{(j)}$ [6] $(moles/mole)$	Final state mole ratio $\bar{C}_1^{(j)}$ [6] $(moles/mole)$	Molar mass $\mathbb{M}^{(j)}$ [6] $(g/mole)$	Equation of state
solid	$C_4H_8N_8O_8$	1	0	296.155	*
1	C	2	0.1899	12.0107	*
2	O	4.15	0.0322	15.9994	**
3	CO	1.65	1.1457	28.0101	*
4	CO_2	0.35	1.8779	44.0095	*
5	OH	1.35	0.1244	17.0073	**
6	H	6.35	0.5546	1.00794	**
7	H_2O	0.15	2.9419	18.0152	*
8	N	4.6	0.1059	14.0067	**
9	N_2	1.7	3.7709	28.0134	*
10	NH_3	0	0.3522	17.0305	**
11	C_2	0	0.3932	24.0214	**
12	H_2	0	0.1903	2.01588	*

Note: In the case of pure final product gases which admit an analytic equation of state, the simulation employs a Mie-Grüneisen form (*). Otherwise, the detonation gas product EOS (**) is assumed to apply.

Table 6.4: Equation of state parameters for the solid reactant in HMX [72].

Density ρ_o	1900 kg/m^3
Sound speed C_s	2650 m/s
Grüneisen γ	1.1
Specific Heat C_v	1000 J/KgK
Melting temperature θ_m	520 K
Young's Modulus E	20 GPa
Yield Stress Y	260 MPa

Table 6.5: Equation of state parameters for the HMX detonation gas products.

A	938.4941 GPa	[67]
B	21.9943 GPa	[67]
R_1	4.6	[67]
R_1	1.4	[67]
ω	0.35	[67]
q	11.97 GPa	[67]
C_v	1422 $J/kg \cdot K$	[84]
ρ_o	1900 kg/m^3	[67]

Table 6.6: Equation of state parameters for the final products in HMX and RDX.

Species	N_2	Ref.	H_2O	Ref.	CO_2	Ref.
Specific heat $C_v(J/kg \cdot K)$	743	[76]	1460	[76]	655	[76]
Specific heat $C_p(J/kg \cdot K)$	1040	[76]	1930	[76]	844	[76]
Sound speed $C_s(m/s)$	354.4	[78]	477.5	[78]	280	[78]
Density $\rho_o(kg/m^3)$	1.165	[75]	0.804	[75]	1.842	[75]
Grüneisen γ	0.4053	*	0.3964	*	0.3117	*
Species	CO	Ref.	C	Ref.	H_2	Ref.
Specific heat $C_v(J/kg \cdot K)$	720	[76]	710	[77]	10160	[76]
Specific heat $C_p(J/kg \cdot K)$	1020	[76]	710	[77]	14320	[76]
Sound speed $C_s(m/s)$	336	[78]	3900	[68]	1290	[78]
Density $\rho_o(kg/m^3)$	1.165	[75]	2200	[68]	0.0899	[75]
Grüneisen γ	0.3714	*	0.24	*	0.39	*

Note: $\theta_o = 298\ K$. * Grüneisen parameters are obtained from Eq.(4.19).

Table 6.7: Published experimental data for HMX.

Parameter	Value	Reference
CJ pressure (P_{CJ})	39.3 GPa	[45]
(avg. 40.2 GPa)	38.98 GPa	[80]
	43 GPa	[20]
	42 GPa	[13]
	38.7 GPa	[13]
	39 GPa	[32]
VN pressure (P_{VN})	60 GPa	[82]
(avg. 61.6 GPa)	63.9 GPa	[21]
	61 GPa	[20]
CJ velocity (v_{CJ})	2240 m/s	[82]
(avg. 2316.7 m/s)	2230 m/s	[43]
	2480 m/s	[21]
VN velocity (v_{VN})	3510 m/s	[20]
Detonation velocity (v_D)	9100 m/s	[13]

Chapter 7

Validation of the Integrated Models: RDX

In this chapter, validation simulations are presented for RDX, recognizing that initial validation work on a new method should consider at least two materials. The meso and macro scale simulations for RDX employ the formulations developed in Chapter 6.

7.1 Mesoscale Simulation

7.1.1 Chemical Kinetics Model

The chemical kinetics models described here were not developed in this dissertation, rather they are taken from separate research conducted concurrently [4–6].

The simplified 4-step short time (detonation) chemistry model for RDX is [6]:

$$
\begin{aligned}
C_3H_6N_6O_6 &\rightarrow 3NO_2 + 3CH_2 + 3N \qquad (7.1)\\
NO_2 + CH_2 &\rightarrow NOH + COH\\
3COH &\rightarrow 0.25CO_2 + 1.15CO + 3H + 1.35O + 1.6C\\
3NOH &\rightarrow 1.3N_2 + 0.4N + 0.1H_2O + 1.1OH + 1.8O + 1.7H
\end{aligned}
$$

Note that the final products of this chemistry model are intermediate states, and are distinct from the final products of the long time (recombination) chemistry model. In the detonation, the solid reactant is decomposed into 13 species of intermediate gas products. The short time chemistry model computes time dependent species concentrations, in the state space model for the system.

7.1.2 State Equations: Chemical Subsystem

The state equations for the species concentrations [6] are

$$\begin{aligned}
C_3H_6N_6O_6: &\quad \tfrac{dC_1}{dt} &&= -r_1 \\
NO_2: &\quad \tfrac{dC_2}{dt} &&= 3r_1 - r_2 \\
CH_2: &\quad \tfrac{dC_3}{dt} &&= 3r_1 - r_2 \\
N_2: &\quad \tfrac{dC_4}{dt} &&= 1.3r_4 \\
NOH: &\quad \tfrac{dC_5}{dt} &&= r_2 - 3r_4 \\
COH: &\quad \tfrac{dC_6}{dt} &&= r_2 - 3r_3 \\
CO_2: &\quad \tfrac{dC_7}{dt} &&= 0.25r_3 \\
CO: &\quad \tfrac{dC_8}{dt} &&= 1.15r_3 \\
C: &\quad \tfrac{dC_9}{dt} &&= 1.6r_3 \\
H: &\quad \tfrac{dC_{10}}{dt} &&= 3r_3 + 1.7r_4 \\
O: &\quad \tfrac{dC_{11}}{dt} &&= 1.35r_3 + 1.8r_4 \\
N: &\quad \tfrac{dC_{12}}{dt} &&= 3r_1 + 0.4r_4 \\
H_2O: &\quad \tfrac{dC_{13}}{dt} &&= 0.1r_4 \\
OH: &\quad \tfrac{dC_{14}}{dt} &&= 1.1r_4
\end{aligned} \tag{7.2}$$

where the C_i are species concentrations and the r_j are reaction rates.

7.1.3 Rate Laws

The reaction rates [6] are

$$\begin{aligned} r_1 &= k_1 C_1^{1.04} \left(\frac{\rho}{\rho_o}\right)^{1-m^{(j)}} u_s(\theta_{max}^{his} - \theta_{ign}) \\ r_2 &= k_2 C_2^{1.00} C_3^{1.00} \left(\frac{\rho}{\rho_o}\right)^{1-m^{(j)}} u_s(\theta_{max}^{his} - \theta_{ign}) \\ r_3 &= k_3 C_6^{1.40} \left(\frac{\rho}{\rho_o}\right)^{1-m^{(j)}} u_s(\theta_{max}^{his} - \theta_{ign}) \\ r_4 &= k_4 C_5^{1.00} \left(\frac{\rho}{\rho_o}\right)^{1-m^{(j)}} u_s(\theta_{max}^{his} - \theta_{ign}) \end{aligned} \tag{7.3}$$

where ρ and ρ_o are the particle density and the particle reference density, θ_{max}^{his} is the maximum historical temperature, θ_{ign} is the ignition temperature, and u_s denotes a unit step function. In the RDX validation example, $\theta_{ign} = 478.65$ K. The rate law constants k_j are shown in Table 7.1.

7.1.4 Equations of State

A reaction progress variable λ^{mes} is used to interpolate between the solid reactant pressure (P_{solid}) and the detonation gas products pressure P_{det}, so that the mesoscale particle pressure is

$$P_{meso} = (1 - \lambda^{mes})\, P_{solid} + \lambda^{mes}\, P_{det} \tag{7.4}$$

Similarly the mesoscale temperature is

$$\theta_{meso} = (1 - \lambda^{mes})\, \theta_{solid} + \lambda^{mes}\, \theta_{det} \tag{7.5}$$

The reaction progress variable is determined by the initial solid species concentration C^o_{solid} and the current solid species concentration C_{solid}

$$\lambda^{mes} = 1 - \frac{C_{solid}}{C^o_{solid}}, \qquad 0 \leq \lambda^{mes} \leq 1 \tag{7.6}$$

The solid equation of state takes a Mie-Grüneisen form

$$P_{solid} = C_s^2 (\rho - \rho_o) + \gamma \rho_o (e - e_o) \tag{7.7}$$

$$\theta_{solid} = \frac{1}{C_v} (e - e_o) \tag{7.8}$$

where θ denotes a temperature, C_s denotes a sound speed, ρ denotes a density, γ denotes a Grüneisen coefficient, and e denotes an internal energy per unit mass. Note that ρ_o and e_o are reference density and reference internal energy respectively. The model parameters are listed in Table 7.4.

The detonation products are modeled using a Jones-Wilkins-Lee (JWL) equation of state [27]

$$P_{det} = Ae^{-R_1\mu} + Be^{-R_2\mu} + C\mu^{(-1-\omega)} \tag{7.9}$$

$$\theta_{det} = \frac{1}{C_v} (e - e_o) \tag{7.10}$$

where

$$\mu = \frac{\rho_o}{\rho} \tag{7.11}$$

and the JWL coefficients A, B, C, R_1, R_2, and ω are shown in Table 7.5.

7.1.5 Simulation Results

The mesoscale validation simulation for RDX models a wall shock in a 2.5 μm long sample of RDX explosive, at an impact velocity of 500 m/s.

The voids are modeled explicitly, as shown in Figure 6.1. The simulation results are compared to published experimental data on the Chapman-Jouguet state and the detonation speed in RDX, which are listed in Table 7.6. The computation employs a Runge-Kutta second order method to integrate the ordinary differential equations.

Note that 50% void regions are placed in the explosive, as indicated in Figure 7.1. Figure 7.2 shows the initial velocity distribution, where the magenta colored lines denote the void region.

The shock fronts propagate from the wall outward, in both directions. Figure 7.3 shows that the detonation waves are generated in each void region, propagating in both directions. The waves which propagate toward the wall collide, producing high pressure and temperature spikes. The outgoing waves propagate with prominent pressure peaks (similar results are shown in reference [52]), including both primary and secondary shocks. The simulation results for particle velocity show good agreement with published experimental data. The dashed line denotes the steady state Chapman-Jouguet particle velocity (2085 m/s) listed in Table 7.6. Experimental averages are obtained from all the listed test data. The simulated shock pressures also show good agreement with published experimental data. Figure 7.4 shows pressure profiles at 0.35 ns. As in the case of the particle velocity plots, the dashed line denotes a Chapman-Jouguet state (34.28 GPa).

As expected for a wall shock, the reaction progress variable (λ) profile takes a step form, as shown in Figure 7.5. The species concentration for the

solid reactant $C_3H_6N_6O_6$ goes to zero as the explosive is fully reacted. Figures 7.6 and 7.7 show temperature and density profiles for the simulation.

Figure 7.15 shows convergence of the mesoscale simulation results, as a function of model resolution. The simulation results for the predicted detonation wave speed show both good convergence and good agreement with the corresponding experiment. The dashed red line denotes the published experimental result, provided in Table 7.6.

7.1.6 Ignition Process Model

The mesoscale simulation results suggest a simple ignition progress model, for use in the macroscale simulation. In the mesoscale simulation, pressure P and reaction progress λ are computed for each particle at every time step. The profiles of reaction progress variables for detonated particles are plotted in Figure 7.16. A linear fit for the ignition process parameter ζ is indicated in the figure and is used in the macroscale simulation.

$$\frac{df}{dP} = \zeta(P) \tag{7.12}$$

In Figure 7.16, the indicated slope ζ_o is

$$\zeta_o = \frac{1}{16} GPa^{-1} \tag{7.13}$$

Note that the mesoscale reaction progress variable plotted in Figure 7.16 is denoted as f in the macroscale simulation section which follows.

7.2 Macroscale Simulation

7.2.1 Chemical Kinetics Model

The 8-step long time chemistry model used to represent recombination in α-RDX is [6]:

$$\begin{aligned} C + O &\rightarrow CO \\ CO + O &\rightarrow CO_2 \\ OH + H &\rightarrow H_2O \\ N + N &\rightarrow N_2 \\ O + H &\rightarrow OH \\ C + C &\rightarrow C_2 \\ H + H &\rightarrow H_2 \\ H_2 + O &\rightarrow H_2O \end{aligned} \tag{7.14}$$

To address important time step issues, temperature is taken as the independent variable in modeling these recombination reactions, specifically the homologous temperature $\theta_H^{(i)}$ previously defined in Section 6.2.1.5. The macroscale RDX simulation employs $C_v = 1256\ J/kg \cdot K$ [1], and $\Delta E = 1452$ cal/J [55], $\theta_0 = 0\ K$ in Eq.(6.53), and $\theta_1 = 4836.9\ K$.

7.2.2 State Equations: Chemical Subsystem

In the macroscale model, the evolution equations for species j in element i are taken [6], for RDX, to be

$$\begin{aligned}
C: \quad & \frac{dC}{d\theta_H}^{(i,1)} &= & -R_1^{(i)} - 2R_6^{(i)} \\
O: \quad & \frac{dC}{d\theta_H}^{(i,2)} &= & -R_1^{(i)} - R_2^{(i)} - R_5^{(i)} - R_8^{(i)} \\
CO: \quad & \frac{dC}{d\theta_H}^{(i,3)} &= & R_1^{(i)} - R_2^{(i)} \\
CO_2: \quad & \frac{dC}{d\theta_H}^{(i,4)} &= & R_2^{(i)} \\
OH: \quad & \frac{dC}{d\theta_H}^{(i,5)} &= & -R_3^{(i)} + R_5^{(i)} \\
H: \quad & \frac{dC}{d\theta_H}^{(i,6)} &= & -R_3^{(i)} - R_5^{(i)} - 2R_7^{(i)} \\
H_2O: \quad & \frac{dC}{d\theta_H}^{(i,7)} &= & R_3^{(i)} + R_8^{(i)} \\
N: \quad & \frac{dC}{d\theta_H}^{(i,8)} &= & -2R_4^{(i)} \\
N_2: \quad & \frac{dC}{d\theta_H}^{(i,9)} &= & R_4^{(i)} \\
C_2: \quad & \frac{dC}{d\theta_H}^{(i,11)} &= & R_6^{(i)} \\
H_2: \quad & \frac{dC}{d\theta_H}^{(i,12)} &= & R_7^{(i)} - R_8^{(i)}
\end{aligned} \tag{7.15}$$

where $C^{(i,j)}$ denotes a spices concentration and $R_k^{(i)}$ denotes a reaction rate.

7.2.3 Rate Laws

The reaction rates [6] are

$$
\begin{aligned}
R_1^{(i)} &= k_1 \theta_H^{(i)\alpha_1} C^{(i,1)} C^{(i,2)} \left(\frac{\rho_o^{(i)}}{\rho^{(i)}} \right) u_s (P^{(i)} - P_{ign}) \\
R_2^{(i)} &= k_2 \theta_H^{(i)\alpha_2} C^{(i,2)} C^{(i,3)} \left(\frac{\rho_o^{(i)}}{\rho^{(i)}} \right) u_s (P^{(i)} - P_{ign}) \\
R_3^{(i)} &= k_3 \theta_H^{(i)\alpha_3} C^{(i,5)} C^{(i,6)} \left(\frac{\rho_o^{(i)}}{\rho^{(i)}} \right) u_s (P^{(i)} - P_{ign}) \\
R_4^{(i)} &= k_4 \theta_H^{(i)\alpha_4} C^{(i,8)} u_s (P^{(i)} - P_{ign}) \\
R_5^{(i)} &= k_5 \theta_H^{(i)\alpha_5} C^{(i,2)} C^{(i,6)} \left(\frac{\rho_o^{(i)}}{\rho^{(i)}} \right) u_s (P^{(i)} - P_{ign}) \\
R_6^{(i)} &= k_6 \theta_H^{(i)\alpha_6} C^{(i,1)} u_s (P^{(i)} - P_{ign}) \\
R_7^{(i)} &= k_7 \theta_H^{(i)\alpha_7} C^{(i,6)} u_s (P^{(i)} - P_{ign}) \\
R_8^{(i)} &= k_8 \theta_H^{(i)\alpha_8} C^{(i,2)} C^{(i,11)} \left(\frac{\rho_o^{(i)}}{\rho^{(i)}} \right) u_s (P^{(i)} - P_{ign})
\end{aligned}
\tag{7.16}
$$

where species concentrations $C^{(i,j)}$ and species masses are related by

$$
C^{(i,j)} = \frac{s^{(i,j)}}{\nu^{(i)} \mathbb{M}^{(j)}} \tag{7.17}
$$

In these expressions $\rho^{(i)}$ and $\rho_o^{(i)}$ are the element density and the element reference density. The rate law constants k_k and the exponents α_k are listed in Table 7.2. The parameter $\nu^{(i)}$ is an element volume, while $\mathbb{M}^{(j)}$ is the species molar mass listed in Table 7.3. Note that pressure based ignition criteria are used, with $P_{ign} = 2.84\ GPa$.

The state equations for the chemical subsystem determine the source terms in the reacted mass evolution equations as well as the reaction source

terms in the species mass evolution equations. The macroscale RDX simulation employs $\zeta_o = \frac{1}{16}\ GPa^{-1}$, obtained from the mesoscale simulation results. The parameters for the macroscale reaction source terms are listed in Tables 7.2 and 7.3.

7.2.4 Equations of State

In this section element superscripts are omitted, for clarity. The macroscale reaction progress variable λ^{mac} is defined by

$$\lambda^{mac} = \frac{\bar{C} - \bar{C}_0}{\bar{C}_1 - \bar{C}_0} \qquad 0 \leq \lambda^{mac} \leq 1 \tag{7.18}$$

and

$$\bar{C} = \frac{s^{(j)}}{m} \frac{\mathbb{M}^{solid}}{\mathbb{M}^{(j)}} \tag{7.19}$$

where $\bar{C}$ is a selected species concentration ratio (O_2 is chosen here), $\bar{C}_0$ is an initial species concentration ratio, and $\bar{C}_1$ is a final concentration ratio (the units of these concentration ratios are moles per unit mole of solid reactant), $\mathbb{M}^{solid}$ is the molar mass of the solid, and $\mathbb{M}^{(j)}$ is the molar mass of species j. The relevant parameters are listed in Table 7.3.

In the case of final product gases which admit an analytic equation of state, the simulation employs a Mie-Grüneisen form. Otherwise, an empirical detonation gas EOS is assumed to apply. The pressure of the gas mixture is then defined as a summation of partial pressures

$$P_{mix} = \sum {C_s}^2 \left(\rho_k - \rho_o\right) + \gamma \rho_o \left(e - e_o\right), \qquad k = 1, 3, 4, 7, 9, 11 \tag{7.20}$$

where the density of each species ρ_k is determined by the mixture density ρ and its mass fraction Y_k

$$\rho_k = Y_k \rho \tag{7.21}$$

and the coefficients are listed in Table 6.6.

The element pressure is finally defined by

$$P = (1-f)P_{solid} + f_{non}P_{det} + f_{ana}\left[(1-\lambda^{mac})P_{det} + \lambda^{mac}P_{gas}\right] \tag{7.22}$$

where f is the solid mass fraction. The mass fraction fraction f_{non} for the non-analytic species O, OH, H, N, C_2 is defined as

$$f_{non} = \sum Y_k, \qquad k = 2, 5, 6, 8, 10 \tag{7.23}$$

and the mass fraction f_{ana} for the analytic species C, CO, CO_2, H_2O, N_2, H_2 is defined as

$$f_{ana} = \sum Y_k, \qquad k = 1, 3, 4, 7, 9, 11 \tag{7.24}$$

The solid equation of state takes a Mie-Grüneisen form

$$P_{solid} = C_s^2\left(\rho - \rho_o\right) + \gamma\rho_o\left(e - e_o\right) \tag{7.25}$$

$$\theta_{solid} = \frac{1}{C_v}\left(e - e_o\right) \tag{7.26}$$

where θ denotes the temperature, C_s denotes the sound speed, ρ denotes the density, γ denotes the Grüneisen coefficient, and e denotes an internal energy per unit mass. Note that ρ_o and e_o are reference density and reference internal energy respectively. The EOS parameters are listed in Table 7.4.

The detonation products are modeled using a JWL equation of state [27]

$$P_{det} = Ae^{-R_1\mu} + Be^{-R_2\mu} + C\mu^{(-1-\omega)} \tag{7.27}$$

$$\theta_{det} = \frac{1}{C_v}(e - e_o) \tag{7.28}$$

where

$$\mu = \frac{\rho_o}{\rho} \tag{7.29}$$

and the JWL coefficients A, B, C, R_1, R_2, and ω are listed in Table 7.5.

The mixture temperature is defined as follows:

$$\theta = (1 - f)\theta_{solid} + \sum_{k=1}^{N_s} Y_k \theta_k \tag{7.30}$$

where the partial temperatures θ_k are

$$\begin{cases} \theta_k = \theta_{det}, & k = 2, 5, 6, 8, 10, \text{ for } O, OH, H, N, C_2 \\ \theta_k = \frac{1}{C_v}(e - e_o), & k = 1, 3, 4, 7, 9, 11, \text{ for } C, CO, CO_2, H_2O, N_2, H_2 \end{cases}$$

7.2.5 Simulation Results

The macrocale validation simulation for RDX models a flyer plate impact experiment for a 25 mm long RDX explosive sample. Figure 6.18 shows a schematic of simulation. The explosive samples are symmetrically positioned on both sides of a plane of symmetry; the elements near the plane of symmetry are assigned initial velocities of 2 km/s, as indicated in Figure 7.17. The detonation is initiated away from the wall, and propagates in both directions, resulting in a wave collision at the plane of symmetry. The outward moving

shock fronts propagate, generating a steady state detonation. The simulation results may be compared to published experimental data on the Chapman-Jouguet state, and the detonation wave speed, all of which are listed in Table 7.6. As in the mesoscale case, we compare to average experimental data. A fourth order Runge-Kutta method was employed to integrate the ODE model.

The simulation results are in good agreement with the experimental data for Chapman-Jouguet pressures (dashed lines), as shown in Figure 7.18. Figure 7.19 shows that the particle velocity profiles are also in good agreement with steady state CJ velocity (dashed lines) data. Figure 7.20 shows the computed temperatures. The species mass fraction distributions are plotted in Figures 7.21-7.26.

Figure 7.27 shows both: (1) converged results as model resolution is increased, and (2) good agreement with published experimental data for the detonation velocity in RDX (the red dashed line indicates the experimental results in Table 7.6).

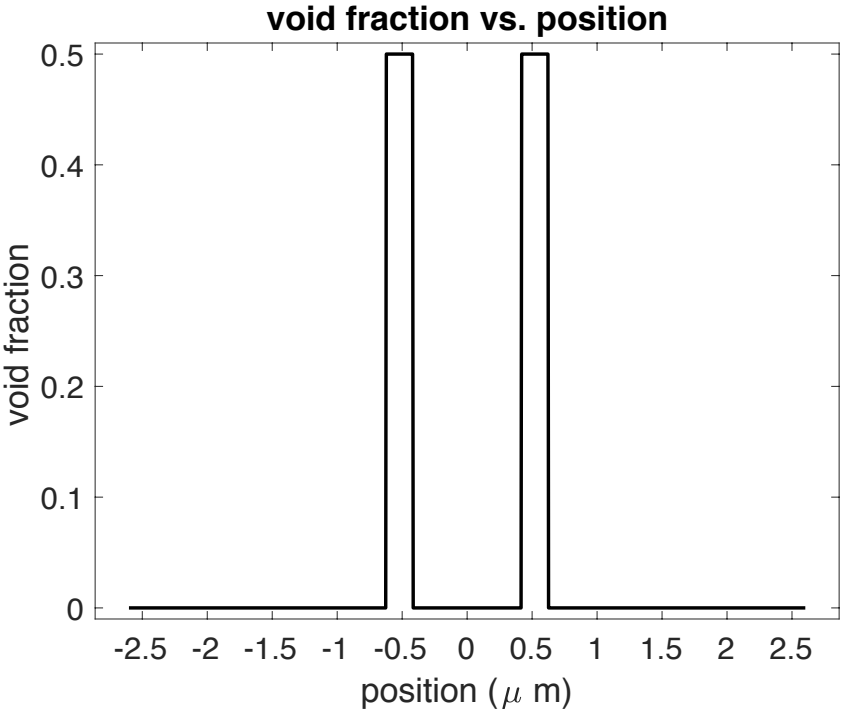

Figure 7.1: Void fraction distribution for the mesoscale simulation in RDX.

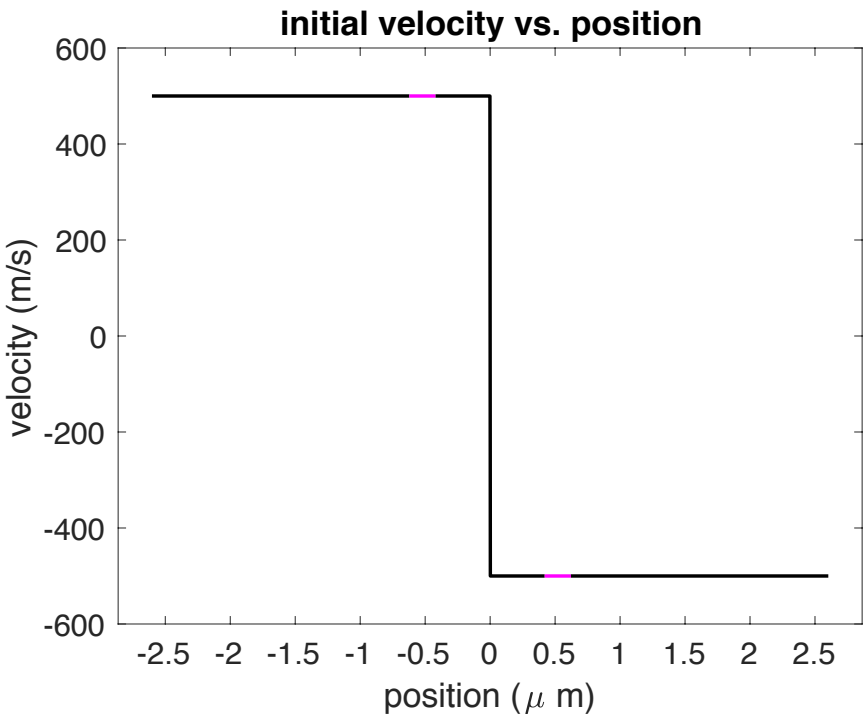

Figure 7.2: Initial velocities for mesoscale simulation in RDX. The magenta colored lines denote the void regions.

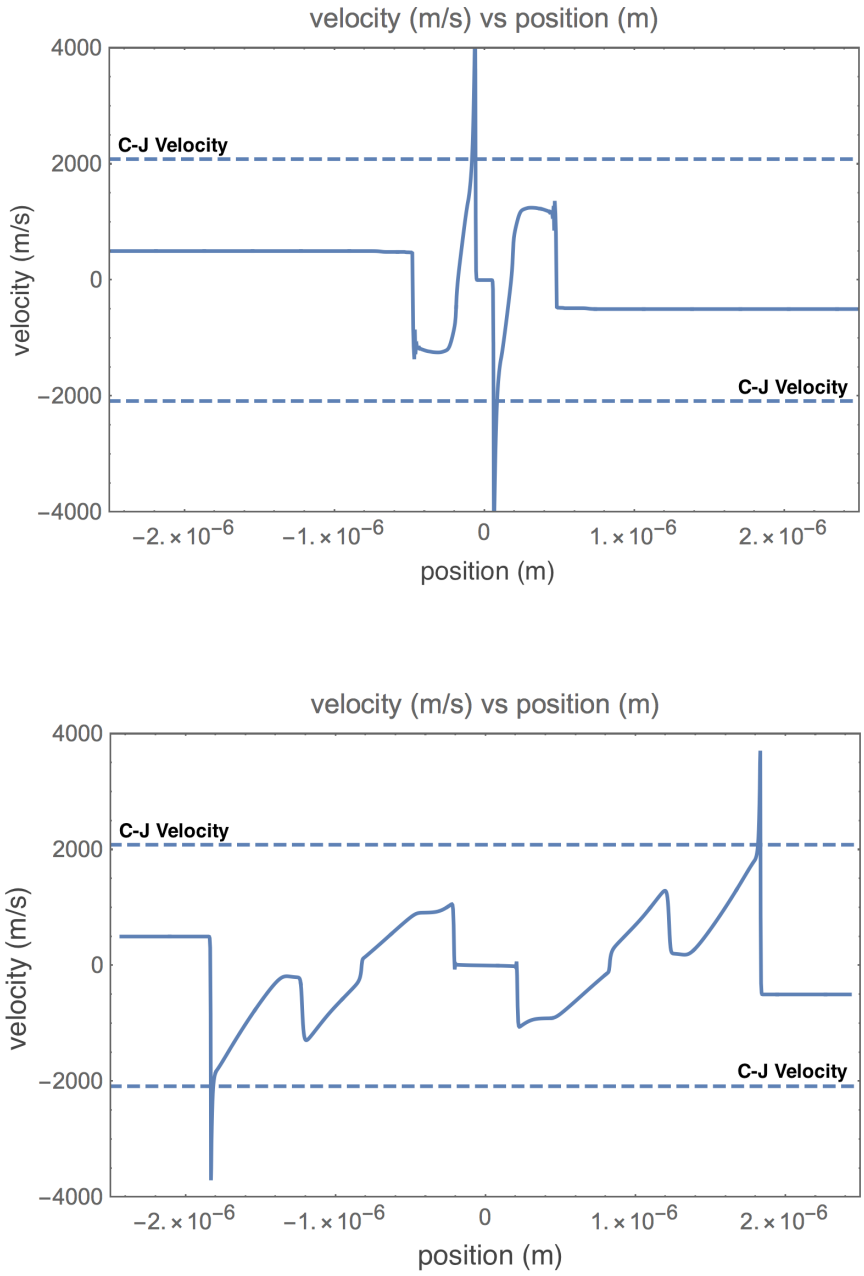

Figure 7.3: Mesoscale simulation of shock induced detonation in RDX: particle velocities at 0.182 ns (upper figure) and at 0.350 ns (lower figure). The dashed lines denote the Chapman-Jouguet (2085 m/s) velocity for the published experimental data listed in Table 7.6.

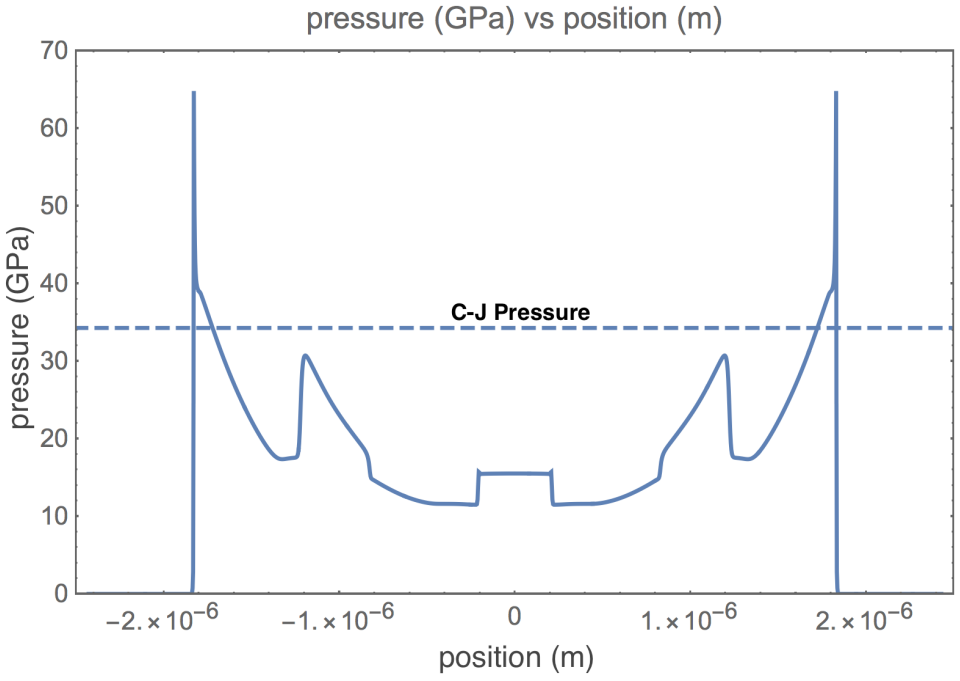

Figure 7.4: Mesoscale simulation of shock induced detonation in RDX: pressure. The dashed line denotes the Chapman-Jouguet (34.28 GPa) pressure from the published experimental data listed in Table 7.6.

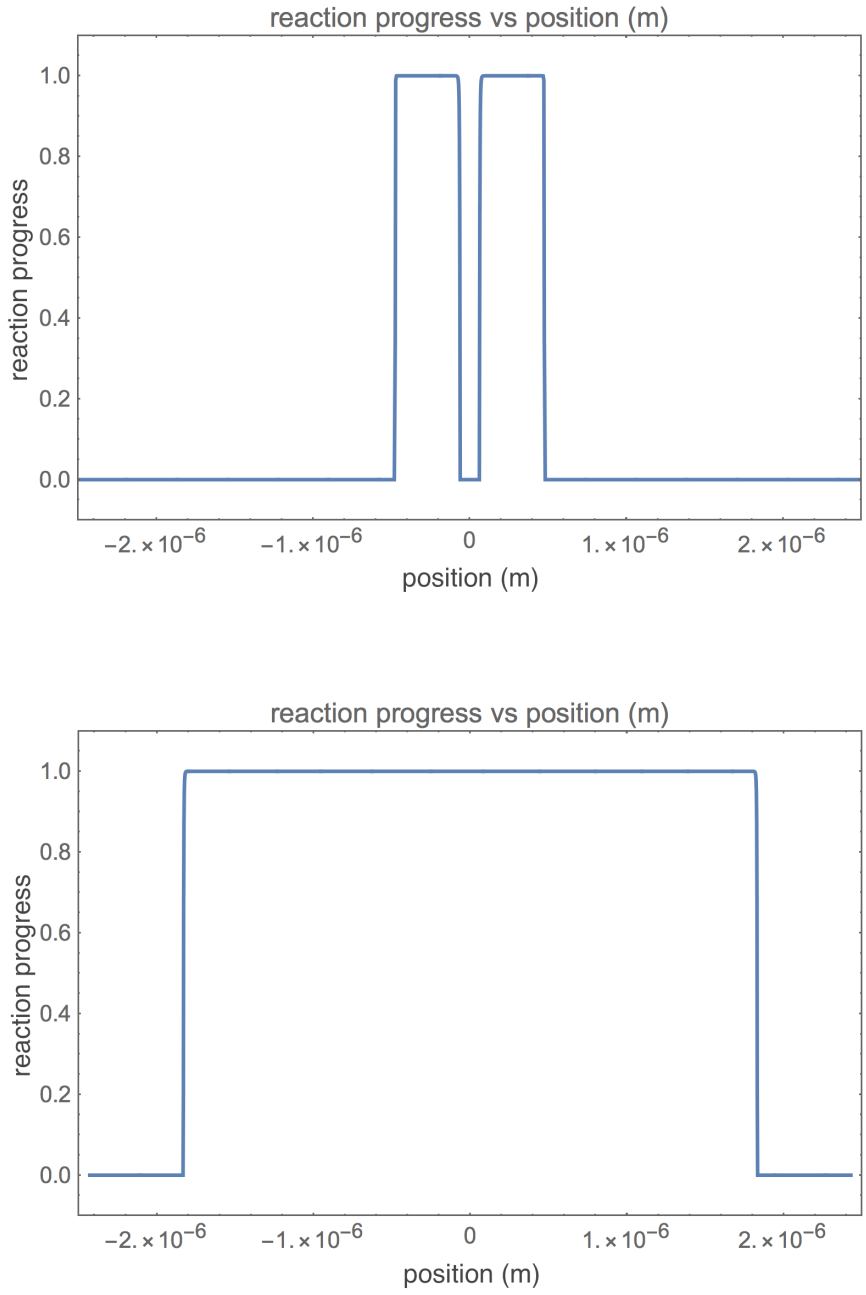

Figure 7.5: Mesoscale simulation of shock induced detonation in RDX: reaction progress variable at 0.182 ns (upper figure) and at 0.350 ns (lower figure).

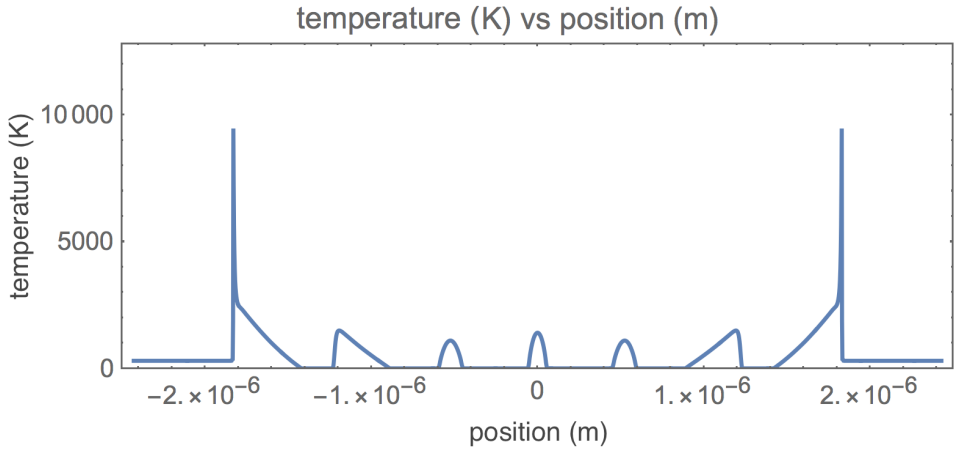

Figure 7.6: Mesoscale simulation of shock induced detonation in RDX: temperature.

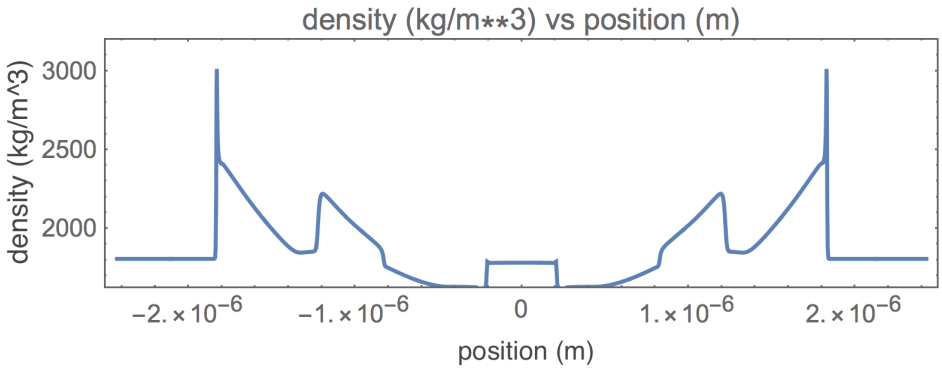

Figure 7.7: Mesoscale simulation of shock induced detonation in RDX: density.

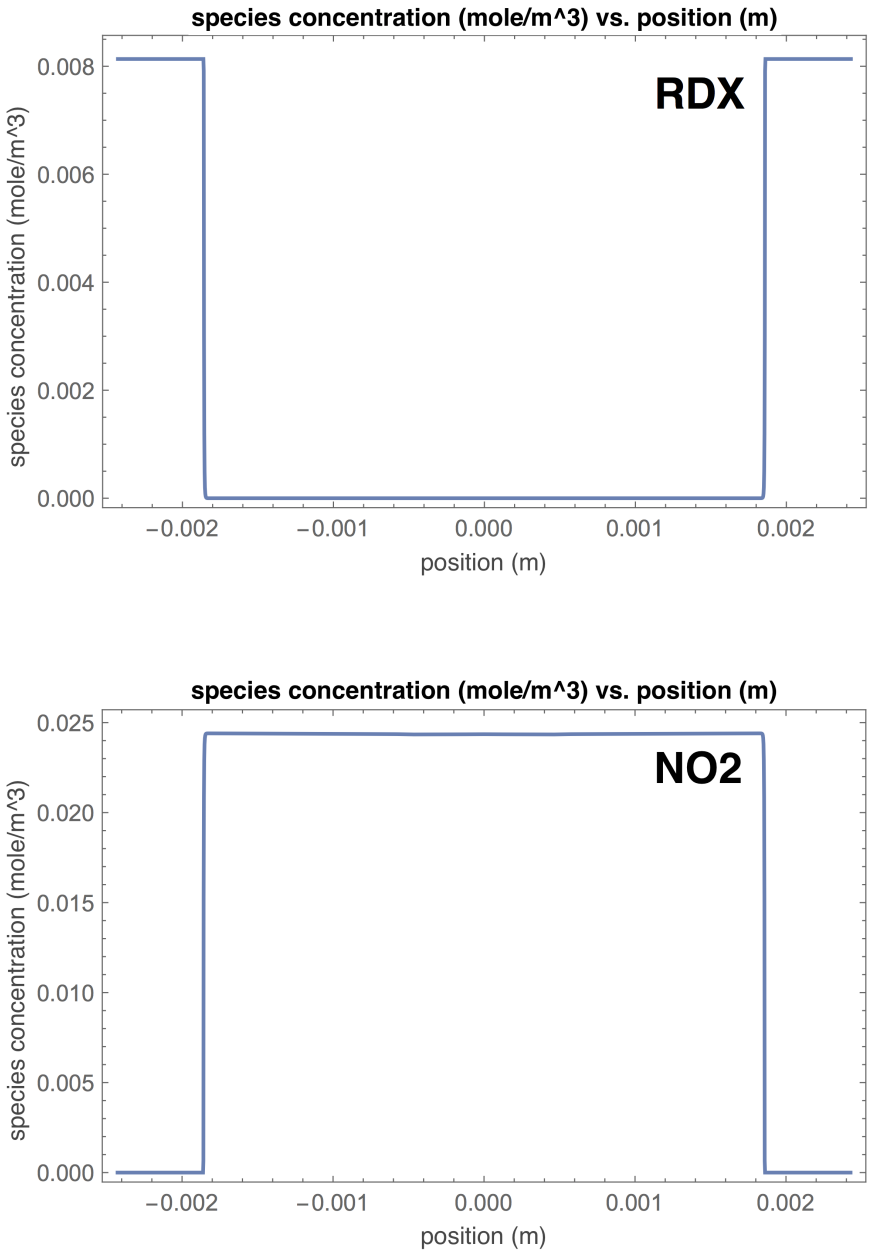

Figure 7.8: Mesoscale simulation of shock induced detonation in RDX: species concentrations for RDX and NO_2.

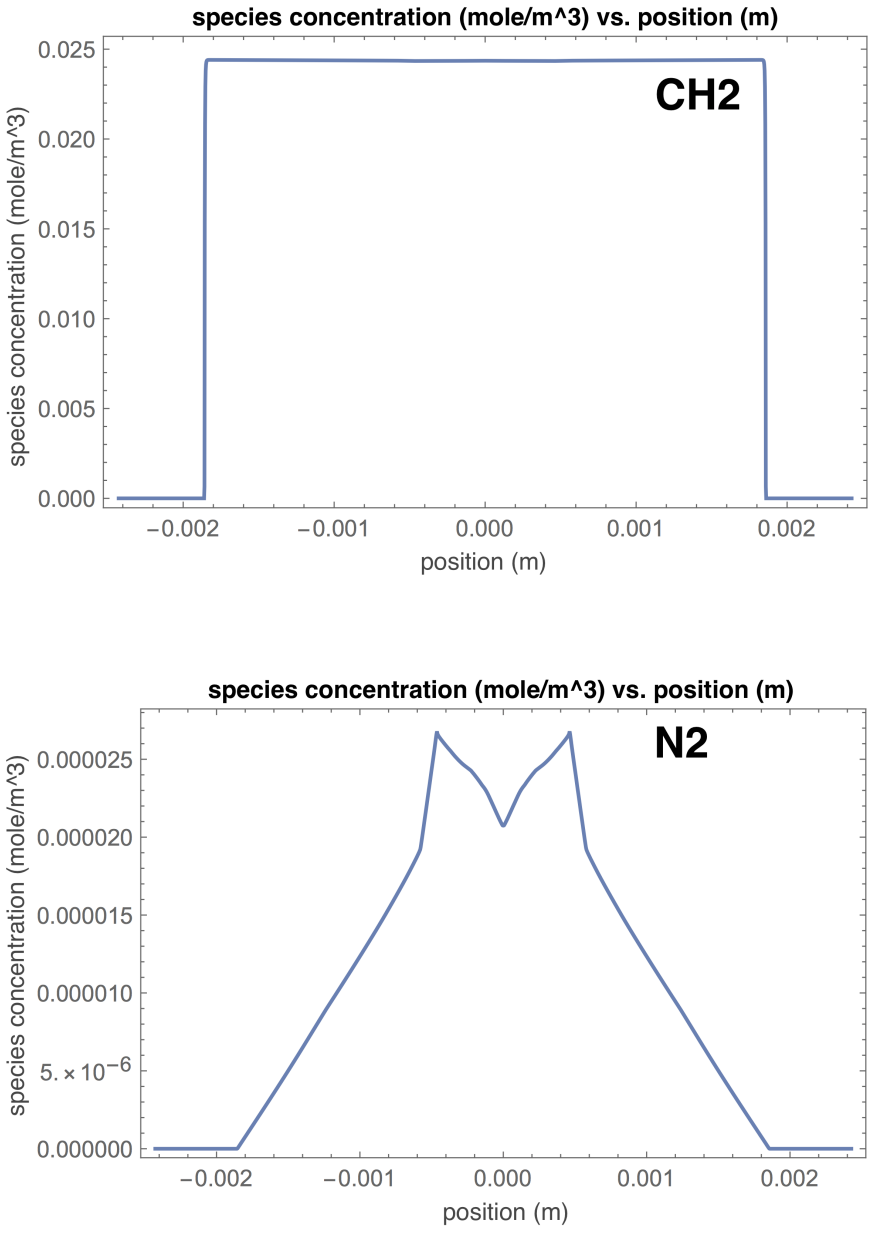

Figure 7.9: Mesoscale simulation of shock induced detonation in RDX: species concentrations for CH_2 and N_2.

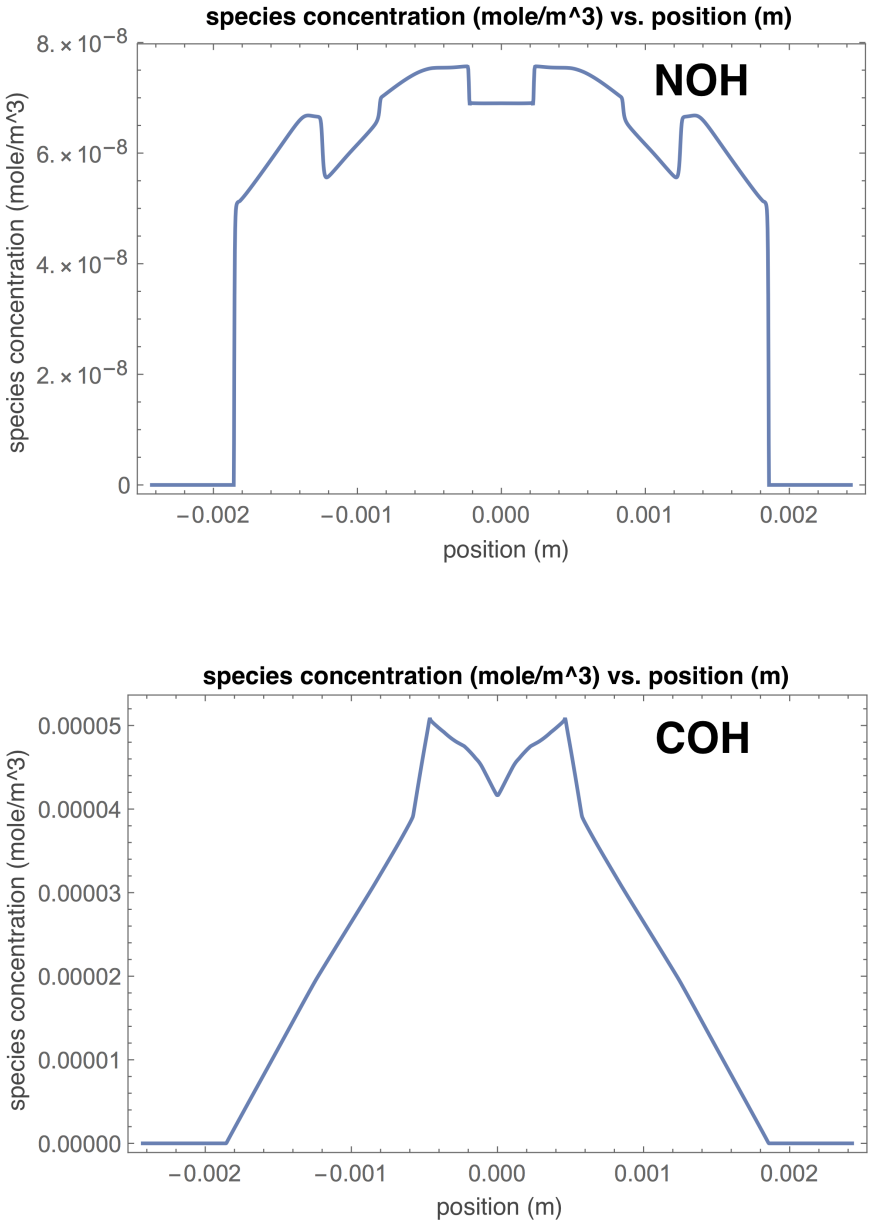

Figure 7.10: Mesoscale simulation of shock induced detonation in RDX: species concentrations for NOH and COH.

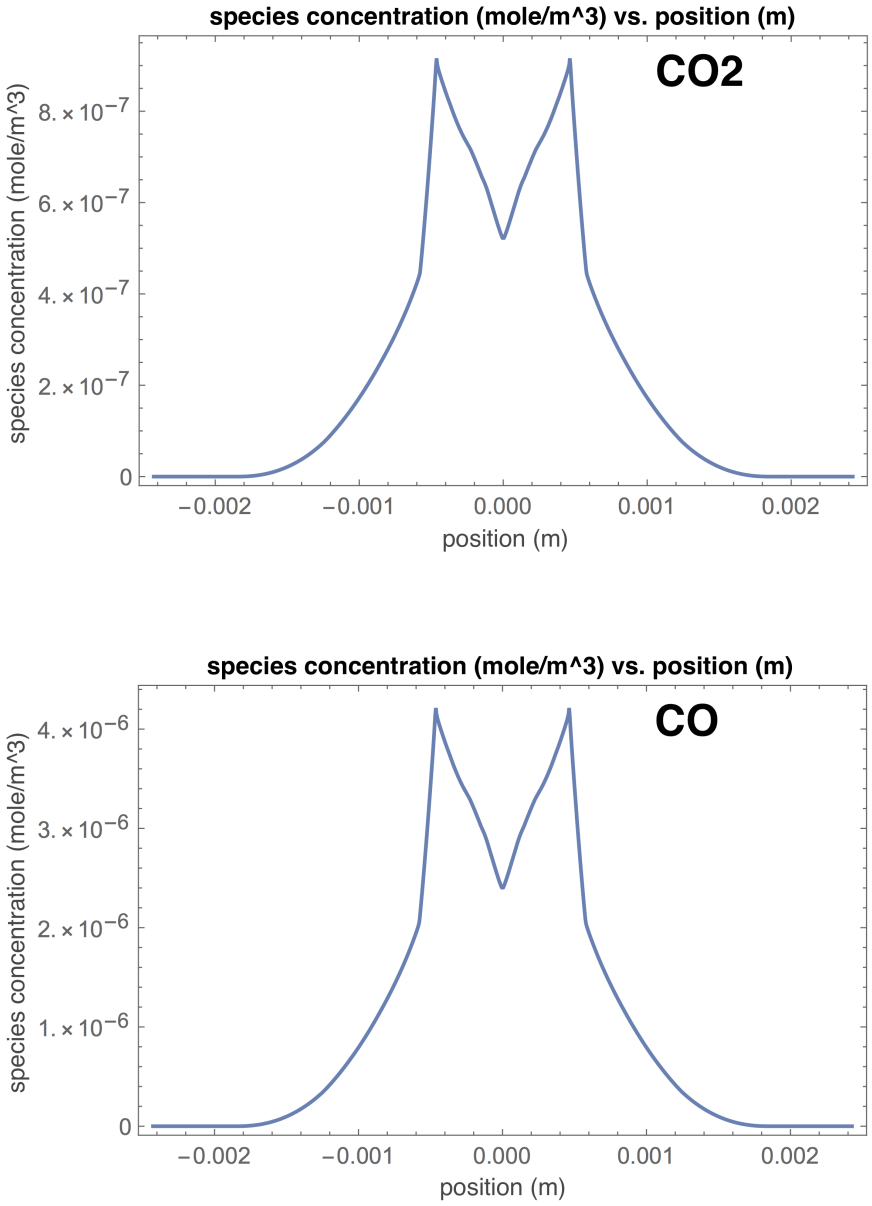

Figure 7.11: Mesoscale simulation of shock induced detonation in RDX: species concentrations for CO_2 and CO.

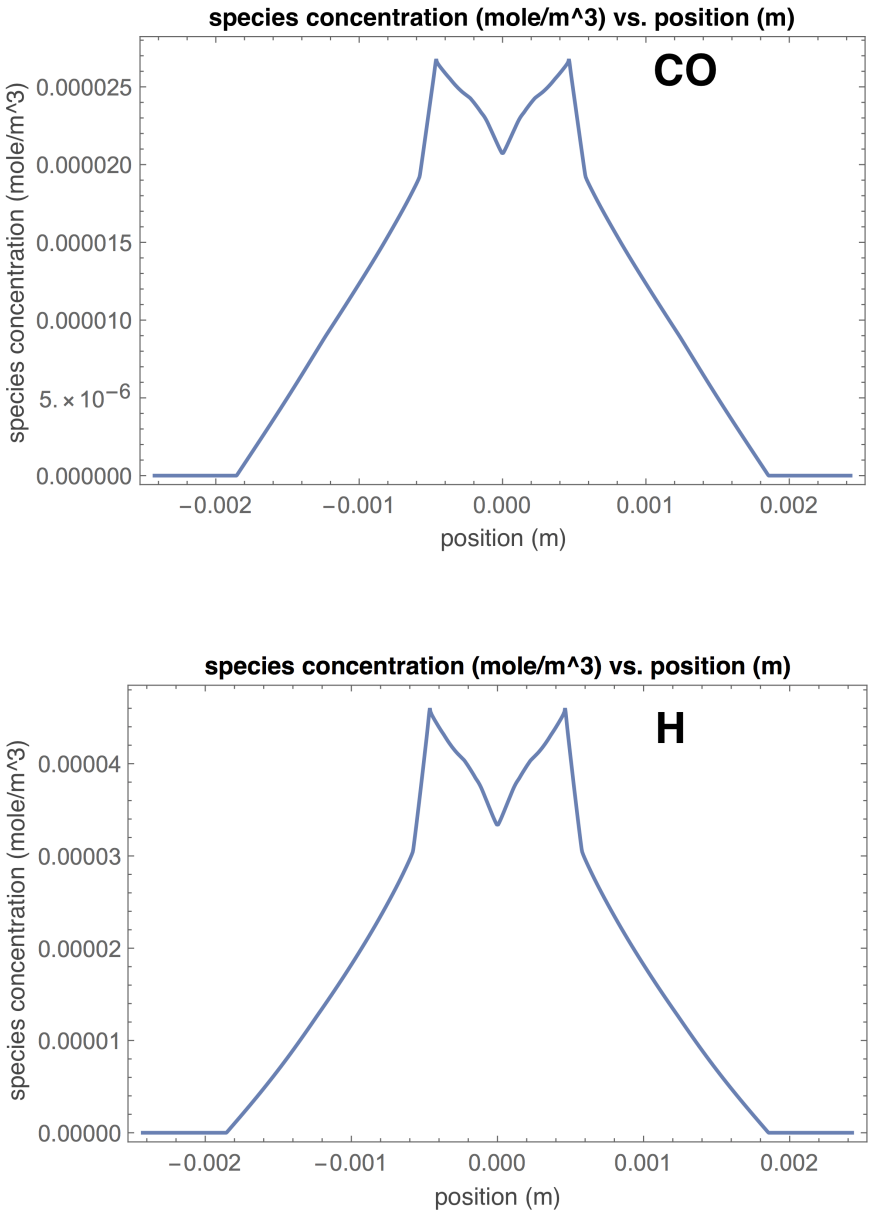

Figure 7.12: Mesoscale simulation of shock induced detonation in RDX: species concentrations for C and H.

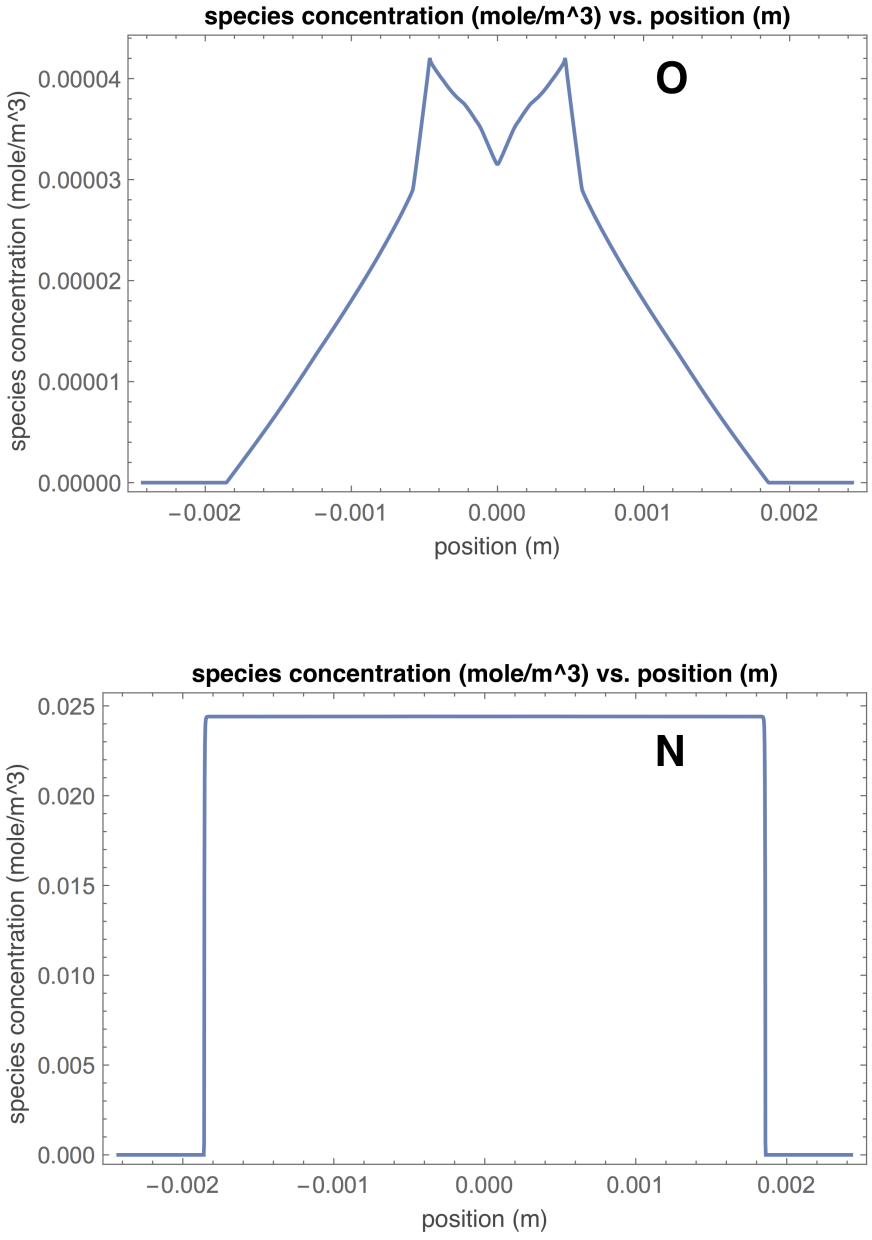

Figure 7.13: Mesoscale simulation of shock induced detonation in RDX: species concentrations for O and N.

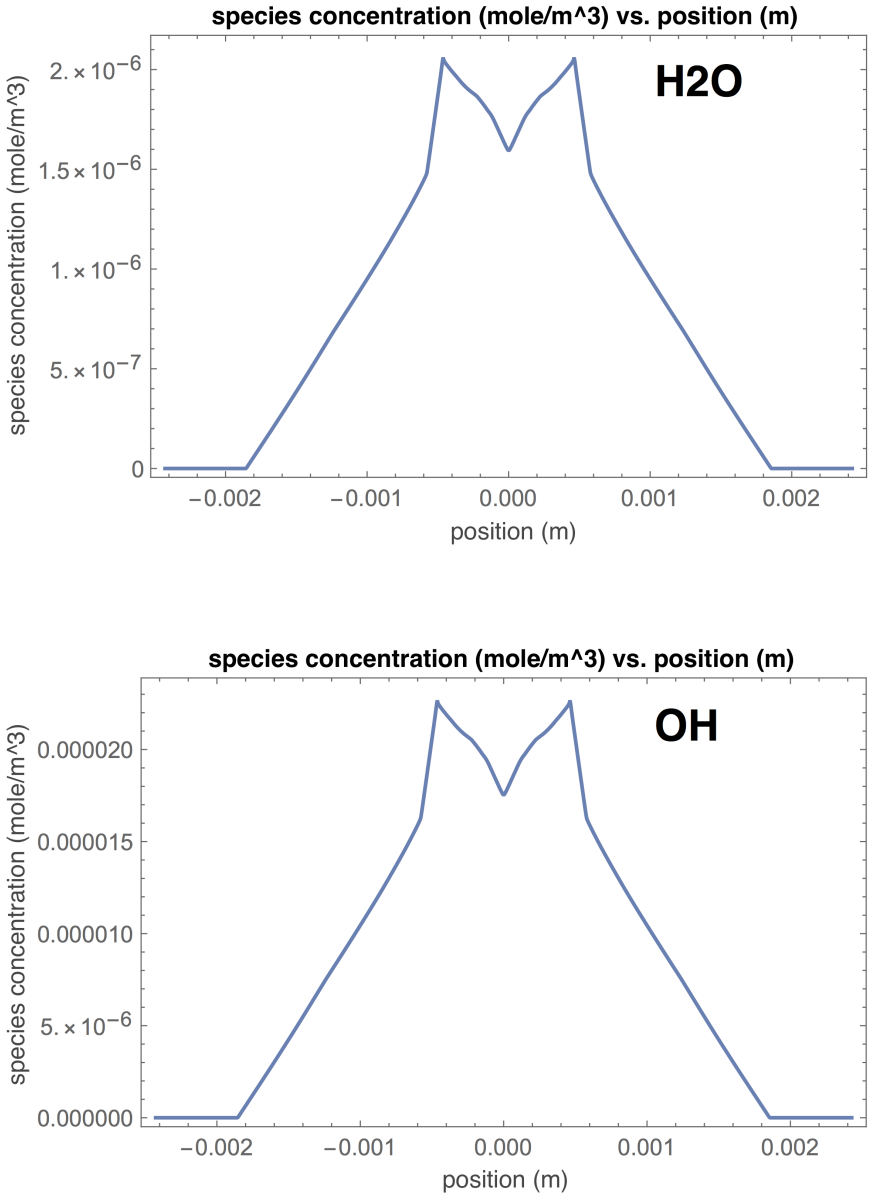

Figure 7.14: Mesoscale simulation of shock induced detonation in RDX: species concentrations for H_2O and OH.

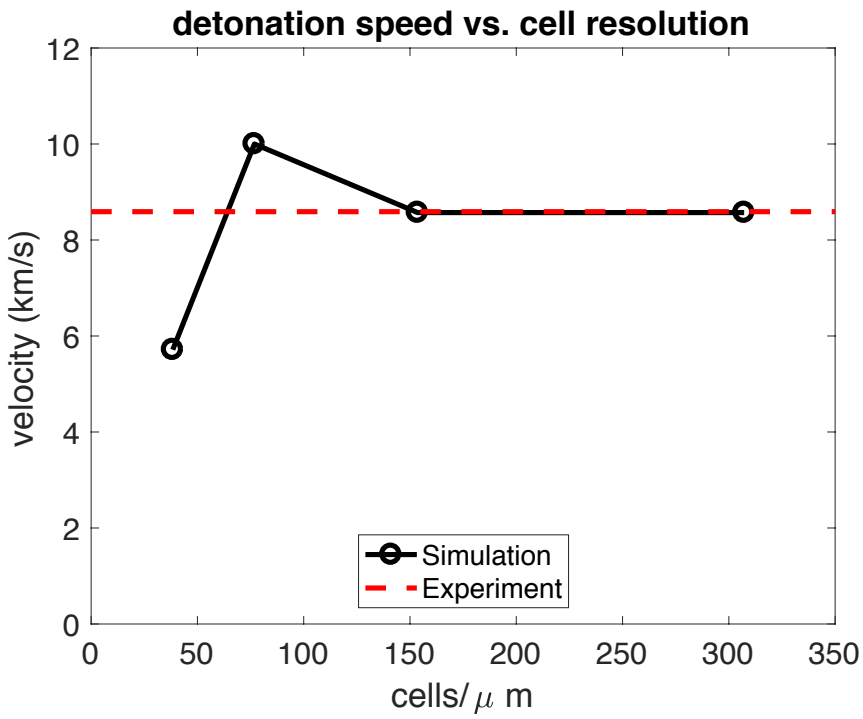

Figure 7.15: Convergence test: mesoscale simulation in RDX.

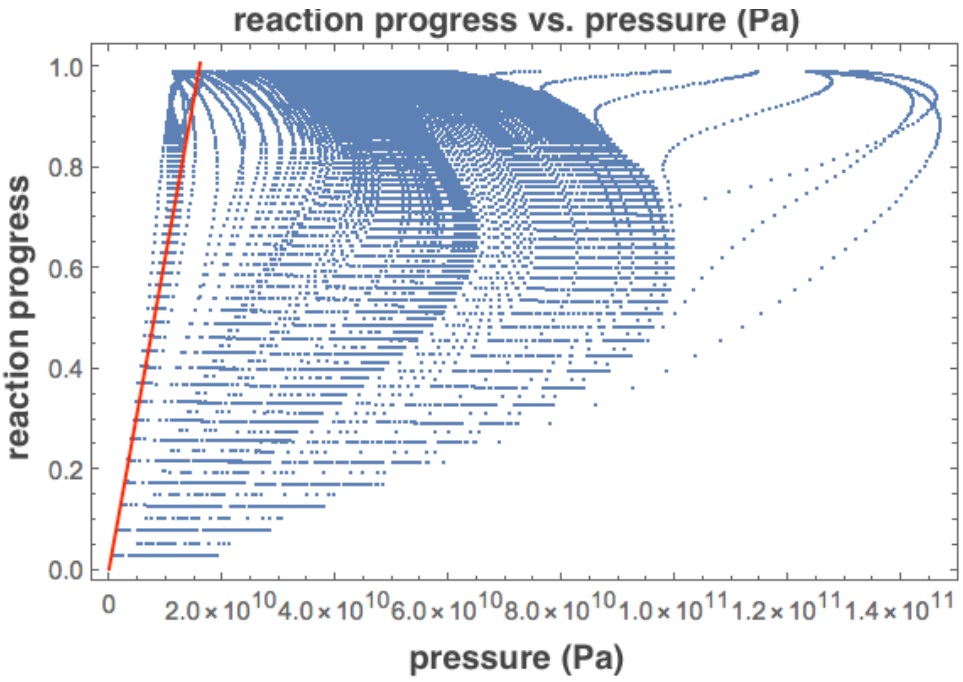

Figure 7.16: Reaction progress variable versus pressure (Pa) in RDX. The red line denotes the linear slope ($\zeta_o = \frac{1}{16}\ GPa^{-1}$).

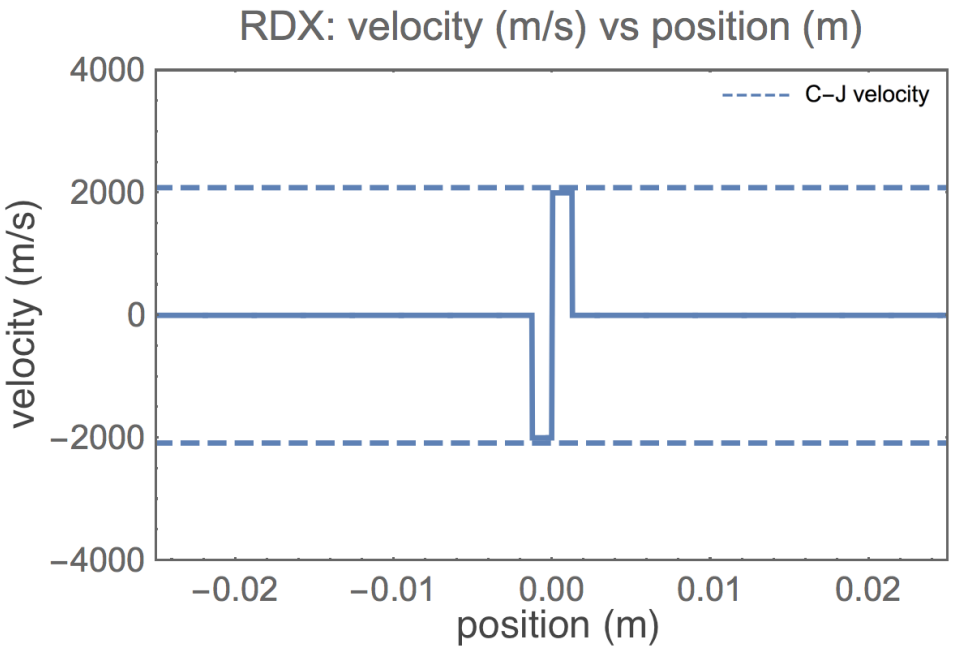

Figure 7.17: Initial velocity distribution: macroscale simulation in RDX.

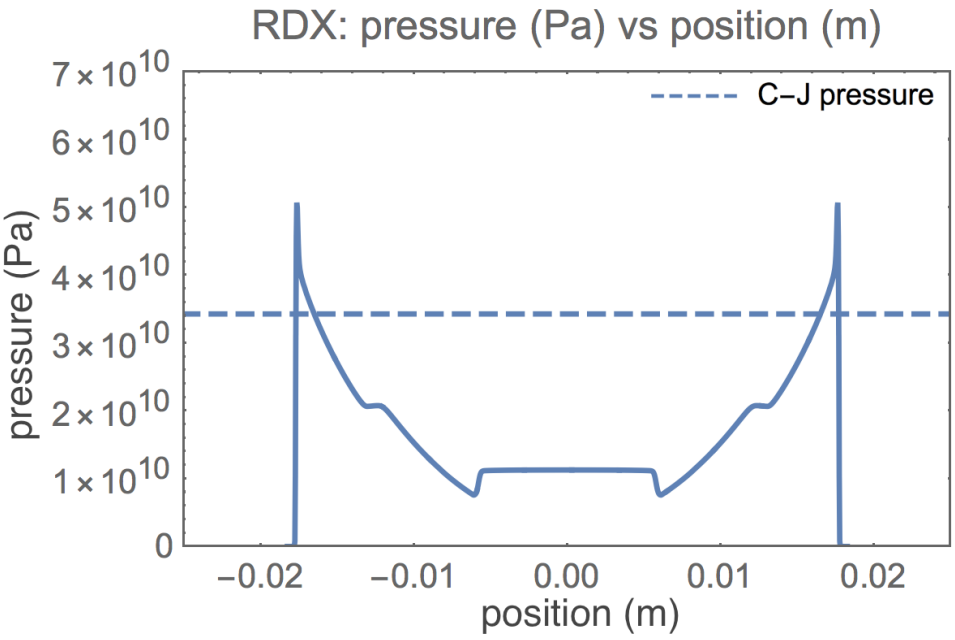

Figure 7.18: Macroscale simulation of shock induced detonation in RDX: pressure. The dashed line denotes the Chapman-Jouguet (34.28 GPa) pressure from the published experimental data listed in Table 7.6.

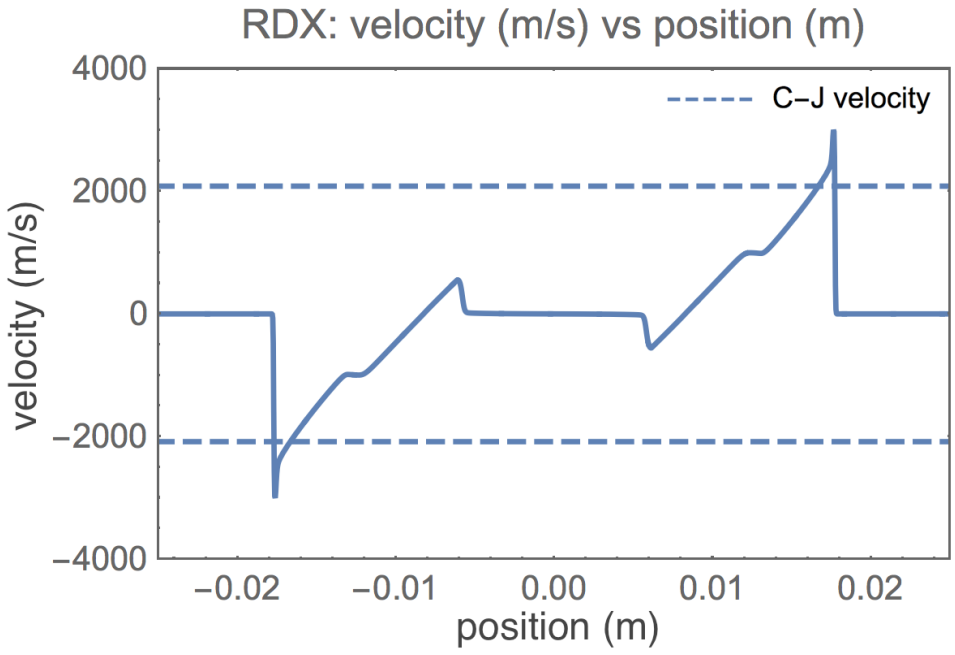

Figure 7.19: Macroscale simulation of shock induced detonation in RDX: velocity. The dashed lines denote the Chapman-Jouguet (2085 m/s) velocity from the published experimental data listed in Table 7.6.

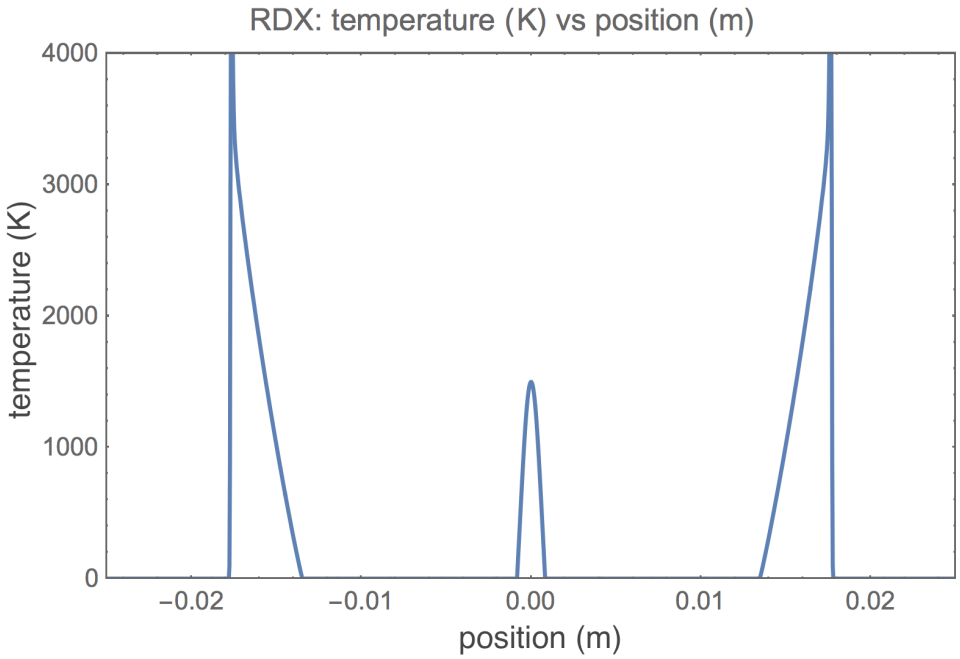

Figure 7.20: Macroscale simulation of shock induced detonation in RDX: temperature.

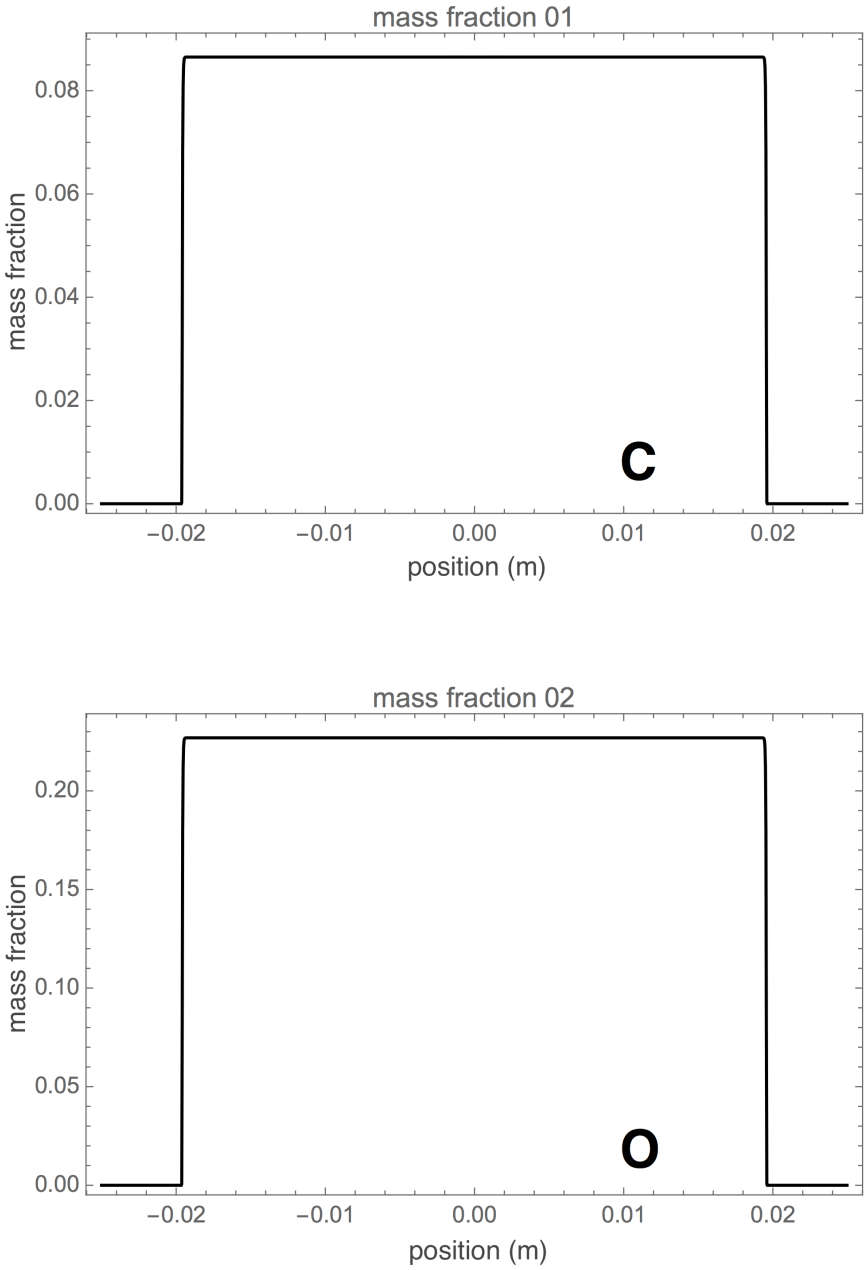

Figure 7.21: Macroscale simulation of shock induced detonation in RDX: species mass fractions for C and O.

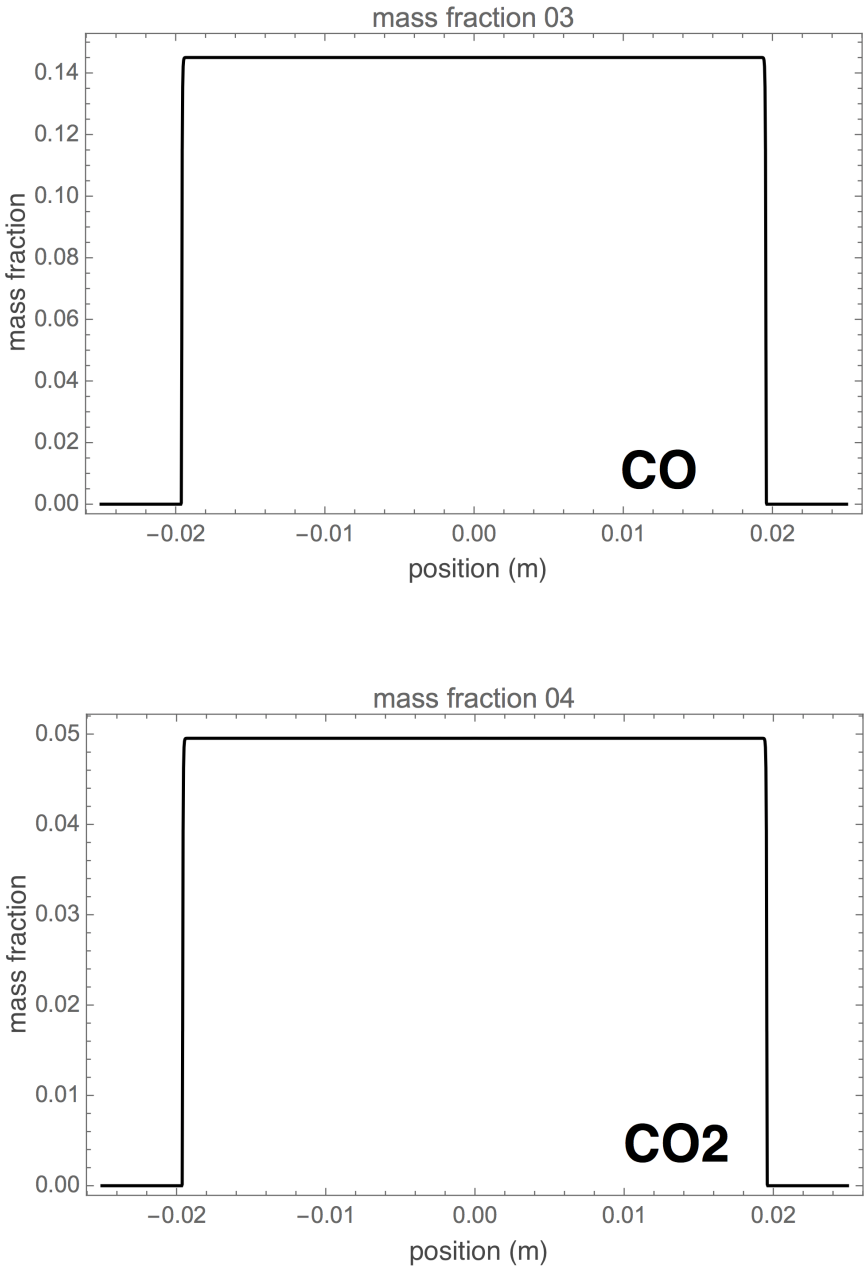

Figure 7.22: Macroscale simulation of shock induced detonation in RDX: species mass fractions for CO and CO_2.

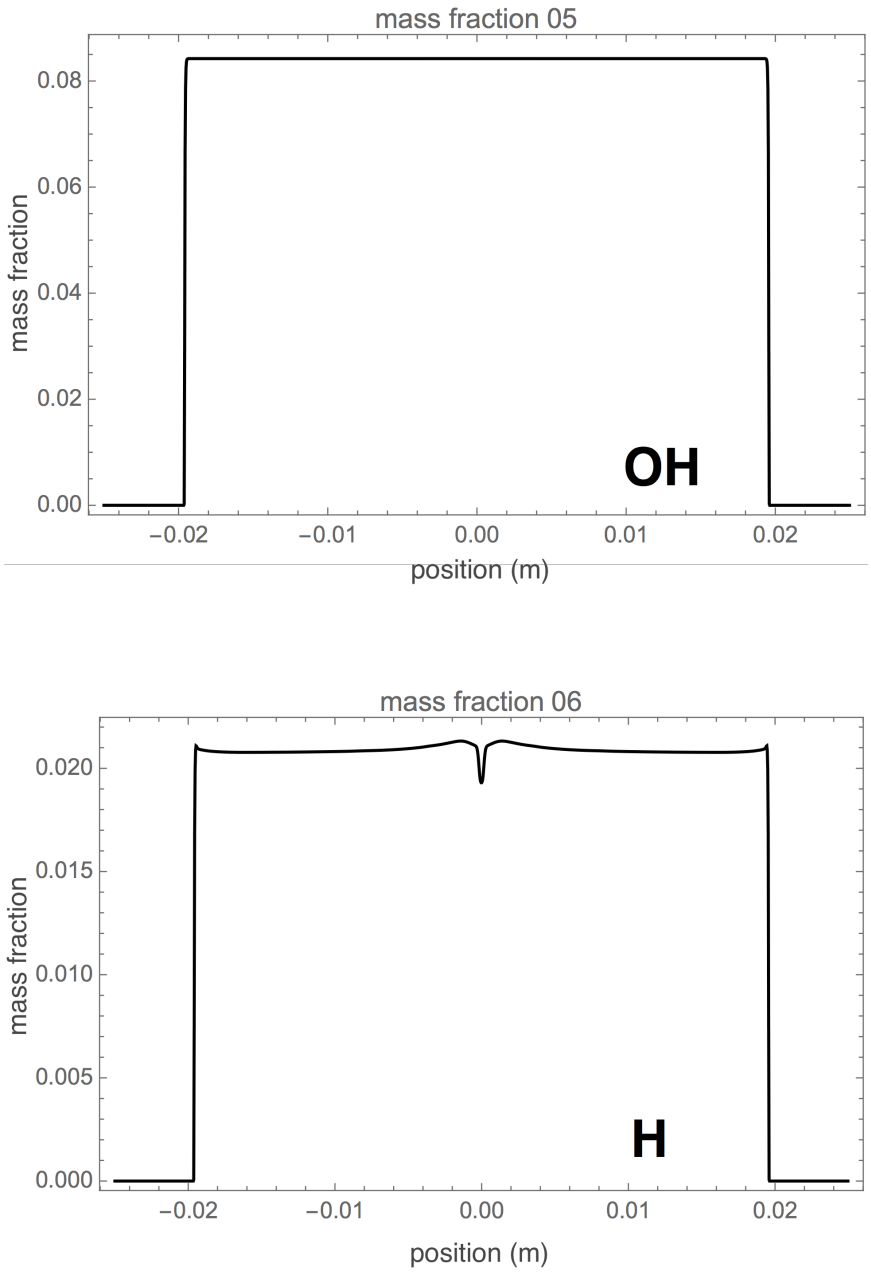

Figure 7.23: Macroscale simulation of shock induced detonation in RDX: species mass fractions for OH and H.

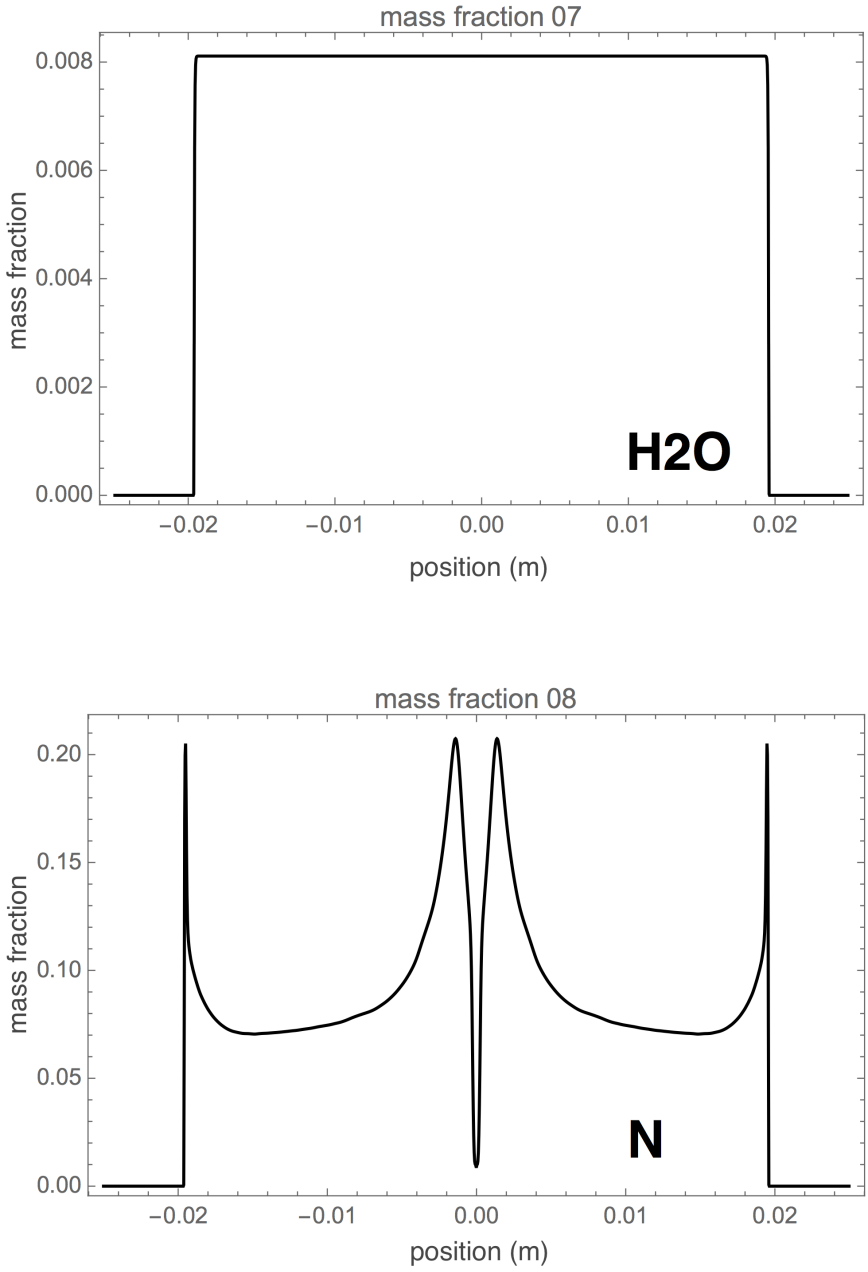

Figure 7.24: Macroscale simulation of shock induced detonation in RDX: species mass fractions for H_2O and N.

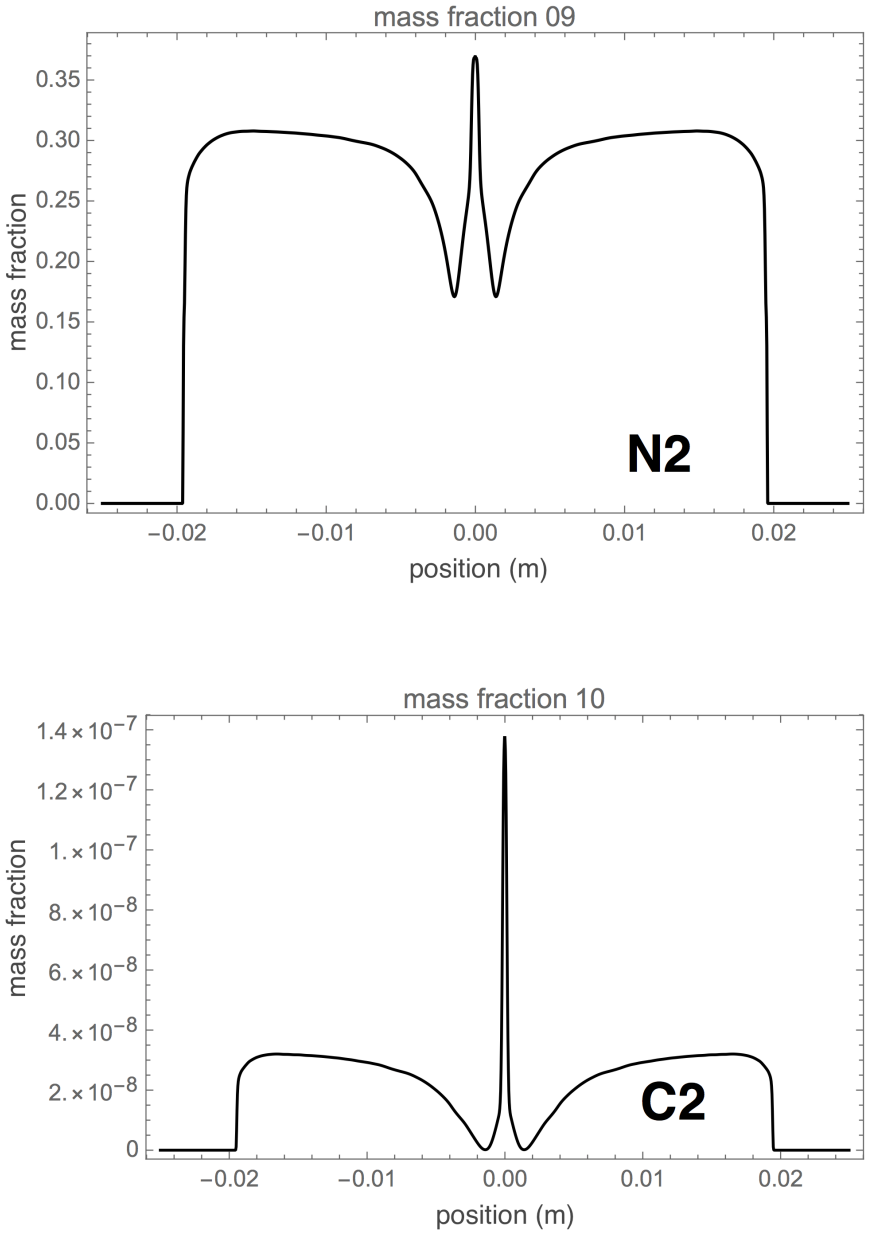

Figure 7.25: Macroscale simulation of shock induced detonation in RDX: species mass fractions for N_2 and C_2.

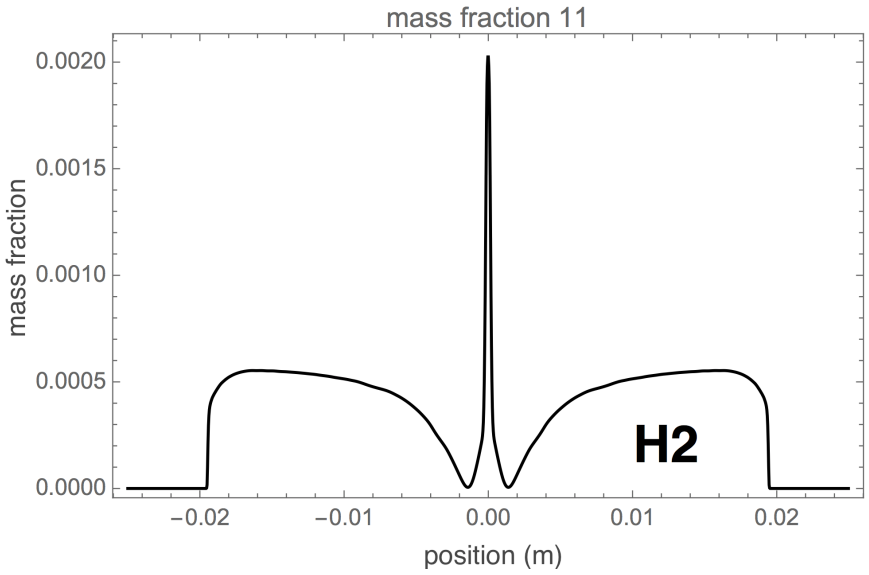

Figure 7.26: Macroscale simulation of shock induced detonation in RDX: species mass fraction for H_2.

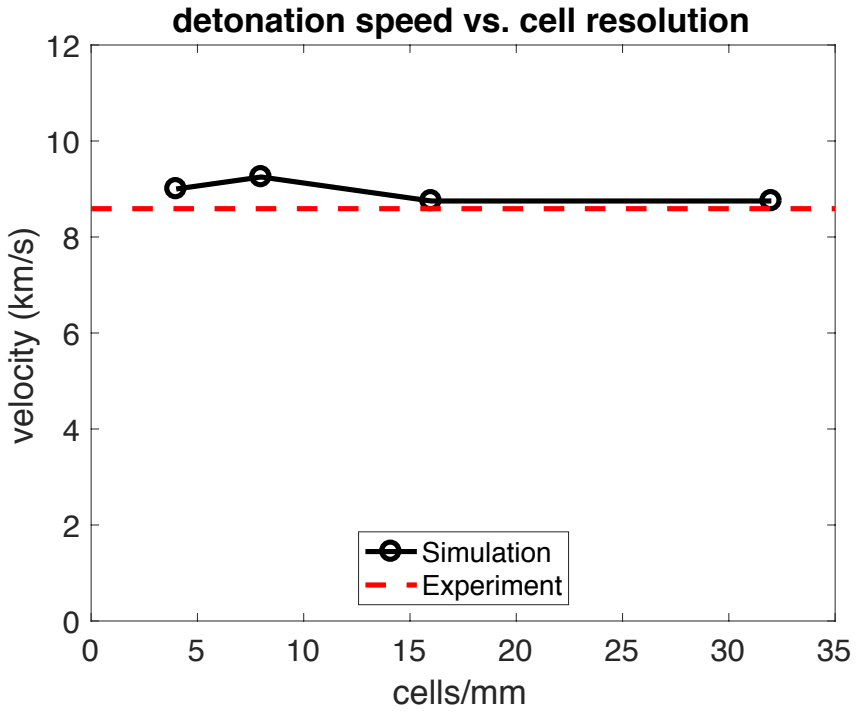

Figure 7.27: Convergence test: macroscale simulation in RDX.

Table 7.1: Rate law constants for the short time chemistry model in RDX [6].

j	k_j $(1/ps)(moles/cm^3)^{1-m^{(j)}}$	$m^{(j)}$
1	6.02	1.04
2	499.32	2.00
3	9.91	1.40
4	1.45	1.00

Table 7.2: Long time chemistry model for RDX [6].

i	Reaction			Rate constant (k_i) $(\frac{moles}{cm^3})^{1-m_i}$	Rate coefficient (α_i)	m_i
1	$C + O$	$\rightarrow$	CO	436.891	1.17437	2
2	$CO + O$	$\rightarrow$	CO_2	924.001	2.27523	2
3	$OH + H$	$\rightarrow$	H_2O	2184.88	2.79995	2
4	$N + N$	$\rightarrow$	N_2	4.29675	1.21881	1
5	$O + H$	$\rightarrow$	OH	64.0264	0.32714	2
6	$C + C$	$\rightarrow$	C_2	2.64239	2.56523	2
7	$H + H$	$\rightarrow$	H_2	1.91827	2.05726	1
8	$H_2 + O$	$\rightarrow$	H_2O	1043.46	2.79799	2

Table 7.3: Long time chemistry model parameters for RDX.

No. (j)	Species	Initial state mole ratio $\bar{C}_0^{(j)}$ [6] $(moles/mole)$	Final state mole ratio $\bar{C}_1^{(j)}$ [6] $(moles/mole)$	Molar mass $\mathbb{M}^{(j)}$ [6] $(g/mole)$	Equation of state
solid	$C_3H_6N_6O_6$	1	0	222.116	*
1	C	1.60	0.1523	12.0107	*
2	O	3.15	0.0261	15.9994	**
3	CO	1.15	1.0103	28.0101	*
4	CO_2	0.25	1.2197	44.0095	*
5	OH	1.10	0.0957	17.0073	**
6	H	4.70	0.2030	1.00794	**
7	H_2O	0.10	2.4287	18.0152	*
8	N	3.40	0.0707	14.0067	**
9	N_2	1.30	2.9646	28.0134	*
10	C_2	0.00	0.3089	24.0214	**
11	H_2	0.00	0.4220	2.01588	*

Note: In the case of pure final product gases which admit an analytic equation of state, the simulation employs a Mie-Grüneisen form (*). Otherwise, the detonation gas product EOS (**) is assumed to apply.

Table 7.4: Equation of state parameters for the solid reactant in RDX.

Density ρ_o	1806 kg/m^3	[80]
Sound speed C_s	2620 m/s	[35]
Grüneisen γ	2.2	[35]
Specific Heat C_v	1256 $J/kg \cdot K$	[1]
Melting temperature θ_m	478 K	[13]
Young's Modulus E	18.4 GPa	[9]
Yield Stress Y	300 MPa	[9]

Table 7.5: Equation of state parameters for the detonation gas products in RDX.

A	828.1 GPa	[27]
B	10.527 GPa	[27]
C	1.499 GPa	[27]
R_1	4.844	[27]
R_2	1.066	[27]
ω	0.395	[27]
C_v	1256 $J/kg \cdot K$	[1]
ρ_o	1630 kg/m^3	[27]

Table 7.6: Published experimental data for RDX.

Parameter	Value	Reference
CJ pressure (P_{CJ})	34.7 GPa	[45]
(avg. 34.28 GPa)	33.8 GPa (Exp.)	[13]
	34.8 GPa (Cal.)	[13]
	34 GPa	[32]
	34.1 GPa	[12]
CJ velocity (v_{CJ})	2085 m/s	[43]
Detonation velocity (v_D)	8754 m/s	[12, 45]
(avg. 8590 m/s)	8700 m/s	[13]
	8639 m/s	[80]

Chapter 8

Conclusion

The dissertation has developed and validated the first unified discrete nonholonomic Hamiltonian approach to multiscale simulation of reacting shock physics. The synchronous multiscale model has been formulated theoretically, while the asynchronous multiscale model has been formulated theoretically and validated in multiscale simulations of shock to detonation in HMX and RDX. The simulation results show good agreement with published experimental data.

The significant contributions of the research may be emphasized, as follows: (1) it presents the first unified multiscale formulation method, developed using a nonholonomic discrete Hamiltonian methodology at all scales, and (2) it presents a novel multiscale integration strategy; the great temporal and spacial disparities between scales are addressed by coupling the meso and macro scale thermomechanical models to distinct chemistry models, each of which incorporates time constants which match those of the corresponding thermomechanical subsystems.

The developed formulation includes new mesoscale models, employing either explicit or implicit representation of voids, allowing simple and expedient application to a grainscale hotspot generation simulation. The multiscale

integrating methodology replaces the heavy reliance on empirical detonation and growth models which now dominate the explosives modeling literature. Future work may extend the methods to additional scales (e.g. electronic structure), additional energy domains (e.g. magnetic fields), additional materials (e.g. materials for quantum computing), and additional reference frames (e.g. Arbitrary Lagrangian Eulerian). Future work should also consider the introduction of additional internal state variables, modeling for example material porosity or state of fragmentation. Fragmentation state modeling may assist in the interpretation of experimental measurements, since direct dynamic measurement of fragment distributions is difficult and a focus of current experimental research.

Bibliography

[1] N.K. Akhmadeev. Simulation of detonation-waves in solid explosives. *Combustion explosion and shock waves*, pages 87–93, 1981.

[2] R.A. Austin, N.R. Barton, J.E. Reaugh, and L.E. Fried. Direct numerical simulation of shear localization and decomposition reactions in shock-loaded HMX crystal. *Journal of Applied Physics*, 117:185902, 2015.

[3] A. Barua, S. Kim, Y. Horie, and M. Zhou. Ignition criterion for heterogeneous energetic materials based on hotspot size-temperature threshold. *Journal of Applied Physics*, 113:064906, 2013.

[4] J. Bass and E. Fahrenthold. A kinetic formulation of reacting shock physics. *presented at the 2016 ASME International Congress and Exposition, Pheonix, Arizona, November*, IMECE 2016-65451, 2016.

[5] J. Bass and E. Fahrenthold. Nonholonomic Hamiltonian method for molecular dynamics simulations of reacting shocks. *AIP Conference Proceedings*, 1793:070011–1–5, 2017.

[6] J.L. Bass. *Nonholonomic Hamiltonian Method for Reacting Molecular Dynamics*. PhD thesis, University of Texas at Austin, 2017.

[7] V.M. Boyle, R.L. Jameson, and F.E. Allison. Pressure measurements during shock initiation of composition B. *Tenth International Symposium on Combustion, The Combustion Institute*, pages 855–861, 1965.

[8] J.Q. Broughton, F.F. Abraham, N. Bernstein, and E. Kaxiras. Concurrent coupling of length scales: Methodology and application. *Physical Review B*, 60(4):2391, 1999.

[9] J.A. Brown and M.A. Zikry. Behaviour of crystallineamorphous interfaces in energetic aggregates subjected to coupled thermomechanical and laser loading. *Proceedings of Royal Society A*, 471(2148), 2015.

[10] H.B. Callen. *Thermodynamics*. John Wiley and Sons, Inc., 1960.

[11] J.K. Clutter and D. Belk. Simulation of detonation wave interaction using an ignition and growth model. *Shock Waves*, 12:251–263, 2002.

[12] N.L. Coleburn. Chapman-Jouguet pressures of several pure and mixed explosives. *United States Naval Ordnance Laboratory*, NOLTR 64-58, 1964.

[13] B.M. Dobratz. Properties of chemical explosives and explosive simulants. *Livermore: Lawrence Livermore Laboratory*, UCRL-51319, 1972.

[14] P. Harris et al. Some physics of the Grüneisen parameter. Technical Report AD-751130, NTIS, 1972.

[15] E.P. Fahrenthold. Computational design of orbital debris shielding. *AIAA 2014-4176, presented at the 2014 AIAA Space Conference, San Diego, CA, August*, 2014.

[16] E.P. Fahrenthold. Computational evaluation of metal foam orbital debris shielding. *IEEE 978-1-4799-5380-6/15, presented at the 2015 IEEE Space Conference, Big Sky, MT, March*, 2015.

[17] E.P. Fahrenthold and C.R. Hean. Discrete Lagrange equations for thermofluid systems. *Journal of Dynamic Systems, Measurement, and Control.*, 130:01009, 2008.

[18] E.P. Fahrenthold and J.C. Koo. Discrete Hamiltons equations for viscous compressible fluid dynamics. *Computer Methods in Applied Mechanics and Engineering*, 178:1–22, 1999.

[19] E.P. Fahrenthold, S. Lee, and J.L. Bass. Multiscale simulation of reacting shock physics. *AIAA 2016-1508, presented at the 2016 AIAA Scitech Conference, San Diego, CA, January*, 2016.

[20] A.V. Fedorov, A.L. Mikhailov, A.K. Antonyuk, D.V. Nazorov, and S.A. Finyushin. Determination of parameters of detonation waves in PETN and HMX single crystals. *Combustion Explosion and Shock Waves*, 47(5):601–605, 2011.

[21] A.V. Fedorov, A.L. Mikhailov, A.K. Antonyuk, D.V. Nazorov, and S.A. Finyushin. Determination of chemical reaction zone parameters, Neu-

mann peak parameters, and the state in the Chapman-Jouguet plane in homogeneous and heterogeneous high explosives. *Combustion Explosion and Shock Waves*, 48(3):302–308, 2012.

[22] J.E. Field, N.K. Bourne, S.J.P. Palmer, and S.M. Walley. Hot-spot ignition mechanisms for explosives and propellants. *Phil. Trans. R. Soc. Land. A*, 339:269–283, 1992.

[23] A.F. Fossum and R.M. Branno. THE SANDIA GEOMODEL: Theory and Users Guide. Technical Report SAND2004-3226, Sandia National Laboratories, Albuquerque, NM, August 2004.

[24] J.H. Ginsberg. *Advanced Engineering Dynamics*. Harper and Row Publishers, Inc., 1988.

[25] N. Goldman, E.J. Reed, I.-F.W. Kuo, L.E. Fried, C.J. Mundy, and A. Curioni. Ab initio simulation of the equation of state and kinetics of shocked water. *The Journal of Chemical Physics*, 130:124517, 2009.

[26] K.A. Gonthier and V. Jogi. Multisale shock heating analysis of a granular explosive. *J. Appl. Mech.*, 72(4):538–552, 2005.

[27] S. Grys and W.A. Trzcinski. Calculation of combustion, explosion and detonation characteristics of energetic materials. *Central European Journal of Energetic Materials*, 7(2):97–113, 2020.

[28] C.R. Hean. *Discrete Lagrange Equations for Reacting Thermofluid Systems*. PhD thesis, University of Texas at Austin, 2009.

[29] C.R. Hean and E.P. Fahrenthold. Discrete Lagrange equations for reacting thermofluid dynamics in arbitrary Lagrangian-Eulerian frames. *Compt. Mehods Appl. Mech. Engrg.*, 313:303–320, 2017.

[30] B.F. Henson, L.S. Smilowitz, J.J. Romero, and B.W. Asay. Modeling thermal ignition and the initial conditions for internal burning in PBX9501. *AIP Conference Proceedings*, 1195:257, 2009.

[31] R.J. Hernandez and E.P. Fahrentold. Hybrid particle-element method for an unstructured hexahedral mesh. *International Journal for Numerical Methods in Engineering*, 94:1191–1215, 2013.

[32] Y. Horie. *Shock wave science and technology reference library Vol.3*. Springer, 2009.

[33] S. Izvekov and G.A. Voth. A multiscale coarse-graining method for biomolecular systems. *Journal of physical chemistry letter B*, 109:2469–2473, 2005.

[34] S. Jiang, Z. Chen, T.D. Sewell, and Y. Gan. Multiscale simulation of the responses of discrete nanostructures to extreme loading conditions based on the material point method. *Comput. Methods Appl. Mech. Engrg.*, 297:219–238, 2015.

[35] G.I. Kanel, S.V. Razorenov, and V.E. Fortov. *Shock-wave phenomena and the properties of condensed matter*. Springer, 2014.

[36] J.W. Kury, R.D. Breithaupt, and C.M. Tarver. Detonation waves in trinitrotoluene. *Shock Waves*, 9:227–237, 1999.

[37] R. Kutteh and R.B. Jones. Rigid body molecular dynamics with nonholonomic constraints: Molecular thermostat algorithms. *Physical Review E*, 61(3):3186–3198, 2000.

[38] E.L. Lee and C.M. Tarver. Phenomenological model of shock initiation in heterogeneous explosives. *Physics of Fluids*, 23:2362–2372, 1980.

[39] S. Lee and E. Fahrenthold. Nonholonomic Hamiltonian method for meso-macroscale simulations of reacting shocks. *AIP Conference Proceedings*, 1793:080006–1–5, 2017.

[40] G. Levesque, P. Vitello, and W.M. Howard. Hot-spot contributions in shocked high explosives from mesoscale ignition models. *Journal of Applied Physics*, 113:233513, 2013.

[41] S. Li and N. Sheng. On multiscale non-equilibrium molecular dynamics simulations. *International Journal for Numerical Methods in Engineering*, 83:998–1038, 2010.

[42] E. Lidorikis, M.E. Bachlechner, R.K. Kalia, A. Nakano, P. Vashishta, and G.Z. Voyiadjis. Coupling length scales for multiscale atomistics-continuum simulations: Atomistically induced stress distributions in Si/Si_3N_4 nanopixels. *Physical Review Letter*, 87(8):086104, 2001.

[43] B.G. Loboiko and S.N. Lubyatkinsky. Reaction zones of detonating solid explosives. *Combustion Explosion and Shock Waves*, 36(6):716–733, 2000.

[44] Y. Long and J. Chen. Systematic study of the reaction kinetics for HMX. *J. Phys. Chem. A*, 119:4073–4082, 2015.

[45] C.L. Mader. *Numerical modeling of detonation*. UC Press., 1979.

[46] M.R. Manaa and L.E. Fried. The reactivity of energetic materials under high pressure and temperature. *Advances in Quantum Chemistry*, 69:221, 2014.

[47] J.M. McGlaun, S.L. Thompson, and M.G. Elrick. CTH: A three dimensional shock wave physics code. *International Journal of Impact Engineering*, 10:351–360, 1990.

[48] R.R. McGuire and C.M. Tarver. Chemical-decomposition models for the thermal explosion of confined HMX, TATB, RDX, and TNT explosives. Technical Report UCRL-84986, Lawrence Livermore National Lab., March 1981.

[49] R. Menikoff. Compaction wave profiles: Simulations of gas gun experiments. *Journal of Applied Physics*, 90:1754–1760, 2001.

[50] R. Menikoff and E. Kober. Equation of state and Hugoniot locus for porous materials: P-α model revisited. *Proceedings of Shock Compression of Condensed Matter*, pages 129–132, 1999.

[51] K.M. Mohamed and A.A. Mohamed. A review of the development of hybrid atomistic-continuum methods for dense fluids. *Microfluid Nanofluid*, 8:283–302, 2010.

[52] F.M. Najja, W.M. Howard, L.E. Fried, M.R. Manaa, S. Bastea, and A. Nichols III. Grain scale simulations of hot-spot initiation for shocked TATB. Technical Report LLNL-CONF-463873, Lawrence Livermore National Laboratory, December 2010.

[53] F.M. Najjar, W.M. Howard, L.E. Fried, M.R. Manaa, A. Nichols III, and G. Levesque. Computational study of 3-d hot-spot initiation in shocked insensitive high-explosive. *AIP Conference Proceedings*, 1426:255–258, 2012.

[54] J.P. O'Connell and J.M. Haile. *Thermodynamics*. Cambridge University Press, 2005.

[55] D.L. Ornellas. Calorimetric determinations of the heat and products of detonation for explosives : Otober 1981 to April 1982. Technical Report UCRL-52821, LLNL, 1982.

[56] J.M. Powers and S. Paolucci. Accurate spatial resolution estimates for reactive supersonic flow with detailed chemistry. *AIAA Journal*, 43(5):1088–1099, 2005.

[57] L. Qiao, X.F. Zhang, Y. He, X.N. Zhao, and Z.W. Guan. Multiscale modelling on the shock-induced chemical reactions of multifunctional en-

ergetic structural materials. *Journal of Applied Physics*, 113:173513, 2013.

[58] N.K. Rai and H.S. Udaykumar. Mesoscale simulation of reactive pressed energetic materials under shock loading. *Journal of Applied Physics*, 118:245905, 2015.

[59] D.J. Reding. Multiscale chemical reactions in reactive powder metal mixtures during shock compression. *Journal of Applied Physics*, 108:024905, 2010.

[60] E.J. Reed, L.E. Fried, and J.D. Joannopoulos. A method for tractable dynamical studies of single and double shock compression. *Physical Review Letters*, 90(23):235503, 2003.

[61] J.J. Rimoli, E. Gurses, and M. Ortiz. Shock-induced subgrain microstructures as possible homogeneous sources of hot spots and initiation sites in energetic polycrystrals. *Physical Review B*, 81:014112, 2010.

[62] N. Rom, B. Hirshberg, Y. Zeiri, D. Furman, S.V. Zybin, W.A. Goddard III, and R. Kosloff. First-principles-based reaction kinetics for decomposition of hot, dense liquid TNT from ReaxFF multiscale reactive dynamics simulations. *J. Phys. Chem. C*, 117:21043–21054, 2013.

[63] R.E. Rudd and J.Q. Broughton. Coarse-grained molecular dynamics and the atomic limit of finite elements. *Physical Review B*, 58(10):5893–5896, 1998.

[64] M.E. Shimek and E.P. Fahrenthold. Impact dynamics simulation for multilayer fabrics of various weaves. *AIAA Journal*, 53(7):1793–1811, 2015.

[65] K.J. Son and E.P. Fahrenthold. Simulation of orbital debris impact on porous ceramic tiles. *Journal of Spacecraft and Rockets*, 51(4):1349–1359, 2014.

[66] P.C. Souers and P. vitello. Initiation pressure thresholds from three sources. *Propellants, Explosives, Pyrotechnics*, 32:288, 2007.

[67] H.K. Springer, C.M. Tarver, J.E. Reaugh, and C.M. May. Investigating short-pulse shock initiation in HMX-based explosives with reactive meso-scale simulations. *Journal of Physics: Conference Series*, 500:052041, 2014.

[68] D.J. Steinberg. Equation of state and strength properties of selected materials. Technical Report UCRL-MA- 106439, Lawrence Livermore National Lab., 1996.

[69] V. Stepanov, T.M. Willey, J. Ilavsky, Gelb J, and H. Qiu. Structural characterization of RDX-based explosive nanocomposites. *Propellants Explos. Pyrotech.*, 38:386–393, 2013.

[70] D.S. Stewart, B.W. Asay, and K. Prasad. Simplified modeling of transition to detonation in porous energetic materials. *Phys. Fluids*, 6(7):2515–2534, 1994.

[71] D.E. Taylor and B.M. Rice. Quantum-informed multiscale M&S for energetic materials. *Advences in Quantum Chemistry*, 69:171–219, 2014.

[72] L. Tran and H.S. Udaykumar. Simulation of void collaps in an energetic material, part 1: Inert case. *Journal of Propulsion and Power*, 22(5):947, 2006.

[73] L. Tran and H.S. Udaykumar. Simulation of void collaps in an energetic material, part 2: Reactive case. *Journal of Propulsion and Power*, 22(5):959, 2006.

[74] Url. https://en.wikipedia.org/wiki/Grüneisen_parameter.

[75] Url. http://www.engineeringtoolbox.com/gas-density-d_158.html.

[76] Url. http://www.engineeringtoolbox.com/specific-heat-capacity-gases-d_159.html.

[77] Url. http://www.engineeringtoolbox.com/specific-heat-solids-d_154.html.

[78] Url. http://www.engineeringtoolbox.com/speed-sound-gases-d_1160.html.

[79] P.A. Urtiew, K.S.Vandersall, C.M. Tarver, F. Garcia, and J.W. Forbes. Shock initiation of Composition B and C-4 Explosives: experiments and modeling. *Russian Journal of Physical Chemistry B*, 2(2):162–171, 2008.

[80] R. Weinheimer. Properties of selected high explosives. *Grand Junction, Co., 27th International Pyrotechnics Seminar, July*, pages 16–21, 2000.

[81] L.-J. Wen, Z.-P. Duan, L.-S. Zhang, Z.-Y. Zhang, Z.-C. Ou, and F.-L. Huang. Effects of HMX particle size on the shock initiation of PBXC03 explosive. *Int. J. Nonlinear Sci. Numer. Simul.*, 13:189–194, 2012.

[82] B.W. White and C.M. Tarver. Ignition and growth modeling of detonation reaction zone experiments on single crystals of PETN and HMX. *AIP Conference Proceedings*, 1793:030001, 2017.

[83] M.A. Wood and A. Strachan. Nonequilibrium reaction kinetics in molecular solids. *Journal of Pys. Chem. C*, 120:542–552, 2016.

[84] J.J. Yoh, M.A. McClelland, J.L. Maienschein, and C.M. Tarver. Test-based thermal explosion model for HMX. *Proceedings of the combustion institute*, 31:2353–2359, 2007.

[85] J. Zhang, Z. Duan, and J. Ding. Simulating shock to detonation transition: Algorithm and results. *Journal of Computational Physics*, 150(1):128–142, 1999.

[86] L. Zhang, S.V. Zybin, A.C.T. van Dubin, S. Dasgupta, and W.A. Goddard III. Carbon cluster formation during thermal decomposition of octahydro-1,3,5,7-tetranitro-1,3,5,7-tetrazocine and 1,3,5-triamino-2,4,6-trinitrobenzene high explosives from ReaxFF reactive molecular dynamics simulations. *J. Phys. Chem. A*, 113:10619–10640, 2009.

[87] D. Zhao. Multiscale seismic tomography and mantle dynamics. *Gondwana Research*, 15:297–323, 2009.

[88] T. Zhou, H. Song, Y. Kiu, and F. Huang. Shock initiated thermal and chemical responses of HMX crystal from ReaxFF molecular dynamics simulation. *Phys. Chem.*, 16:13914–13931, 2014.

Vita

Sangyup Lee was born in Seoul, Korea. He received B.S. and M.S. degrees from Seoul National University in 2004 and 2006 respectively. He has worked in automotive industry for several years before he joined the University of Texas at Austin for his doctorate in 2013.

Email address: butterfox@utexas.edu

This dissertation was typeset with LaTeX[†] by the author.

[†]LaTeX is a document preparation system developed by Leslie Lamport as a special version of Donald Knuth's TeX Program.